Surface reflectance characteristics of Langjökull, Iceland

Ed Pope[1,2]

ATM, ETM+ and MODIS radiance data collected for the surface of Langjokull during August 2007. Radiance data from the three different instruments was then converted to surface broadband albedo using a number of different methods. The differences between the methods used to derive the surface albedo were then compared, followed by an analysis of the impact of spatial resolution and sample size on the differences between the derived surface albedo. Analysis of the different datasets combined with transect sample analyses of the derived surface albedos indicated that the most precise methods of deriving albedo from the ATM and ETM+ instruments was through the use of FLAASH for the ATM and dark pixel atmospheric correction or 6S atmospheric correction for the ETM+. These first analyses also indicated that the MODIS data was broadly in agreement with these two datasets. However, analysis of the differences between the different spatial resolution datasets across the three different spatial extents revealed a number of differences between the datasets. At the smallest scale the lower resolution datasets were shown to contain a bias towards representing certain areas in individual pixels. Consequently, the correlation between the datasets was reduced across greater sample sizes. Moreover, this bias was shown to prevent the ETM+ and MODIS imagery from averaging highly variable surfaces. The result of these measurement characteristics was for the low resolution instruments to overestimate the albedo value of snow in the accumulation area, greatly underestimate the albedo in the firn zone and struggle to capture the spatial variability in the ablation zone. The implications of these characteristics for lower resolution data have consequently been outlined, with the extent of the differences between both the low resolution datasets and the ATM dataset, indicating that where possible ETM+ imagery should be used to monitor surface albedo characteristics as it was the most closely correlated with the ATM data.

[1]Scott Polar Research Institute
University of Cambridge
Lensfield Road
Cambridge
CB2 1ER

Scott Polar Research Institute
University of Cambridge

[2]Jesus College
Jesus Lane
Cambridge
CB5 8BL

Acknowledgements

I would like to thank my supervisor, Ian Willis, for his guidance and helpful comments about this project. I would also like to thank Allan Pope for a number of useful discussions we had about the project some of the possible methods which could be used.

In addition I would like to thank the staff and students at the Scott Polar Research Institute for an enjoyable and enriching year.

Declaration

This dissertation is the result of my own work and does not exceed 20,000 words excluding dissertation declaration, acknowledgements, abbreviations and acronyms, variables list, table of contents, list of figures, list of tables, abstract, figure and table and their associated captions, references and appendices.

Contents

List of Figures

List of tables

Acronyms and Abbreviations

ARSF – Airborne Research and Survey Facility

ASL – Above sea level

ASTER – Advanced Spaceborne Thermal Emission and Reflection Radiometer

ATM – Airborne Thematic Mapper

BHR – Bihemispherical reflectance

BRDF – Bidirectional Reflectance Distribution Function

CPF – Calibration Parameter File

DN – Digital Number

DEM – Digital Elevation MODEL

ETM+ – Enhanced Thematic Mapper Plus

FLAASH – Fast-line-of-sight Atmospheric Analysis of Spectral Hypercubes

FSF – Field Spectroscopy Facility

FWHM – Full-Width Half-Maximum

GDEM – Global Digital Elevation Model

GIC – Glaciers and Ice Caps

GISP – Greenland Ice Sheet Project

GMT – Greenwich Meridian Time

HDF – Hierarchical Data Format

HDR – Hemispherical directional reflectances

IFOV – Instantaneous field of view

MODIS – MODerate resolution Imaging Spectroradiometer

MODTRAN – MODerate resolution atmospheric TRANsmission

NERC – Natural Environmental Research Council

RMSE – Root Mean Square Error

SLC – Scan Line Corrector

SLE – Sea Level Equivalent

TM – Thematic Mapper

6S - Second Simulation of a Satellite Signal in the Solar Spectrum

Variables

α – albedo

$\alpha_{ATMSolar}$ – ATM broadband albedo derived from conversion using solar spectrum measurements

α_{ATMFl} – ATM broadband albedo derived from FLAASH atmospheric correction

α_{etmdp} – ETM+ broadband albedo derived from dark pixel correction

α_{etmfl} – ETM+ broadband albedo derived from FLAASH atmospheric correction

α_{etm6} – ETM+ broadband albedo derived from 6S atmospheric correction

$\alpha_{shortsnow}$ – shortwave broadband albedo

a – pixel value

a,y – pixel along track position

c – empirical constant

d – Earth-sun distance

$ESUN_\lambda$ – Mean exoatmospheric solar irradiance

E_0 – Spectral irradiance

$\vec{I}$ – Stokes vector

I – intensity of radiation

I_i – irradiance

I_r – radiance

L(a) – fitted mean radiance for a given view angle

L(a=0) – fitted mean radiance at nadir

L'(a,y) – corrected radiance

L_λ – Spectral radiance at the sensor's aperature

L* – spectral Radiance

S – spherical albedo of the atmosphere

L^*_a – radiance backscattered by the atmosphere

$LMIN_\lambda$ – Spectral at-sensor radiance that is scaled to Q_{calmin}

$LMAX_\lambda$ – Spectral at-sensor radiance that is scaled to Q_{calmax}

LW – net Longwave radiation flux

M – energy used to melt ice or freeze water

Q – perpendicular polarisation of electromagnetic radiation

Q_{cal} – Quantised calibrated pixel value

Q_{min} – minimum recordable digital number

Q_{max} – maximum recordable digitable number

QE – latent heat transfer

QH – sensible heat transfer

QR – Energy from rain

QT – energy used for temperate change in the ice

S_{R+A} – spherical albedo

SW – net shortwave radiation flux

SW_{in} – incoming solar radiation

SW_{out} – outgoing solar radiation

T_g – gaseous transmission

T_{R+A} – transmission of the molecules and aerosols

U – parallel polarisation of electromagnetic radiation

V – elliptical polarisation of electromagnetic radiation

v – view zenith angle

ϕ – relative azimuth angle

ρ – reflectance

ρ_e – average surface reflectance for the pixel and the surrounding region

ρ_λ – at-sensor spectral radiance

ρ_{TOA} – Planetary TOA reflectance

ρ_R – molecular scattering intrinsic reflectance

ρ_{R+A} – intrinsic reflectance of molecules and aerosols

Θ_s – Solar zenith angle

1. Introduction

1.1 Background theory

Throughout the Quaternary, glaciers and ice sheets have undergone periodic expansion and retreat as a result of global climate change. These fluctuations in the mass of the cryosphere have led to significant changes in global sea level (IPCC, 2007). The loss of current ice sheet mass has been a specific recent concern due to their potential to raise sea level by over 70m (Anderson, 1999). At present, however, 60% of sea level rise is the result of valley glacier and ice cap (GIC) losses due to their more rapid response to climatic perturbations at the timescale of decades to centuries (Meier et al., 2007). Estimated to have a volume of between 0.35±0.07m sea level equivalent (SLE) (Grinsted, 2013) and 0.60±0.07m (Radic and Hock, 2010), GICs are projected to contribute 0.124±0.037m to global sea level by 2100 (Radic and Hock, 2011). The contribution of glacier and ice caps to global sea level rise, in addition to other factors such as the steric effect (Ishii et al., 2006), is extremely important given that 33.5% of the world's population currently lives within 100m of current sea level (Bell, 2008).

At a local level, the mass balance of GICs has a major influence on the surrounding region due to their role in the hydrological system (Ribstein et al., 1995). Glaciers provide both an important source of fresh water in mountainous regions and further down the drainage system for large populations in terms of both drinking water and agriculture (Barry, 2011). Furthermore, glaciers have also been used as important source of energy generation in mountainous regions in which they also influence the flood regimes of some systems (Thorson, 2009; Dahlke et al., 2012). Understanding the mass balance of these environments is therefore crucial in order to inform future environmental and industrial planning policy, in addition to managing geomorphological hazards related to their changing state (Richarson and Reynolds, 2000; Arendt et al., 2002; Varone et al., 2002; Hubbard et al., 2005; Benn et al., 2012).

Mass balance is defined as the gain and loss of mass in part or all of the glacier system over a specified period of time (Benn and Evans, 2010). Glaciers gain ice through the accumulation of snow and ice through precipitation onto the glacier surface itself and from the transfer of snow from surrounding areas through avalanching and aeolian processes (Paterson, 1994). Output, or ablation, is the loss of snow and ice through melting, sublimation and evaporation or mass loss from calving.

Where inputs exceed losses glaciers are able to grow, storing greater amounts of water. This stored water is subsequently released when the glacier reaches a state of negative mass balance.

Mass balance can be determined using a number of different methods. The direct ‘glaciological method’ uses direct measurements of accumulation and ablation through snow pits and ablation stakes drilled into the glacier (Braithwaite, 2002). The ‘hydrological method’ estimates the volume of water being stored in a glacier basin from net-precipitation and net-runoff; the results being interpreted as an indicator of mass balance (Braithwaite, 2002). In addition to these methods, geodetic and gravimetric techniques are increasingly being used. Both methods exploit remote sensing techniques and have been used increasingly over valley glaciers (Willis et al., 1998) and more recently for the Greenland and Antarctic ice sheets (Zwally et al. 2002; Chen et al., 2005, 2008).

Combined with these methods of mass balance measurement, numerous attempts at modelling glacier surface mass balance have also been made using models forced by climatic variables. Three main types of modelling are used. Statistical modelling typically uses correction and regression techniques for variables such as precipitation, minimum and maximum air temperatures, and uses them to predict variations in glacier average annual mass balance (Letreguilly, 1988; Moore and Demuth, 2001). In spite of this technique revealing the roles of individual variables in controlling mass balance, it is unable to account for spatial variability over glacier surfaces. Furthermore, the treatment of variables as independent excludes feedback mechanisms that may be in operation and thus prevent extrapolation of results to other glaciers or in to the future (Hooker and Fitzharris, 1999).

These drawbacks mean that degree-day and energy balance modelling approaches are used more frequently. Degree-day glacier mass balance models allow the calculation of accumulation, ablation and net mass balance from simple climate variables (Anderson et al., 2006). Parameters such as temperature and precipitation gradients are used in combination with degree-day factors for snow and ice melt to calculate mass balance. Unlike most statistical models, they can be used to calculate spatial variability in mass balance with elevation or across a grid (Laumann and Reeh, 1993). Lastly, energy balance approaches allow the calculation of accumulation and ablation separately, although degree day approaches do also allow this. Using the energy balance technique, ablation can be calculated at individual locations using site specific factors, making them better suited to take into account large spatial and temporal variability that is seen across glacier surfaces (Brock and Arnold, 2000). It is with this last approach in mind that this study has originated with remote sensing playing a key role in providing data with which to calibrate and evaluate models (Bishop et al., 1998; Klok and Oerlemans, 2002).

Models of glacier energy balance are primarily concerned with the surface energy balance which is the net sum of incoming and outgoing energy fluxes between the glacier surface and the atmosphere. It is defined by:-

$$SW + LW + QH + QE + QR - QT - M = 0 \tag{1.1}$$

where SW is the net shortwave radiation flux, LW is net longwave radiation flux, QH is sensible heat transfer, QE is latent heat transfer, QR is energy from rain, QT is energy used for temperature change in the ice, and M is energy used to melt ice or freeze water (Benn and Evans, 2010). Shortwave radiation consists of electromagnetic radiation in the ultraviolet, visible and near-infrared parts of the spectrum and is derived primarily from the sun (Rees, 2013), whilst longwave radiation is emitted by the atmosphere and the surrounding terrain and is dependent on their temperature. It is this energy balance that predominantly controls the summer mass balance of land terminating glaciers in temperate and sub-polar regions.

Energy balance studies of Arctic glaciers have shown that net-radiation is the dominant contributor of available energy for melting glacier snow and ice (Ardent, 2000; Guðmundsson et al., 2003). In particular visible and near infrared radiation can provide up to 99% of available energy (Arendt, 1999). The amount of energy made available to the glacier from shortwave fluxes is therefore critical and is controlled by the albedo, i.e. reflectivity, of the glacier surface. Albedo is defined as the proportion of shortwave radiation reflected from a surface, given by:-

$$\alpha = I_r/I_i \tag{1.2}$$

where I_r *and* I_i are radiance and irradiance respectively (Cuffey and Paterson, 2010). Thus, surface albedo is a key parameter in energy balance modelling designed to estimate the extent of glacier melt (Brock et al., 2000; Arnold et al., 2006).

Glacier snow and ice albedo depends on a number of factors; these include the solar incidence angle, snow grain size and geometry, impurities in the snow and ice, water content and surface topography (Steffan et al., 1993). Importantly, glacier albedo is not constant but evolves temporally as snow falls, ages and melts and spatially on a scale in the order of meters (Arnold and Rees, 2003). Fresh snow can have an albedo of over 0.9 whilst ice can range between ~0.4 and ~0.1 depending on the debris content (Röthlisberger and Lang, 1987; Paterson, 1994). Monitoring surface albedo and snowline migration is therefore a key component of mass balance studies and has been carried out in a range of environments in combination with seasonal temperature changes (Klok and Oerlemans, 2002; Box et al., 2006, 2012; Tedesco et al., 2011). This is an area where multispectral remote sensing can play a prominent role.

1.2 Background to remote sensing

"Remote sensing is, broadly but logically speaking, the collection of information about an object without making physical contact with it (Rees, 2013: 1)". In terms of remote sensing of the Earth, this translates to the extraction of information about the Earth's surface or atmosphere using electromagnetic radiation from airborne and spaceborne platforms (Campbell, 2002; Rees, 2006). Remote sensing has particular advantages for cryospheric remote sensing as it allows both large spatial and regular temporal coverage whilst limiting the cost and risk associated with repeated field measurements (Aniya et al., 1996; Paul et al., 2004; Boyd, 2009). Cryospheric remote sensing research has therefore increased dramatically due to concerns about climate change as it provides the ideal solution for obtaining data from otherwise inaccessible areas (Campbell, 2002)

Whilst many different satellite and airborne remote sensing systems exist, glacier surface characteristics are often extracted from multispectral imagery (Pellikka and Rees, 2010). Multispectral sensors are passive imaging systems recording reflected electromagnetic radiation from the surface of the Earth simultaneously over a number of wavelengths and are defined by their spatial, spectral, radiometric and temporal resolutions (Rees, 2006). In terms of monitoring albedo evolution, if narrow to broadband transformations can be made, spatial and temporal resolutions thereby become the crucial factors in cryospheric monitoring projects. The appropriateness of individual sensors for such studies ultimately depends on whether the resolution of individual pixels is sufficient to capture surface variability needed for energy balance modelling.

Modelling surface albedo in energy balance models is extremely complicated as it is exceedingly difficult to quantitatively relate albedo variations to their causes. Opposing factors may influence the local conditions in different ways (Hock, 2005). For glaciers, snow and ice albedo is treated differently as a consequence of their absolute difference and their differing temporal variability. Frequent attempts at modelling snow albedo have been made, often using grain size, atmospheric controls or the time since last snowfall (Warren and Wiscombe, 1980; Choudury and Chang, 1981; Brock et al., 2000). Fewer attempts have focussed on ice albedo (Oerlemans, 1992; Cutler and Munro, 1996; Brock et al., 2000). Remote sensing provides a means of validating these models of changing surface albedo, assessing the spatial resolution needed in order to accurately model the surface energy balance. Consequently accurate derivation of albedo data is a critical component of future surface mass balance modelling studies (Greuell et al., 2002).

In addition, remote sensing data can also be used to classify different surface facie and margin position. Facie identification is important as glacier surfaces exhibit a range of zones from the glacier margin to the accumulation area, from wet and dry snow to clean and dirty ice (Williams et al., 1991). Identification of different glacier facies is important as they are associated with different mass balance characteristics. In the accumulation area, the facie type present includes dry snow, wet snow, slush and superimposed ice, whilst in the ablation zone the facie type is dominated by clear and dirty ice (Cuffey and Patterson, 2010). Therefore identification of these different surface types can be used to accurately assess melt characteristics throughout the ablation season as facie zones migrate up-glacier (Kakhonovsky and Breon, 2012). In terms of margin location, multispectral imagery can be used to monitor temporal changes in terminus location and which can therefore be used as a proxy for long term temporal trends in mass balance (Kachouie et al., 2012). Information about the temporal evolution of glacier surfaces, both interannually and intra-annually is therefore a key parameter for building energy balance models.

In order to use surface reflectance data from multispectral sensors, a certain number of criteria must be met. First, the variable being measured must be the radiance reaching the sensor; this is normally achieved automatically using pre-launch calibrations (Rees, 2006). Second, any atmospheric effects must be removed. Remotely sensed values of surface radiance must be corrected for absorption and scattering, the latter of which is represented in Figure 1.1:-

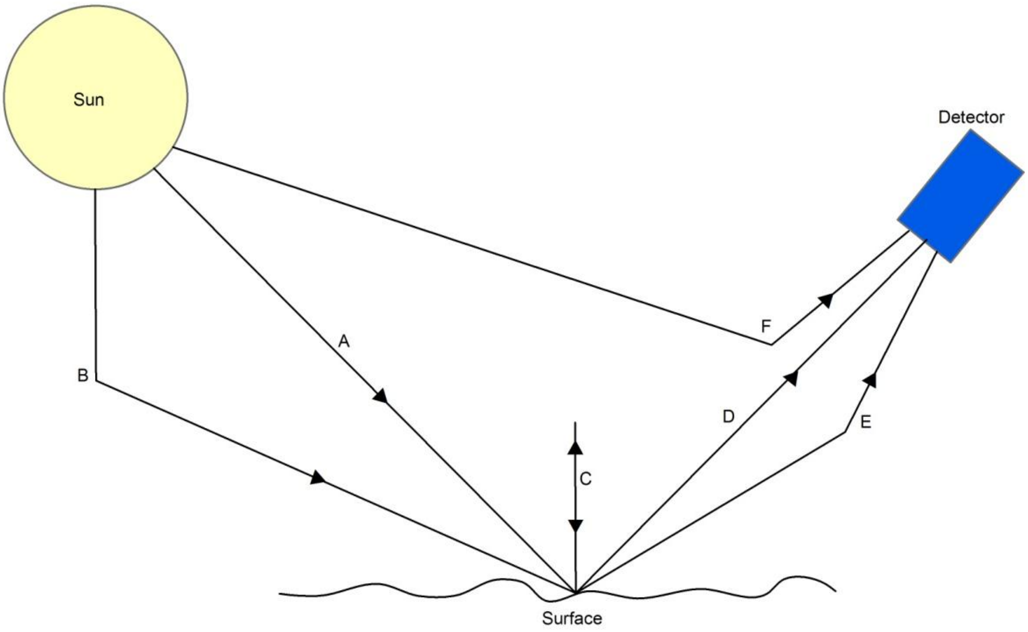

Figure 1.1: Contributions to the radiance measured at a sensor in the presence of atmospheric scattering (Rees, 2006).

In Figure 1.1, A is representative of direct illumination of the surface by the Sun, which B shows can also be illuminated by radiation that has been scattered from the atmosphere. Rays C to E show the possible destinations of radiation scattered from the surface. In C it has been scattered back to the surface; in D it is transmitted directly to the sensor; and in E it also reaches the sensor, having been scattered by the atmosphere (Rees, 2006). In addition to these processes, some photons are absorbed by aerosols or atmospheric gases (principally O_3, H_2O, O_2, CO_2, CH_4, and N_2O). Our ability to remove these effects either through physical models, calibration targets or simple empirical methods controls the accuracy of remotely sensing surface reflectance data (Rees, 1999; 2006).

Calculation of the impacts of atmospheric propagation is needed in order to derive a precise albedo value but in order to understand the reflective characteristics of the surface fully a number assumption and definitions of albedo must first be acknowledged. Measuring albedo is inherently complicated by the anisotropic scattering properties of snow and ice, which increases both with the wavelength of the incoming radiation and with the solar zenith angle (Knap and Reijmer, 1998; Greuell and de Ruyter de Wildt, 1999; Li et al., 2007). Previous studies have overcome this problem by assuming that radiometer measurements, measurements of reflected radiation in only one direction, are representative of reflectance as a whole due to the surface being a Lambertian scatterer (Knap et al., 1999; Schaepman-Strub et al., 2006; Gardner and Sharp, 2010). Using this assumption, many studies consider hemispherical-directional reflectance (HDR, Schaepman-Strub et al., 2006), where irradiance is measured in all directions whilst radiance is only measured at a point, to be bihemispherical reflectance (BHR). BHR is defined as the ratio of radiant flux reflected from a unit surface area into the whole hemisphere to the incident radiant flux of hemispherical angular extent and will be referred to as albedo from this point on. Assuming a Lambertian surface during this study is critical in order to compare the different data sets, however, the introduction of an error of up to 0.15 will be acknowledged in the results (Choudhury and Chang, 1981; Kuhn 1985; Knap et al., 1999; Li et al., 2007).

Previous studies attempting to measure and validate remotely sensed values of albedo and the different methods through which they can be derived have been mainly based on the use of ground-point surveys. These, however, have been limited by their lack of spatial and temporal resolution. In the case of spatial resolution, point measurements have been used to validate measurements for entire pixels (Knap et al., 1999; Reijmer et al., 1999; Greuell et al., 2002; Liang et al., 2005; Stroeve et al., 2005; Pope, 2012). Despite their frequent use, point measurement validations are fundamentally inappropriate except where the surface in question is relatively homogeneous in terms of its surface reflectance characteristics. This is not the case for many glaciers and ice caps, thereby calling into question validation studies that have been previously carried out.

1.3 Study Aims

This study will study to use a high resolution data set produced from an airborne multispectral scanner to derive reflectance characteristics of a highly heterogeneous glacier surface which can be compared to satellite imagery. The study site chosen for this exercise is Langjökull as it provides both large relatively homogenous areas, in addition to highly variable surfaces near the margins of the ice cap. Moreover, whilst validating satellite imagery, it should also provide information as to the appropriate resolution that surface energy balance models need in order to properly incorporate surface variability.

The aims of this study therefore are as follows:-

Evaluate different methods of deriving surface reflectance characteristics from the same remotely sensed image.

Assess the spatial variability of albedo over the surface of Langjökull.

Assess the ability of different spatial resolution datasets to accurately capture surface albedo.

Assess the suitability of scientific products derived from different satellite platforms for evaluating surface energy balance models.

2. Study site

The study site for this investigation is Langjökull ice cap. It is the second largest ice cap in Iceland with and area of about 925km^2, and is located at about 64.7^{0}N and about 20.4^{0}W in southwest Iceland. Elevations across the ice cap range between 450 and 1450m a.s.l. with an average height of 900m a.s.l. (Guðmundsson et al., 2003). The surroundings of Langjökull are comprised of lava, sand and proglacial lakes (Sigurðsson, 1990) and while two major rivers drain meltwater from the ice cap, a significant proportion of the meltwater drains directly into the substrate to feed groundwater aquifers (Guðmundsson et al., 2009).

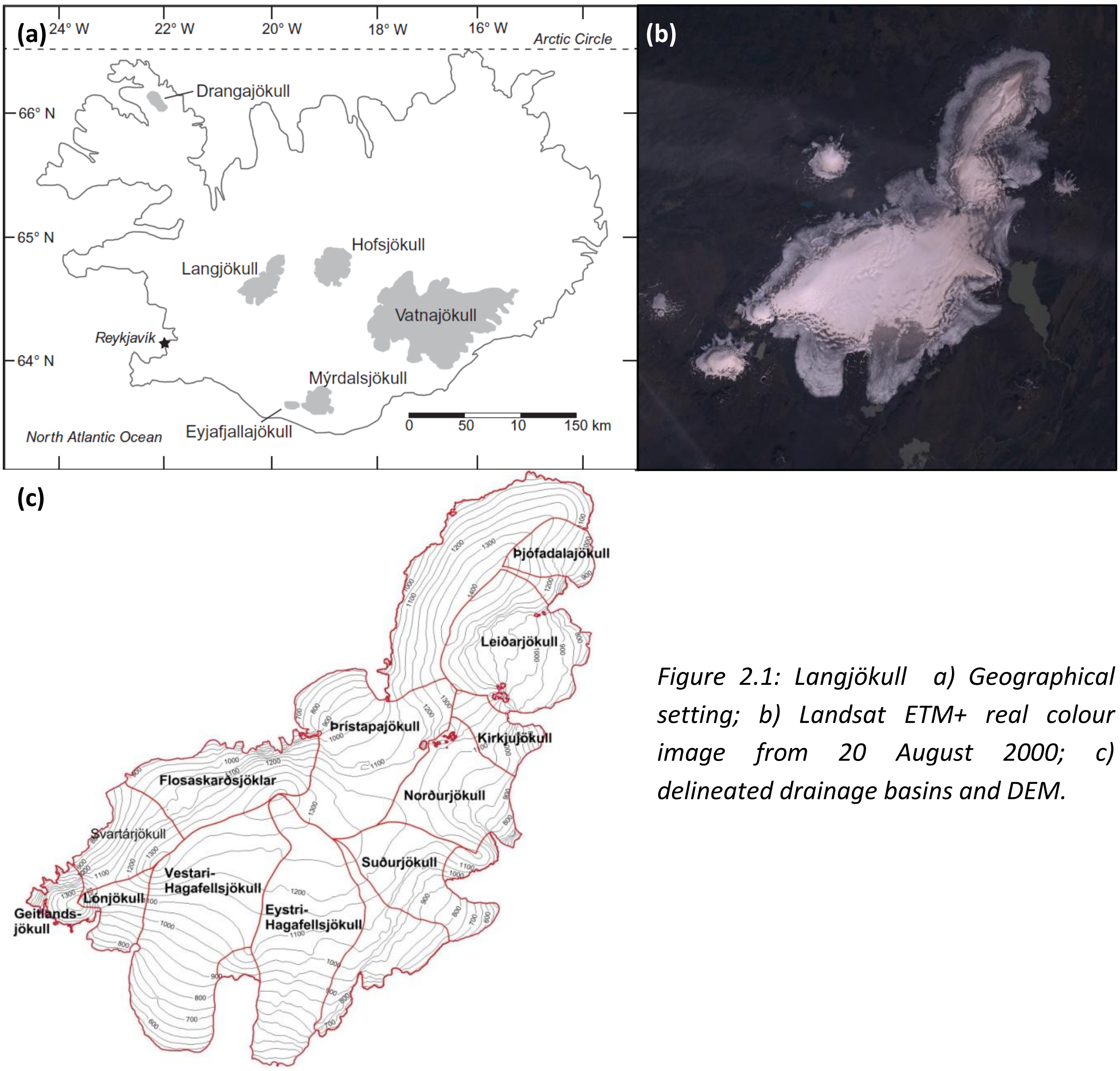

Figure 2.1: Langjökull a) Geographical setting; b) Landsat ETM+ real colour image from 20 August 2000; c) delineated drainage basins and DEM.

Most of Langjökull is land terminating with only outlet glacier Norðurjökull to the east and part of the outglacier Eystri-Hagafellsjökull in the south terminating at calving margins in lakes (Figure 2.1). Thus, the mass balance of the ice cap is controlled primarily by the balance between snow and accumulation of melting and evaporation. Langjökull receives on average 3,500mm precipitation per year, with a peak value of 4,000mm over the northern dome (Björnsson and Pálsson, 2008). This precipitation is derived primarily from cyclones crossing the North Atlantic and falls mainly as snow at higher altitudes throughout the year due to the average surface air temperature being close to or below freezing. At lower elevations the ablation season typically lasts for four months from late-April to mid-September (Guðmundsson et al., 2003). Energy balance and degree day modelling studies during the ablation season have demonstrated that incoming short-wave solar radiation provides the highest contribution to the total surface melt energy, equalled or surpassed, only on occasion by peaks in latent and sensible heat during spells of high temperatures and strong winds (Guðmundsson et al., 2003). These events are principally the consequence of solar radiation heating up the low-albedo areas outside the ice-cap generating high lateral temperature gradients between the melting glacier surface and the surrounding areas, producing katabatic wind downslope (Guðmundsson et al., 2003). Thus, the albedo of both the glacier surface and the surrounding landscape, particularly the drop in albedo that occurs when low elevation snow has melted and the summer surface is exposed, play a crucial role in determining the mass balance of Langjökull (Björnsson and Pálsson, 2008). Importantly, this relationship also means that small positive winter mass balances can lead to high negative summer mass balance as lower albedo surface are revealed earlier in the ablation season.

In spite of the delicate balance of Langjökull’s mass balance, reconstructions of glacier dynamics and extent have demonstrated that the response of the ice cap and its outlet glaciers has been sluggish during the Holocene. Moraine chronologies have demonstrated that over the last 5000 years the ice cap has grown slowly in response to deteriorating regional climate (Kirkbride and Dugmore, 2006). This trend is has been supported by the palaeoclimatic record from the GISP2 ice core which shows a depletion of $\delta^{18}O$, and therefore air temperature, over the last 3500 years for the North Atlantic region (Stuiver and Grootes, 2000). The volume and extent of Langjökull peaked during the Little Ice Age in 1840, with a secondary peak around 1890 (Flowers et al., 2007). Both the volume and extent of the ice cap have since declined; the Little Ice Age peak volume and area estimated to be 10% and 5% greater respectively than their 2007 equivalents.

Despite the slow response shown by Langjökull during the Holocene, modelling studies have shown that recent climatic changed together with albedo feedback mechanisms have led to rapid mass balance changes and that these are likely to accelerate over the next century (Björnsson and Pálsson, 2008). Moreover, the ice loss acceleration is expected to be greater than that seen on either Vatnajökull or Hofsjökull (Björnsson and Pálsson, 2008). Principally this response is the result of increasing air temperatures and the melt accelerating albedo feedback coupled with the local underlying topography. Model results show that increasing air temperatures will cause a reduction of the accumulation area as snow melts earlier in the year exposing the lower albedo glacier surface to melting for longer periods of time; this in turn leads to a reduction in the elevation of the ice surface. Whilst the elevation of the ice surface of most of the ice caps in Iceland is a by-product of ice thickness and high underlying topography, the surface elevation of Langjökull is entirely dependent on ice thickness. The accumulation of snow due to lapse rates associated with increasing elevation on Langjökull is therefore controlled by the thickness of the ice. Thus a negative mass balance induced by higher temperatures and lower surface albedo will result in a positive feedback as the surface elevation will be reduced, increasing temperatures further and reducing the volume of deposited snow. A run away thinning of the ice cap will therefore occur due to less snowfall occurring whilst the rate of melt in the ablation area increases (Björnsson and Pálsson, 2008; Flowers et al., 2007). Understanding albedo variations on the ice cap is therefore crucial to modelling mass balance change making calibration of models using remotely sensed albedo values critical in understanding regional response to changing climate.

3. Methodology

3.1 ATM

The primary focus of this study is the Airborne Thematic Mapper dataset which was obtained through collaboration with the UK Natural Environmental Research Council (NERC) Airborne Research and Survey Facility (ARSF). The ARSF flew a campaign over Langjökull on 2nd August 2007, with the Daedalus 1268 passive multispectral scanner mounted inside the ARSF's Dornier 228 aircraft. Between 14:21 and 17:50 GMT the whole of Langjökull was imaged in 24 separate, overlapping strips in 11 wavelength bands in the visible, near, short and thermal infrared regions of the electromagnetic spectrum as listed in Table 3.1. The output of these 11 spectral bands was a 16-bit digital output with up to 65,536 digital intensity levels (NERC Airborne Research Facility website, 2013).

Channel	**Wavelength (nm)**
1	420-450
2	450-520
3	520-600
4	600-620
5	620-690
6	690-750
7	760-900
8	901-1050
9	1550-1750
10	2080-2350
11	8500-13000

Table 3.1: ATM band information.

Data from each of the flight lines went through a series of pre-processing steps before delivery as at-sensor calibrated radiance (Level 1B) Hierarchical Data Format (HDF). The raw data were reformatted at the original resolution of the image files with ancillary files appended. Subsequently, using data from pre-flight calibration, radiometric correction was carried out in order to produce radiance data. The final processing carried out to produce the Level 1B product was to append locational and navigational information taken at the time that each of the flight lines was flown in a geodetic (latitude, longitude, spheroid, height, pitch, role and heading) and GPS datum (WGS84) (Azimuth Systems, 2005).

Before the swaths were orthorectified, swath corrections were applied to the files. Swath correction is a critical step when using airborne data generated from an instrument with a wide field of view ,as the data can exhibit radiances with substantial viewing angle dependence due to illumination, atmospheric corrections, and the BRDF of different objects (Kennedy et al., 1997; Palubinskas et al., 2003b). Usually these corrections are derived by a physical model using *in situ* field measurements taken during the acquisition of the data. However, no atmospheric or *in situ* measurements were carried out at the time of individual flight lines and thus an empirical correction was needed to ensure the data were radiometrically homogeneous (Palubinskas et al., 2003a, 2003b; Zhao et al., 2005). To achieve this, a multiplicative correction based on a 5th order polynomial was fitted to each swath (Eq. 3.1), having taken the average brightness for each cross-swath pixel for each entire flight line.

$$L(a) = c1a^5 + c2a^4 + c3a^3 + c4a^2 + c5a + c6 \qquad (3.1)$$

where L(a) is fitted mean radiance for a given view angle. Knowing that the view angle effects are zero when the view angle is zero, compensation factors were calculated to normalise each view-angle to the nadir view using a multiplicative compensation factor:-

$$Kmult = L(a)/L(a = 0) \qquad (3.2)$$

where L(a=0) is the fitted mean radiance at the nadir. Having established a multiplicative compensation factor, each pixel was defined in terms of it along track dimension of the image at position (a,y) and was assigned a corrected radiance L'(a,y) using the following empirical correction:-

$$L'(a, y) = L(a, y)/\ Kmult(a) \qquad (3.3)$$

where a=0 was defined as the centre (Kennedy et al., 1997; Palubinskas et al., 2003b).

The corrected Level 1B swaths were subsequently subjected to Level 3A processing using AZGCORR which corrected the image data and interpolated an output image on a regular grid in a recognised map projection coordinate space aligned at a fixed spheroid height. Furthermore, it was at this stage that the ground spatial resolution (pixel size) of the ATM data was defined. The spatial resolution was controlled by the optical characteristics of the scan head, which provides the instantaneous field of view (IFOV), and the aircraft altitude. These factors combine to control pixel length and width as they are defined by the IFOV and the scan angle away from nadir (Callison et al., 1987). In terms of the Daedalus 1268, with a scan rate of 2.5mrad the physical ground resolution is given by:-

$$Resolution = (Aircraft\ altitude - Surface\ elevation) \times 2.5\ \times 10^{-3} \qquad (3.4)$$

For all of the ATM swaths produced, the spatial resolution is about 5m. For greater details regarding the techniques used to produce the Level 3 product see the Azimuth Systems AZGCORR User Guide (Azimuth Systems, 2005).

3.1.1 Georeferencing

Having produced the Level 3A product, the swaths were individually geolocated. This step was crucial to this study in order to allow comparison between images from different satellite platforms as well as accurate comparison of the ATM data with the satellite images (Reijmer et al., 1999). Furthermore, analysis of the effects of varying spatial resolution was reliant on precise execution of this process. As no ground measurements were taken during the airborne survey, the decision was taken to georeference all images to an ETM+ image collected prior to 2 August 2007, the date on which the ATM data were collected. An ETM+ image was chosen because of the well known accuracy of the method used to locate Landsat-7 imagery using the spacecraft altitude and ephemeris which are incorporated into the data upon download (Storey et al., 2008). Proven to have an accuracy before 2004 of between 30 and 40m through ground control point studies (Lee et al., 2004; Tucker et al., 2004), an ETM+ image from 20th August 2000 was chosen due to the high absolute accuracy of its geolocation and the relatively cloud free nature of the image.

Having established a base image, each of the ATM swaths was located approximately, using information derived from the AZGCORR processing. Specifically, the geographic projection (WGS84, UTM27N), resolution (5m), and the X, Y limits of each image were applied using ERDAS Imagine software. Subsequently, the images were flipped vertically to give the correct alignment before ground control points were used to geolocate precisely each of the image swaths. Control points, which redefined the location of the pixel centres, were selected on the basis of being low variability features and were principally located in the proglacial area. Lake margins were often used, justified on the basis that they were less likely to have a large annual and inter-annual variability, in addition what appeared to be the more static margin areas of the ice cap itself. The process for one of the swaths can be seen in Figure (3.1).

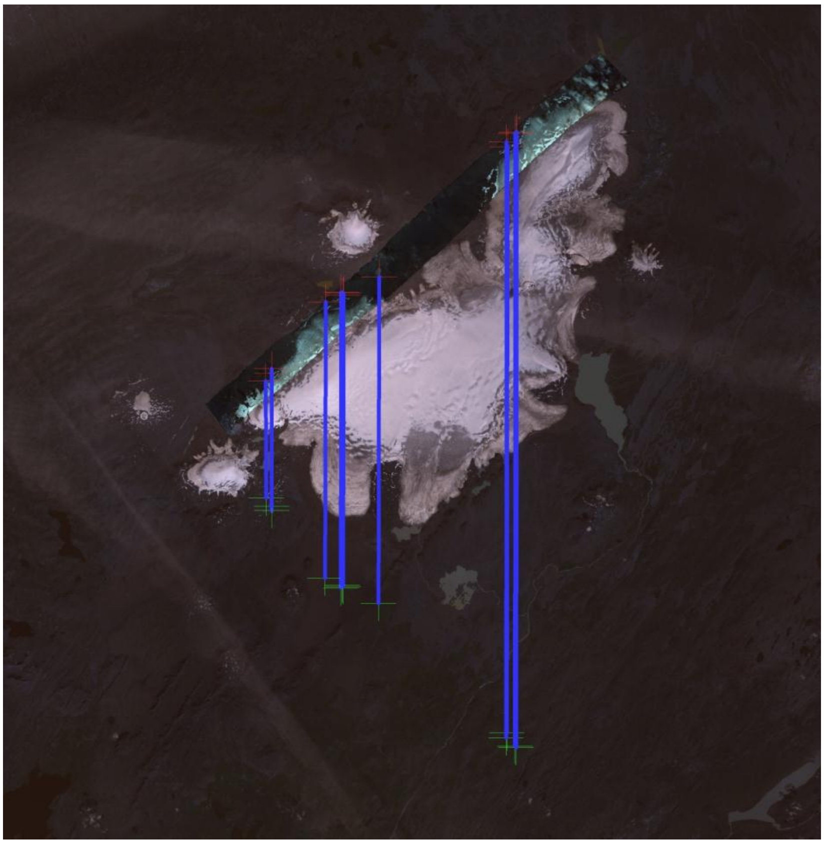

Figure 3.1: Georeferencing ATM swath a214e031. Green crosses show the original location of each pixel used as a control point with connected red crosses showing the final position of each pixel once the image had been flipped vertically due to the programme assuming the wrong north-south orientation of the image.

3.1.2 Surface reflectance using the solar spectrum of Langjökull

Having georeferenced each of the ATM swaths, the ATM spectral radiance values for each band needed to be converted to reflectance values. The first method used to achieve this used measured ground based *in situ* spectra to convert the ATM data. This is a relatively simple method of deriving surface reflectance values, incorporating two possibly significant assumptions. First, it ignores any atmospheric influence between the ground surface and the sensor; second it assumes that the *in situ* measured irradiance values were the same irradiance values that would have been measured at the same time the surface reflectance values were derived by the ATM. Despite these assumptions, it is crucial to assess whether this relatively simple technique can produce sufficiently accurate surface albedo values.

The spectra used in this part of the study were HDR spectra (Schaepman-Strub et al., 2006) and were collected in August 2011. They were measured with an ASD FieldSpec Pro which was on loan from the UK's Natural Environment Research Council's Field Spectroscopy Facility (FSF). The FieldSpec has a spectral range of 350-2500nm, a sampling interval of 1.4 nm (350-1000nm) or 2nm (1000-2500nm), and a spectral resolution (FWHM) of 3nm at 700nm, 10nm at 1400nm, and 12nm at 2100nm. The spectra were all subsequently resampled to 1nm. Spectra were collected following procedures suggested by the FSF (MacArthur 2007a, 2007b, 2007c; Milton et al., 2009; Goetz, 2012; Pope, 2013).

All spectra were collected with a Spectralon panel with the data being stored to be subsequently processed using tools provided by the FSF. Of the spectra measurements collected, only those taken under cloudless conditions were used in order to replicate the conditions under which the ATM data were collected. The first stage of post processing the Raw Digital Number (DN) data was to use the FSF 'Excel Template for ASD Raw (DN) Reflectance Data Files' spreadsheet in order to extract and format an ASD ASCII file for use in subsequent analysis. The second stage was to use the 'ASD Excel Template for Calculating Spectral Radiance and Irradiance' to produce calibrated radiance and irradiance values for each set of measurements. Having input configuration parameters, specific to the Spectralon panel that was used, the spectral data from the ASD ASCII worksheet were normalised using the coefficients derived from the first stage of processing. For the Spectralon panel that was used three different gain settings were specified. From 350-973nm the normalising coefficient was 68, from 974-1785nm the normalising coefficient was 58.514 and from 1785-2500nm the normalising coefficient was 128.

Utilising the normalised coefficient values and the unique radiance calibration file generated from pre-use calibration of the equipment, spectral radiance values between 350nm and 2500nm were generated at a spectral resolution of 1nm. These values were calculated thus:-

$$L_{\lambda} = \frac{'ASDASCII\ File' \times Radiance\ Calibration\ File}{Normalised\ Coefficient} \tag{3.5}$$

where L_{λ} is radiance per nm. Having generated a radiance value the excel macro subsequently produced an irradiance value and thus the value of incoming solar radiation at each wavelength. This is achieved via the following algorithm and facilitates the calculation of reflectance from the ATM radiance values:-

$$E_0 = \frac{L_\lambda \times \pi}{Panel\ Calibration\ File\ Value} \tag{3.6}$$

From these data it is possible to derive reflectance values from the ATM data for the ice cap surface by calculating a weighted average for each of the ATM bands according to their spectral response across the solar spectrum (Guo et al., 1997). Provided by the ARSF, the spectral response of the first eight ATM bands is displayed in Figure 3.2.

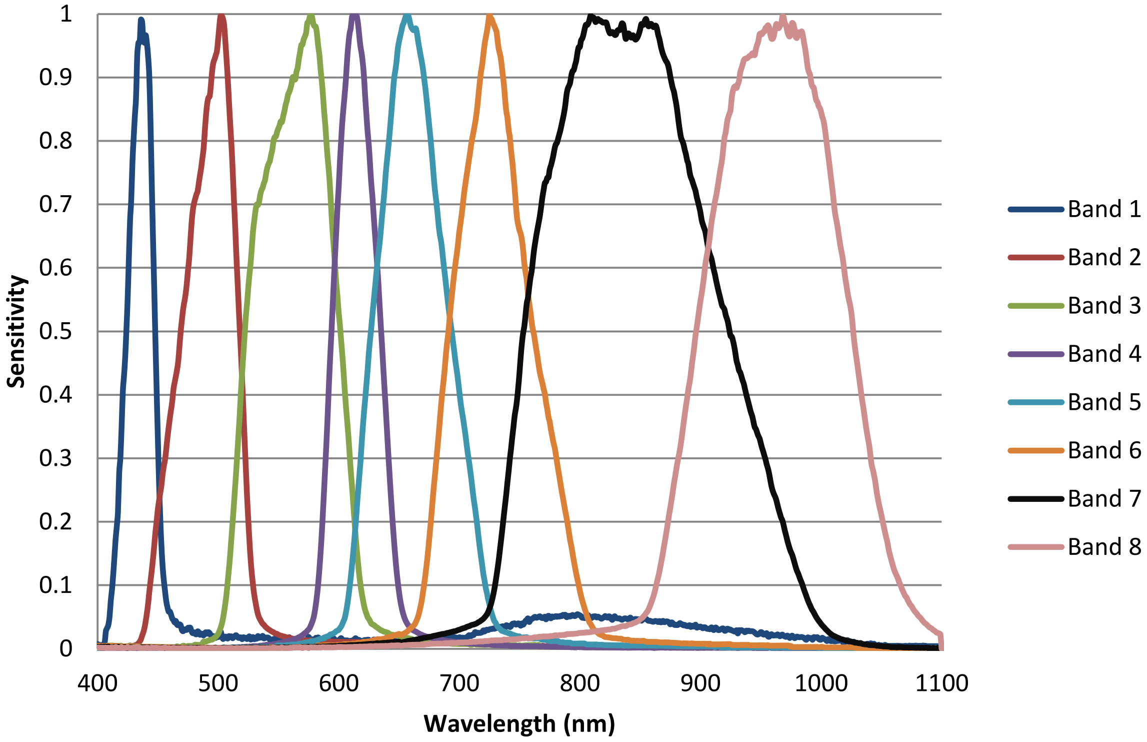

Figure 3.2: Spectral response of ATM bands 1-8.

The derivation of a weighted average for each of the ATM bands was achieved by first multiplying the irradiance value per nanometer generated by Equation 3.6 for a set of solar spectrum measurements by the ATM bandwidth function for the corresponding wavelength. The sum of these values was then divided by the sum of the corresponding ATM band response values generating a weighted average for each band across the solar spectrum. For the set of measurements selected to be used in this study from which the irradiance figures were derived, the value of the weighted average for each band can be seen in Table 3.2.

Band	**Wavelength (nm)**	**Weighted Average ($mW/m^2/nm$)**
1	420-450	471.811
2	450-520	561.3221
3	520-600	564.845
4	600-620	524.902
5	630-690	498.1183
6	690-750	430.5049
7	760-900	380.9968
8	910-1050	596.7858

Table 3.2: ATM bands 1-8 and the generated weighted average for each of the bands.

Using these weighted average values for each of first eight of the ATM bands, reflectance values for each of the ATM bands was calculated from Equation 3.7. The ATM radiance values were divided by 1000 as this is what they were scaled to in the original data whilst the ‘weighted average’ values were divided by 10 in order to make these units comparable with the ATM values (Guo et al., 1997).

$$r = \left(\frac{ATM\,radiance}{1000} \times \frac{\pi}{(Weighted\,Average/10)}\right) \qquad (3.7)$$

ATM reflectance values calculated by this method will henceforth be referred to as ATMSolar.

3.1.3 Atmospheric correction

The second method used to generate surface reflectance from the ATM data was to use an atmospheric correction model to remove the impacts of atmospheric propagation and as a by-product convert radiance values to reflectance. This method was carried out to demonstrate the extent of atmospheric influence through comparison with ATMSolar values, and to generate an atmospherically corrected data set directly comparable with the corrected satellite imagery (Matthews et al., 2003; Azimuth Systems, 2005; Perkins et al., 2012). Atmospheric correction was carried out using Fast Line-of-sight Atmospheric Analysis of Spectral Hypercubes (FLAASH), which is supported by ENVI software. Whilst other models such as ATREM and ACORN carry out similar corrections, FLAASH was chosen specifically as it typically produces comparable if not better results (Kruse, 2004) and could be quickly applied to both the ATM swaths and the ETM+ data.

Developed by the Air Force Phillips Laboratory, Hanscom AFB and Spectral Science, Inc, FLAASH was intended to provide an accurate, physics based derivation of surface and atmospheric properties (such as albedo, surface altitude, water vapour column, aerosol and cloud optical depths and, surface and atmospheric temperatures), with minimal computational requirements (Adler-Golden et al., 1999; Perkins et al., 2012). Using MODTRAN4-based atmospheric correction, the desired atmospheric properties are derived from the spectral radiance for each image pixel using look-up tables that are generated from these simulations (Matthew et al., 2000; 2003). Operating in the 400-2500nm spectral range, where thermal emission is negligible, spectral radiance (L^*) at the sensor for each pixel is therefore able to be parameterised as shown in Eq. 3.8.

$$L^* = \frac{A\rho}{1-\rho_e S} + \frac{B\rho_e}{1-\rho_e S} + L^*{}_a \tag{3.8}$$

where ρ is the surface reflectance, ρ_e is an average surface reflectance for the pixel and the surrounding region, S is the spherical albedo of the atmosphere, $L^*{}_a$ is the radiance backscattered by the atmosphere and A and B are coefficients that depend on atmospheric and geometric corrections (Matthews et al., 2003). The first term in the equation corresponds to the radiance from the surface that travels directly to the sensor, while the second term corresponds to the radiance from the surface that is scattered by the atmosphere to the sensor (Adler-Golden et al., 1999). The distinction between ρ and ρ_e accounts for the adjacency effect (spatial mixing of radiance among nearby pixels) caused by atmospheric scattering (Adler-Golden et al., 1999).

The values of A, B, S and $L^*{}_a$ are determined from MODTRAN4 calculations that use the viewing and solar angles and the mean surface elevation of the image, as well as assuming a certain model atmosphere, aerosol type, and visibility (Kruse, 2004). The solar angles and the mean surface elevation were provided individually for each of the ATM images. The former was automatically calculated from the acquisition time of each swath in combination with the scene centre location. The latter was extracted from an ASTER GDEM of Langjökull obtained from ECHO Reverb. Lastly, the model allowed the sensor elevation above sea level to be input in order for its location within the modelled atmosphere to be taken into account.

One of the greatest impacts on the values of A, B, S, and $L^*{}_a$ is that of water vapour, which is often variable across each scene. FLAASH accounts for this variability by looping MODTRAN4 calculations over a series of water column quantities through the use of a spectral band centred in the region of the electromagnetic spectrum absorbed by water and a reference band outside of this, so that the quantity of water can be calculated on a pixel by pixel basis (Matthews et al., 2003). Unfortunately, the ATM did not have an absorption band and therefore a standardised atmospheric water vapour column had to be used for corrections. Provided as a MODTRAN Model Atmosphere the model used for the ATM data was the Sub-Arctic Summer model as specified by the MODTRAN latitude and date of acquisition guide (FLAASH User's Guide, 2009).

In addition to removing the effects of water vapour, FLAASH was also used to remove the impacts of aerosols from each swath using selected dark land pixels or very bright calibration targets in the scene. This method, based on ATM bands 5 and 10, relied on the observation by Kaufman et al. (1997) of an almost fixed ratio between the reflectances for pixels at 660nm and 2100nm of ~0.45 (Kaufman et al. 1997; Adler-Golden et al., 1999; Matthews et al., 2003). Whilst this method of aerosol remove appears more precise than the selection of an idealised water vapour model, it incorporates a crucial generalisation. A standardised aerosol model has to be chosen from a drop down list, and whilst the FLAASH user guide considers the choice of model not to be critical for high visibilities, errors may still be incorporated (FLAASH User's Guide, 2009). The model used for each ATM swath was the *Rural* model, which contends to "represent aerosols in areas not strongly affected by urban or industrial sources and which contains particles sizes which are a blend of one large and one small" (FLAASH User's Guide, 2009: 23). ATM reflectance values calculated by this method will henceforth be referred to as ATMFlaash.

3.1.4 Narrow to broadband (NTB) conversion

Having carried out the previous radiance to reflectance transformations, the narrowband spectral reflectance produced had to be converted to broadband albedo in order to produce the average reflectance of the surface (Rees, 2006). This was accomplished using an empirical relationship established by Knap et al. (1999) using band-2 and band-4 on Landsat-5's Thematic Mapper instrument and which was subsequently validated by Reijmer et al. (1999). It was deemed acceptable to use this empirical relationship for the ATM instrument because ATM bands 3 and 7 are spectrally comparable with Landsat-5 bands 2 and 4.The ATM broadband albedo ($\alpha_{ATMSolar,}$ α_{ATMFl}) was calculated thus:-

$$\alpha_{atm} = 0.726r_3 - 0.322r_3^2 - 0.051r_7 + 0.581r_7^2 \tag{3.9}$$

Although this formula is not appropriate for deriving broadband albedo off-glacier, it is suitable for deriving broadband albedo on both ice and snow surfaces. Therefore differentiation between glacier ice and snow for separate NTB formula appropriate for the individual surfaces is unnecessary (Reijmer et al., 1999). Furthermore, in the original study, the root square mean differences between modelled Landsat-5 broadband albedo and ground based measured broadband albedo were only 0.009, demonstrating that only small errors are incorporated into the data through this technique (Knap et al., 1999). Alternatively this study could have used the later empirical relationship derived by Greuell et al. (2002). However, preliminary tests of the two formulae showed values differed within the calibraton uncertainty of ±5% (Greuell and Oerlemans, 2004). This, in combination with the results of the Knap et al.'s (1999) conversion being previously validated on the Haut and Bas Glaciers d'Arolla, Switzerland and on Morteratschgletscher and Vatnajökull, the last of which is likely to have similar site characteristics to Langjökull, justified the use of this relationship.

3.2 Satellite instruments

3.2.1 Landsat-7

The first of the satellite instruments used by this study is the ETM+ instrument carried on Landsat-7 which measures reflected solar radiation across eight different spectral bands the details of which are in Table 3.3.

Band Number	**Wavelength Interval (nm)**	**Spectral Response**	**Spatial resolution (m)**
1	452-514	Blue-Green	30
2	519-601	Green	30
3	631-692	Red	30
4	772-898	Near Infrared	30
5	1547-1748	Shortwave Infrared	30
6	10310-12360	Thermal Infrared	30
7	2065-2346	Mid-Infrared	30
8	515-896	Panchromatic	15

Table 3.3: ETM+ band information.

Landsat-7 has a repeat interval of 16 days, a scene swath of 185km and an orbit inclination angle of 98.2^0 (Chander et al., 2009; Quincey and Luckman, 2009). When launched the ETM+ instrument was fitted with a Scan Line Corrector (SLC) which compensated for the forward motion of the satellite to ensure that subsequent scans were aligned with one another. However, as of May 2003, the SLC failed resulting in approximately 22% of data missing in a Landsat-7 scene. Whilst missing data points can be optionally filled in using other data products, in order for the different sampling techniques to be compared, it has been decided not to fill in the missing data in each scene during this study (USGS, 2010).

Surrounding the ATM acquisition date of 2 August 2007 Landsat-7 produced two images of Langjökull on on 14 July and 15 August. Although not ideal for comparison with the ATM data, the image generated on the 15 August was selected for this study as its acquisition date is temporally closer to both the acquisition date of the ATM data as well as the MODIS albedo product selected for this project (see section 3.2.2). This Landsat-7 image was acquired through EarthExplorer on the USGS website.

3.2.1.1 Surface albedo retrieval

Before the Landsat-7 image can be used to asses surface albedo a number of corrections need to be made to each image. The first corrections are made automatically during image pre-processing before acquisition occurs. In the case of the Level 1T product obtained for this study, radiometric correction, systematic geometric correction and precision correction using ground control chips are all carried out by an automated system (Roy et al., 2010). Further corrections are needed in order to accurately assess albedo including removal of noise interference resulting from the interaction of electromagnetic radiation with the atmosphere as well as adjusting the image as a consequence of the time of year of acquisition. These corrections carried out with the intention of deriving a precise and accurate surface albedo of Langjökull are described below.

3.2.1.2. Radiometric calibration

In order to detect and quantify changes to terrestrial environments, sensors need to be calibrated to ensure that they produce data of a known accuracy and precision and therefore enable consistent measurement of the Earth’s surface features through time (Chander et al., 2009). In order to achieve this the ETM+ sensor undergoes regular radiometric calibration as part of the generation of the Level-1 product by the automated system and therefore only at-sensor spectral radiance conversions need to be applied to the acquired images (Roy et al., 2010).

3.2.1.3. Manual processing to generate surface albedo

3.2.1.3.1 Conversion to at-sensor spectral radiance

The first stage needed to generate surface albedo through this method is to rescale the raw data values following the automated stage of calibration to form calibrated digital numbers (Q_{cal}). The main purpose of this processing step is to generate a physically meaningful common radiometric scale between different sensors on varying platforms (Chander et al., 2009). Q_{cal} numbers are generated during radiometric calibration by converting pixel values (Q) to units of absolute spectral radiance using 32-bit point calculations which are then scaled to 8-bit numbers for ETM+ (Q_{calmax} = 255) (Chander et al., 2009). Conversion from these figures back to at-sensor spectral radiance requires knowledge of the lower and upper limits of the original rescaling factor. Equation 3.7 is used to perform calibrated digital number (DN) to at-sensor spectral radiance (L_λ) for the Level-1 products that was obtained:-

$$L_\lambda = \left(\frac{LMAX_\lambda - LMIN_\lambda}{Q_{calmax} - Q_{calmin}}\right)(Q_{cal} - Q_{calmin}) + LMIN_\lambda \tag{3.10}$$

where

L_λ = Spectral radiance at the sensors's aperature [W/(m^2 sr µm)]
Q_{cal} = Quantized calibrated pixel value [DN]
Q_{calmin} = Minimum quantised calibrated pixel value corresponding to $LMAX_\lambda$ [DN]
Q_{calmax} = Maximum quantised calibrated pixel value corresponding to $LMAX_\lambda$ [DN]
$LMIN_\lambda$ = Spectral at-sensor radiance that is scaled to Q_{calmin} [W/(m^2 sr µm)]
$LMAX_\lambda$ = Spectral at sensor radiance that is scaled to Q_{calmax} [W/(m^2 sr µm)]

The spectral range, post-calibration dynamic ranges ($LMIN_\lambda$ and $LMAX_\lambda$) and the mean exoatmospheric solar irradiance ($ESUN_\lambda$) are summarised in the appendix.

3.2.1.3.2 Conversion to top-of-atmosphere (TOA) reflectance

Having converted the image to at-sensor spectral radiance the next step in deriving accurate surface albedos is to convert the spectral radiance to top-of-atmosphere (TOA) reflectance, also known as in-band planetary albedo. The purpose of this processing step is to remove any cosine effect generated by different solar zenith angles relating to changes to the sun's position at different times of the year. In addition, "it corrects for the variation in the Earth-Sun distance between different data acquisition dates" (Chander et al., 2009: 900) as well as compensating for different values of exoatmospheric solar irradiance arising from the spectral band differences (Chander et al., 2009). TOA reflectance of the Earth (ρ_{TOA}) is calculated thus:-

$$\rho_{TOA} = \frac{\pi \times L_\lambda \times d^2}{ESUN_\lambda \times cos\theta_s} \tag{3.11}$$

where

L_λ = Spectral radiance at the sensor's aperture [W/(m^2 sr µm)]

d = Earth-Sun distance [astronomical units]

ESUN$_\lambda$ = Mean exoatmospheric solar irradiance [W/(m^2 µm)]

Θ_s = Solar zenith angle [degrees]

Despite the need for this correction, it unfortunately incorporates errors relating to assumptions about surface anisotropy. For example, the radiation field over the surface of Morteratschgletscher, Switzerland, has been found to be strongly anisotropic and thus significant errors in satellite-derived albedos may arise from the assumption that the radiation field is isotropic (Knap and Reijmer, 1998:). However, in the absence of any other available data, the method will have to be used in this study, although it must be recognised that it will introduce errors into calculated values of surface albedo as a result. For Knap and Reijmer (1998), the error was an underestimate of the ice albedo of 0.05, independent of the magnitude of the albedo. In the case of snow, Suttles et al. (1988) found that the underestimation of snow albedo was smaller than that for ice under the same conditions. Both these errors, however, depend on the solar zenith angle and the view angle which may therefore lead to a greater error when observing the albedo on Langjökull due to its latitude (Reijmer et al., 1999).

3.2.1.3.3 Dark pixel correction

Lastly, in order to generate surface albedo, the effects of electromagnetic radiation propagation through the atmosphere need to be removed. The simplest and most widely applied means of doing this is through dark pixel subtraction (Rees, 2001). This correction procedure involves the identification of the minimum radiance pixel value for each of the bands in the image and then subtracting this value across all the pixels in the image (Campbell, 2002). The pixels that provide these zero-reflectance areas are often the result of shadows or in the near-infrared region of the electromagnetic spectrum, water bodies (Rees, 2001). The crude nature of this method does mean, however, that a number of assumptions have to be made. It assumes that the minimum radiance in an individual band is zero and that the atmospheric impact is uniform across the image, and whilst inspection of the images can determine the appropriateness of this technique, these assumptions must still be acknowledged (Lillesand and Kiefer, 2000; Rees, 2006). This straightforward method of deriving surface albedo will be used as a base from which to compare the other methods of surface reflectance derivation. ETM+ reflectance values calculated by this method will henceforth be referred to as LandsatDP.

3.2.1.4 Generating surface albedo from 6S

In contrast to the manual processing methods for generating surface albedo described in section 3.2.1.3, a second method is used which involves one of the freely available physical models for atmospheric correction. The model selected uses the 6S basic radiative transfer code (Vermote et al., 2006; Kotchenova and Vermote, 2007). The 6S code, which is also used for the calculation of lookup tables in the MODIS atmospheric correction algorithm (Vermote et al., 1997; 2002), allows accurate simulation of satellite and airborne observations through the modelling of a realistic atmosphere and the resulting absorption and scattering by different molecules (Kotchenova et al., 2006; Vermote et al., 2006).

The 6S code is based around a method of successive approximations of absorption, scattering and reflection within different levels in the atmosphere, radiative transfer equations being solved numerically for each layer. This is accomplished by breaking down the signal at the top of the atmosphere into four separate terms: i) photons which are directly transmitted from the sun to the target and directly reflected back to the sensor; ii) photons scattered by the atmosphere and then reflected by the target and directly transmitted to the sensor; iii) photons directly transmitted to the target but scattered by the atmosphere on their way to the sensor; and iv) photons which have at least two interactions with the atmosphere and one with the target itself (Vermote et al., 2006). These are equivalent to A, B-D, A-E and B-E in Figure 1.1 respectively. The first three terms are computed using the downward radiation field as given by the Successive Orders of Scattering method which uses the contribution of the atmosphere and an approximated BRDF using the hemispherical albedo of the target (Kotchenova et al., 2006; Vermote et al., 2006).

6S also includes the effects of electromagnetic radiation polarisation through the calculation of four components of the Stokes Vector, $\vec{I} = \{I, Q, U, V\}$, where the first component, *I*, describes the intensity of the radiation whilst the other three characterise perpendicular (*Q*), parallel (*U*), and elliptical (*V*) polarisations (Kotchenova et al., 2006). The degree, angle and ellipticity of polarisation are calculated from the last three components using mathematical formula (Coulson et al., 1960).

The Stokes parameters are specified according to the coordinate system associated with the direction of incident light propagation which can subsequently be adjusted using scattering events defined by molecular and aerosol phase matrices based on Rayleigh and Mie Scattering theories (Kotchenova et al., 2006). A schematic of the 6S process chain is presented below (Figure 3.3) whilst further details of the model are available from Vermote et al. (2006).

From this outline of the 6S radiative transfer code it is clear that the quantity and location of different atmospheric constituents are needed. These were provided for the ETM+ image on the 15th August 2007 by the “MODIS/Aqua Aerosol, Cloud and Water Vapour Subset 5-Min L2 Swath 5km and 10km V5.1” product. This product enabled total water vapour and aerosol optical depth to be derived for the Landsat scene. In addition to this product obtained from NASA’s Echo Reverb facility, the ASTER GDEM of Langjökull was also acquired as an addition input in order to facilitate the correction of geometric effect to be made as part of the LandCor processing chain (Zelazowski et al., 2011). ETM+ reflectance values calculated by this method will henceforth be referred to as Landsat6S.

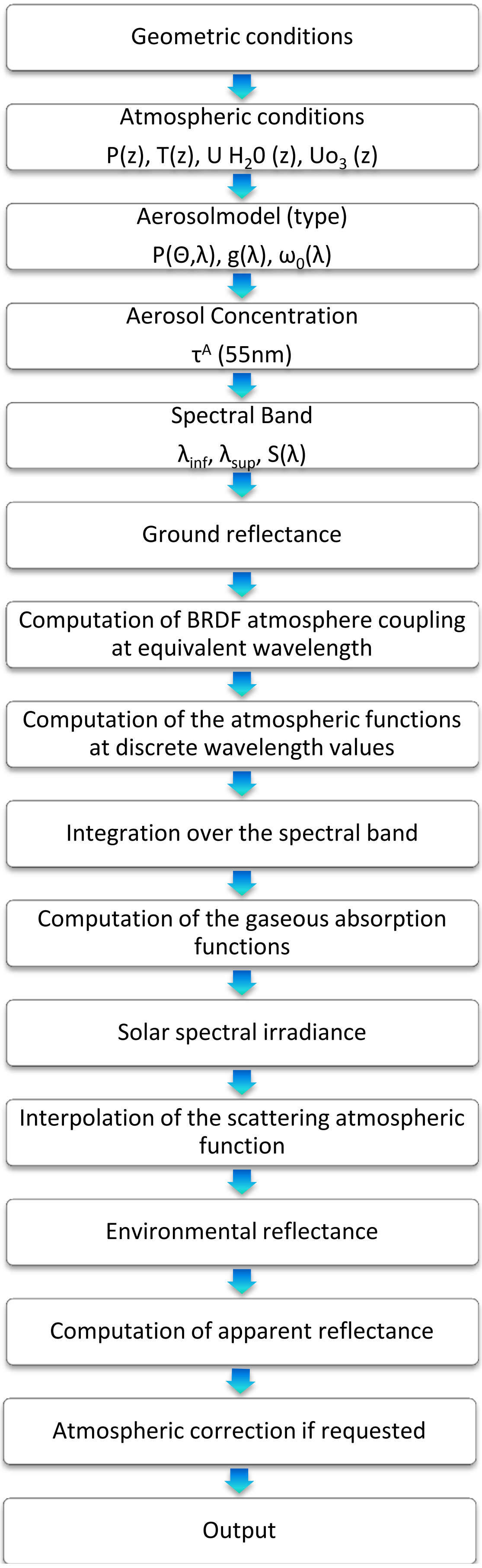

Figure 3.3: General flow chart of 6S computations.

3.2.1.5 Generating surface reflectance from FLAASH

Having carried out atmospheric corrections on the ATM data, FLAASH was also used on the ETM+ image. In contrast to the images generated from dark pixel correction or 6S modelling, FLAASH modelling allows the ETM+ image and the ATM swaths to be directly compared as they underwent the same correction process. In order to accomplish this, the ETM+ image was first converted to at-sensor spectral radiance (see 3.2.1.3.1) before undergoing atmospheric correction using FLAASH as described in Section 3.1.3 to generate surface reflectance. ETM+ reflectance values calculated by this method will henceforth be referred to as LandsatFlaash.

3.2.1.6 NTB conversion

Having carried out the different atmospheric correction methods, the narrowband albedos generated were converted to broadband albedo using the Knap et al. (1999) empirical correction. In the case of the ETM+ band-2 and band-4 were used as they are comparable to the same bands on the TM instrument. For example, differences between *in situ* and ETM+ derived broadband albedos measured on the Haut and Bas Glacier d'Arolla ranged from 0.010 and 0.016 (Pope, 2012).

3.2.2 MODIS

3.2.2.1 Product selection

The moderate-resolution imaging spectroradiometer (MODIS) has been carried on board the Terra satellite since 1999 and on board Aqua since 2002. Terra and Aqua orbit at 705km on a sun-synchronous near polar orbit whilst the MODIS instrument makes observations over a $\pm 55^0$ field-of-view range relative to the instrument nadir in the cross-track direction (Xiong and Barnes, 2006). The instruments capture data in 36 spectral bands ranging in wavelength from 410nm to 14390nm at three different spatial resolutions (250m, 500m and 1km) and have a scene swath of 2330km (Quincey and Luckman, 2009). Together the two instruments image the entire Earth every 1 to 2 days. Out of the numerous data products generated from MODIS data only one was selected to study the surface reflectance characteristics of Langjökull, the MODIS BRDF/Albedo product (MCD43).

The MCD43 product is derived from the surface reflectance product which is generated from MODIS instruments on both the Terra (MOD09 product) and the Aqua (MYD09 product) satellites. These provide surface reflectance measurements across seven spectral bands, the details of which are in Table 3.4.

Band number	**Wavelength interval (nm)**	**Resolution (m)**
1	620-670	250
2	841-876	250
3	459-479	500
4	545-565	500
5	1230-1250	500
6	1628-1652	500
7	2105-2155	500

Table 3.4: MODIS MOD09 and MYD09 band information.

These surface reflectance products are defined as the reflectance that would be measured at the land surface if there were no atmosphere (Vermote et al., 2002). Using MODIS L1B as the primary input, corrections are made for the effects of molecular absorption and scattering, in addition to coupling between atmospheric and surface BRDF and adjacency effects (the atmospheric point spread function). The correction algorithm is based on the MODTRAN atmospheric correction model (Liang et al., 1999) and can be approximated assuming a Lambertian and uniform target by:-

$$\rho_{TOA} = T_g(O_3, O_2, CO_2)[\rho_R + (\rho_{R+A} - \rho_R)Tg\left(\frac{U_{H_2O}}{2}\right) + T_{R+A}\frac{\rho_s}{1-\rho_s S_{R+A}}Tg\left(U_{H_2O}\right)] \quad (3.12)$$

where ρ_{TOA} is the reflectance observed at the top of the atmosphere, Tg refers to gaseous transmission, ρ_R is the molecular scattering intrinsic reflectance, ρ_{R+A} is the intrinsic reflectance of the molecules and aerosols, T_{R+A} is the transmission of the molecules and aerosols and S_{R+A} is the spherical albedo. In addition, it accounts for the coupling between water vapour absorption and aerosol scattering in a simplified way ($U_{H_2O}/2$), which is of sufficient accuracy for MODIS where the absorption by water vapour in the visible and near-infrared bands is weak (Vermote et al., 2002).

The MCD43 product is produced every 8 days using 16 days of acquired MOD09 and MYD09 images. Generating the BRDF/Albedo product is achieved using an algorithm of three basic steps (Lucht et al., 2000; Schaaf et al., 2002). Firstly, atmospheric corrections are carried out which convert TOA radiance to surface directional radiance. Second, narrowband albedos are generated for each band using a kernel-driven, linear BRDF model which relies on the weighted sum of an isotropic parameter and two functions (or kernels) of viewing and illumination geometry to determine reflectance, R (Roujean et al., 1992; Liang et al., 2005):-

$$R(\theta, v, \phi, \lambda) = f_{iso}(\lambda) + f_{vol}(\lambda)K_{vol}(\theta, v, \phi, \lambda) + f_{geo}(\lambda)K_{geo}(\theta, v, \phi, \lambda) \qquad (3.13)$$

where θ, v, and ϕ are the solar zenith, view zenith and relative azimuth angles; $K_k(\theta, v, \phi, \lambda)$ are the model kernels; and $f_k(\lambda)$ are the spectrally dependent BRDF kernel weights or parameters. The kernel weights selected are those that best fit the available observational data (Schaaf et al., 2002). Of the two kernels, $K_{vol}(\theta, v, \phi, \lambda)$ is derived from volume scattering radiative transfer models (Ross, 1981), whilst $K_{geo}(\theta, v, \phi, \lambda)$ is based on surface scattering and geometric shadow casting theory (Li and Strahler, 1992). This algorithm is applied to all cloud-free, atmospherically corrected surface reflectances that have been collected over the 16 day period; the kernel weight most appropriate to the majority situation of whether the surface represents a snow-covered or snow free situation and thus the impact of surface anisotropy (Strahler et al., 1996; Privette et al., 1997; Knap and Reijmer 1998; Lucht et al., 2000; Schaaf et al., 2002).

The suitability of this BRDF/Albedo algorithm for use in surface reflectance studies is widely accepted as a consequence of evaluation by a number of different studies using ground based measurements. Using broadband pyranometers in different uniform areas in Colorado and Montana, Salomon et al. (2006) showed the MODIS albedo product met the absolute accuracy requirement of 0.02 for eight different field sites during spring and summer months. The product was shown to have an RMSE of 0.013 and a bias of around -0.02 although the accuracy dropped during the autumn and winter months at some sites as the heterogeneity of the validation sites increased (Jin et al., 2003). Stroeve et al. (2005) also showed the high quality of albedo retrieval over homogeneous snow surfaces, the mean difference between the MODIS algorithm retrievals and the in situ data being less than 0.02 for all sites in the study and an RMSE of -0.07. It is therefore appropriate to attempt to compare the data produced across Langjökull with the ATM derived data especially with improving cloud detection within the processing stream thus increasing the quality threshold (Stroeve et al., 2005).

The MCD43 product contains two separate sets of measurements, ‘White sky’ and ‘Black sky’. White-sky albedo, i.e. completely diffuse bihemispherical albedo, is derived through integration of the

BRDF for the entire solar and viewing hemisphere. Meanwhile Black-sky albedo, i.e the direct beam directional hemispherical albedo, is calculated through integration of the BRDF for a particular illumination geometry (Schaaf et al., 2002). For this study, the 'Black-sky' albedo has been selected as this is comparable to the data produced from the other instruments used in this study onboard the ATM and Landsat ETM+ (Schaepman-Strub et al., 2006). The final stage of this process is the conversion for the modelled narrowband reflectance to broadband albedo as described in the following section.

3.2.2.2 Broadband albedo generation

Unlike the other sensors used in this study which could be compared on a band by band basis due to their spectral similarity this is not the case for MODIS. The MODIS bands do not have the same spectral response as those of either the ATM or the ETM+ and therefore the generation of a broadband albedo is of particular importance. Attempts to carry out NTB conversion on MODIS data have resulted in both generalised and specialised coefficients for this purpose depending on the surface type under investigation (Liang et al., 1999, 2000; Lucht et al 2000). In particular a set of coefficients has been derived for high albedo snow (Stroeve et al., 2005) and it is this formula deriving shortwave broadband albedo that will be used in this study. Only the shortwave albedo (spectral wavelengths from 300 to 3000nm) are considered due to their dominance of the solar spectrum. The conversion formula for the shortwave broadband albedo of snow ($\alpha_{shortsnow}$) is given by Eq. 3.14:

$$\alpha_{shortsnow} = -0.0093 + 0.1574n_1 + 0.2789n_2 + 0.3829n_3 + 0.1131n_5 + 0.0694n_7 \quad (3.14)$$

where *n* is the MODIS narrowband albedo for the specified MODIS spectral channel.

4. Results

This section is divided into three parts. First, the overall albedo characteristics derived using different atmospheric correction methods on the individual instruments are compared. Second, the precise values of the different datasets are compared using a number of transects. Last, the impacts of varying spatial scales and resolutions on derived albedo will be analysed.

4.1 General patterns of albedo derived from different platforms

4.1.1 Surface albedo of Langjökull derived from ATM measurements

Figure 4.1 shows the surface albedo of Langjökull derived from the ATM swath measurements clipped to ice cap margin.

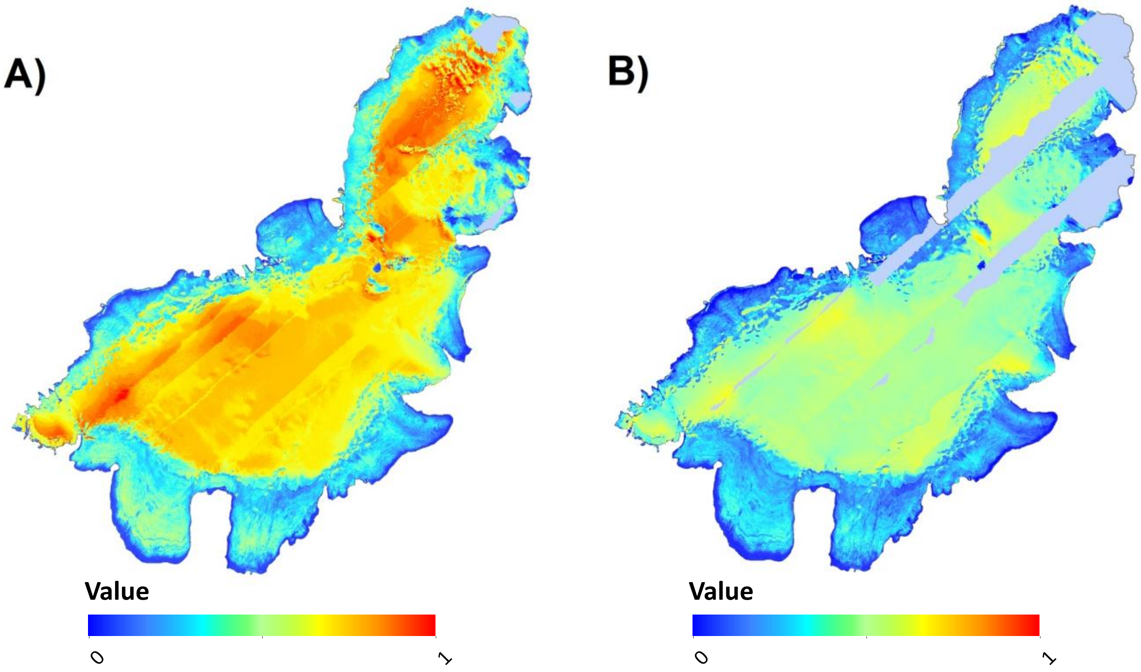

Figure 4.1: ATM surface albedo on 2 August 2007 derived using A) a solar spectrum from Langjökull; B) after carrying out atmospheric corrections using FLAASH.

As shown in Figure 4.1, the glacier surface on 2 August 2007 was characterised by low albedo ice with varying debris content at lower elevations and higher albedo snow at high elevations. The transition between these two zones occurred at elevations between 900m a.s.l. and 1100m a.s.l. The association of increasing albedo with elevation is further supported by comparison with the ASTER GDEM of Langjökull which shows the ATMSolar and ATMFlaash data have positive correlations with height of 0.759 and 0.638 respectively. Both datasets also include a degree of stripping. This is a consequence of the different flight directions of the Dornier aircraft when generating the swaths. Clearer in the ATMSolar dataset, this problematic feature is the result of a non-Lambertian scattering surface and is responsible for the small number of points which have an albedo exceeding 1 (Figure 4.2). To reduce its impact on the derived results, an attempt will be made to limit sampling of albedo values to swaths which have been collected by the aircraft flying in a similar direction. The stripping is less visible in the ATMFlaash dataset and therefore has less of an impact on sampling. The reason for these features will be fully illuminated in the discussion.

Whilst the general trends exhibited by the ATM albedo datasets are clearly similar, it is obvious that their values are significantly different. Both datasets contain pixel values equal to 0 and 1. However, the ATMSolar dataset has a much higher mean value (0.563) compared to the ATMFlaash dataset (0.391). Although this disparity might appear to be the result of the different coverage of the datasets, removing areas in the ATMSolar albedo map not covered by the ATMFlaash data actually raises the mean ATMSolar value by 0.005. The dataset variability reflects the different mean albedo values. The ATMFlaash albedo data has a lower variability, its standard deviation is only 0.159 compared to 0.234 for the ATMSolar dataset. This contrast in variability is graphically represented by the histograms in Figure 4.2. Moreover, the histograms also show that the frequency distribution of albedo values varies smoothly in the ATMFlaash albedo data. In comparison the ATMSolar dataset varies abruptly and has a much greater frequency range. The histograms also show that the datasets are both negatively skewed; the mean value being less than the modal value for each dataset.

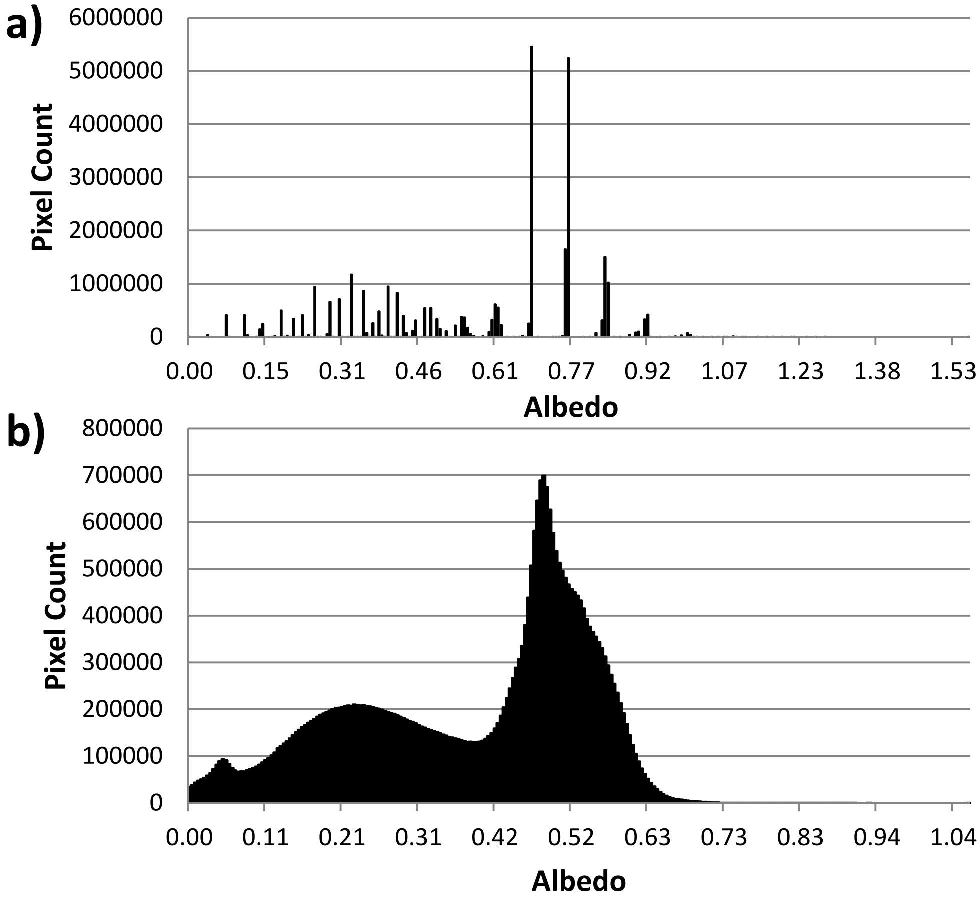

Figure 4.2: Histograms of albedo frequency distribution for a) the ATMSolar dataset, and b) the ATMFlaash dataset.

4.1.2 Surface albedo of Langjökull derived from satellite data

Figure 4.3 displays the surface albedo derived from the three different methods of atmospheric correction used on the Landsat ETM+ image for the 15 August 2007. In addition, it also displays the MCD43 albedo/BRDF product obtained from MODIS.

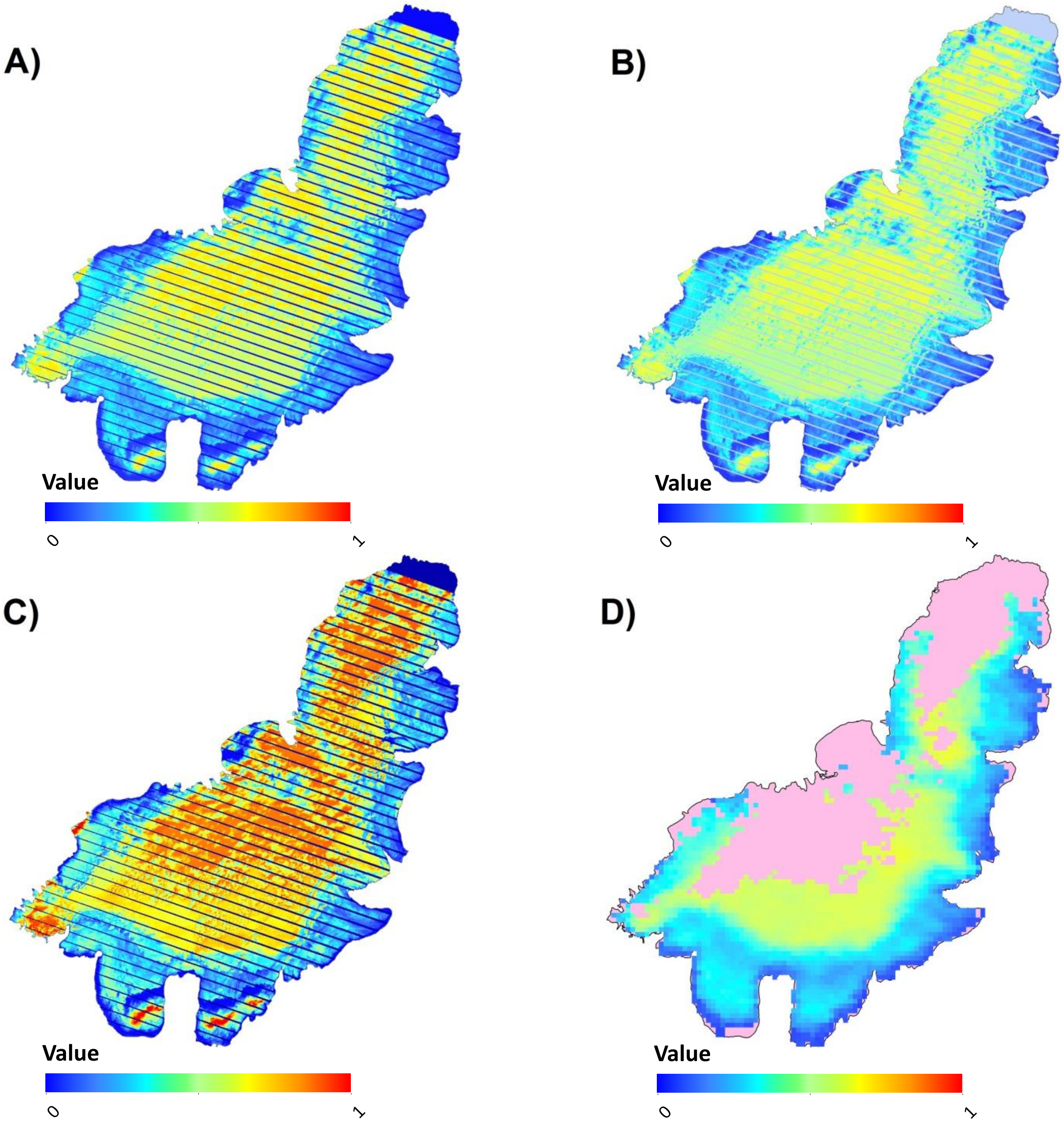

Figure 4.3: A) ETM+ surface albedo derived after using dark pixel atmospheric correction. B) ETM+ surface albedo derived after carrying out atmospheric correction using 6S. C) ETM+ surface albedo derived after carrying out atmospheric corrections using FLAASH. D) MCD43 MODIS product albedo map.

The ETM+ and MODIS albedo measurements show increasing albedo with elevation. The ETM+ images also show that large areas of the ice cap are covered by cloud. Visible in the northern area of the ice cap, this cloud was subsequently removed using a NDSI threshold value of 0.75. This threshold value was chosen due similar values being used in other studies to designate cloud locations (Shimamuraa et al., 2006). In contrast, areas of cloud were removed automatically in the creation of the MCD43 product. As a result of this automated procedure, only areas where cloudless data were derived over the 16 day data collection period were included in the final product. The result is the no data areas seen in Figure 4.3D. The high percentage of cloud cover in the satellite derived datasets in the northern area of Langjökull has meant that subsequent analysis of albedo using this product has been primarily limited to southern areas and specifically the outlet glaciers Svartárjökull, Flosaskarðsjökull, Lónjökull, Vestari-Hagafellsjökull, Eystri-Hagafellsjökull and Suðurjökull (Figure 2.1c).

Having removed the areas deemed to be clouds, it is clear that the albedo values generated by the FLAASH atmospheric correction model are still significantly higher than those derived by the other methods of atmospheric correction (Figure 4.3). The LandsatFlaash dataset has a mean value of 0.457, 0.1 higher than the next highest mean of 0.368 for the MCD43 dataset. The Landsat6S dataset has the lowest mean value of 0.339. Emulating the ATM results, the dataset with the highest mean also has the highest variability. The LandsatFlaash dataset has a standard deviation of 0.226, compared to 0.173, 0.154 and 0.144 for the LandsatDP, Landsat6S and MCD43 datasets respectively. Despite the differences between the mean albedo values and the variability contrasts between the datasets, the frequency distribution of the datasets varies smoothly (Figure 4.4), similar to that for the ATMFlaash dataset (Figure 4.2b). Furthermore, all of the satellite datasets are negatively skewed.

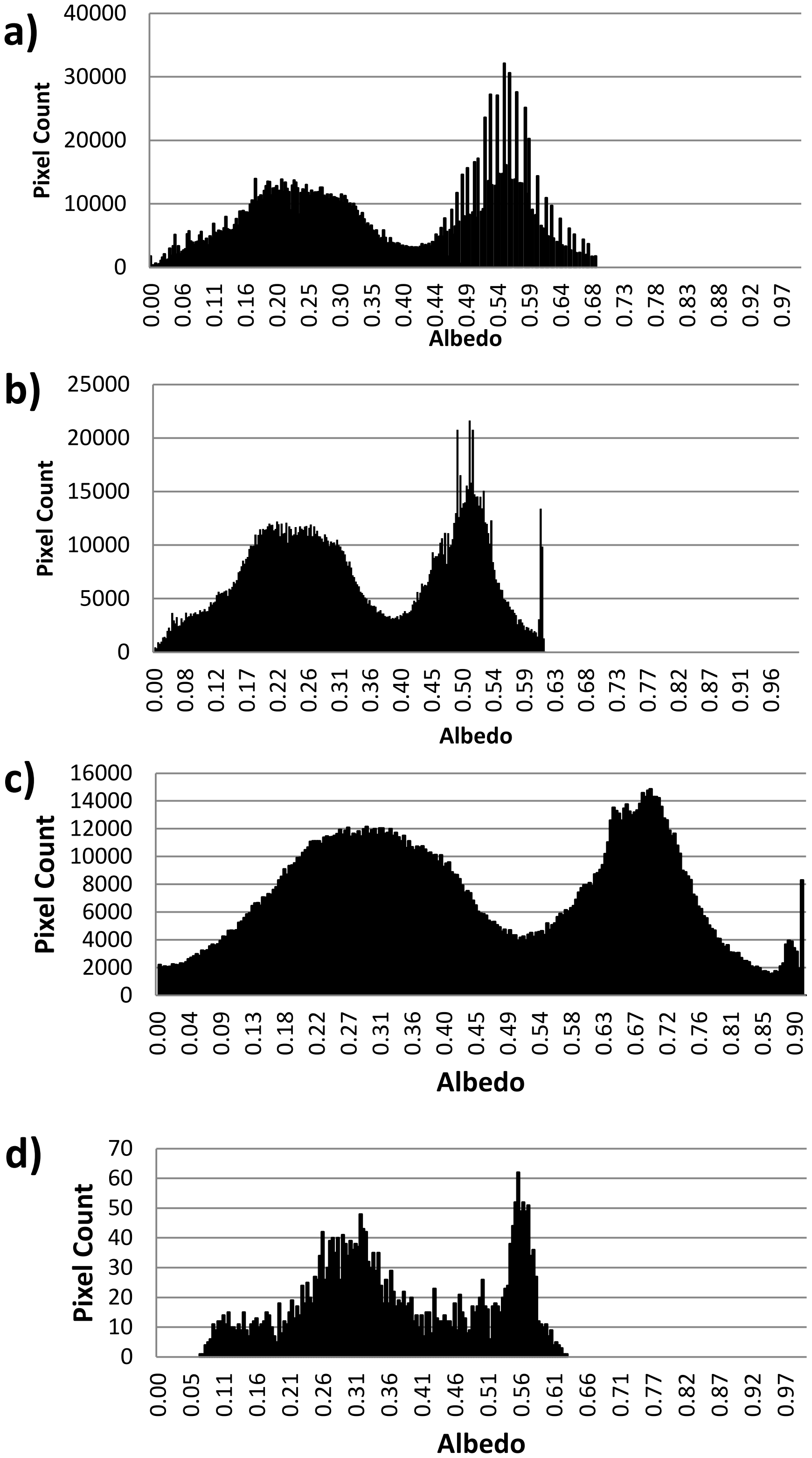

Figure 4.4: Albedo frequency distribution histograms for a) LandsatDP; b) Landsat6S; c) LandsatFlaash; d) MCD43 product.

4.2 Comparison of ATM, ETM+ and MODIS data based on selected transects

In order to begin to quantify the differences between the albedo derived from the different instruments and the various methods of atmospheric correction beyond descriptive statistics, albedo values along a number of transects were extracted. Three transects were placed in relatively homogeneous areas of snow across different ATM swaths (Transects A, B and C). Two were placed in regions of exposed ice across ATM swaths (D and E), whilst one, transect F, ran up a single swath from the glacier margin to an area of homogenous snow cover. These transects can be seen in Figure 4.5.

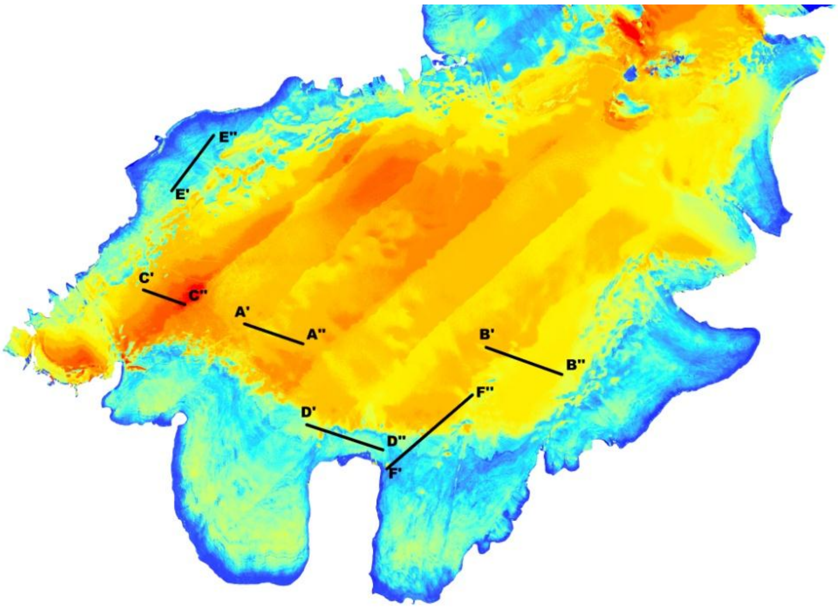

Figure 4.5: Southern area of Langjökull displaying the extraction transects. Surface albedo background is provided by the ATMSolar data.

4.2.1 Comparison of the ATM data along snow transects

The three snow transects were located in areas of progressively higher albedo snow in order to extract the greatest amount of information regarding the different methods of albedo derivation. Transect A had the lowest albedo whilst Transect C had the highest albedo. The ATMFlaash and ATMSolar albedo values along these transects are displayed in Figure 4.5 and show a number of crucial characteristics.

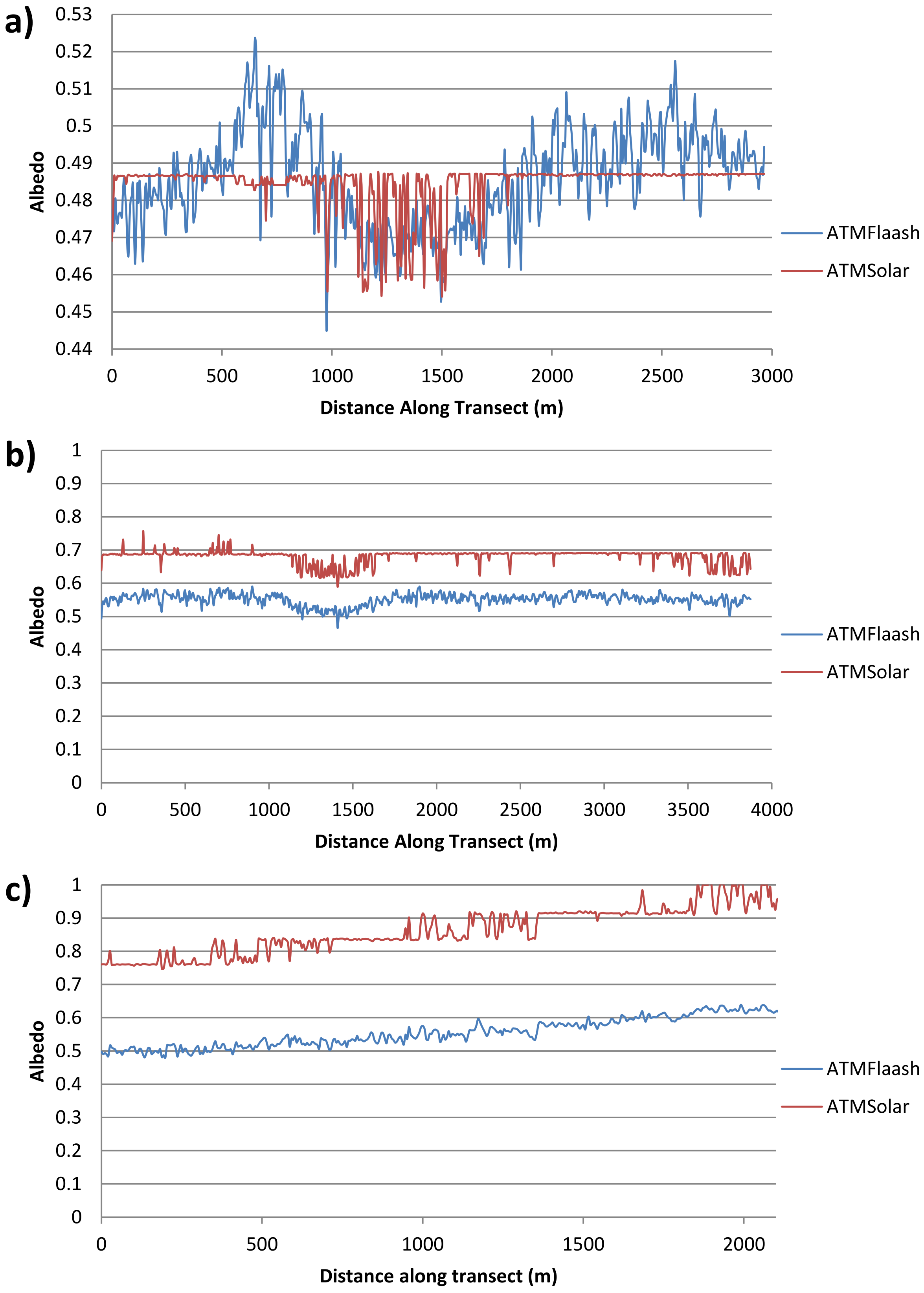

(Figure 4.6: ATM albedo values along a) Transect A’ - A’’; b) Transect B’ - B’’; c) Transect C’ - C’’.

Along Transect A, the ATMFlaash albedo has a high spatial variability, with values ranging by 0.079 between 0.445 and 0.524 (Figure 4.6a). Across the transect, the general albedo pattern is for albedo to increase from the start of the transect before entering a low albedo region and subsequently increase over the rest of the transect. In contrast, the ATMSolar albedo values have an upper limit of 0.487. The albedo value along the ATMSolar transect does not fluctuate, the only exception being the area of low albedo seen in the ATMFlaash data. These characteristics can also be seen along Transect B (Figure 4.6b). The ATMFlaash surface albedo shows a high degree of variability whilst the ATMSolar albedo has an upper limit of 0.7. Furthermore, in regions of low ATMFlaash albedo, the ATMSolar albedo values drop and exhibit the variability characterising the ATMFlaash data. Transect C shows slightly different characteristics. Along this transect, the ATMFlaash albedo increases slowly. This trend in mirrored by the ATMSolar transect but, unlike transects A and B, the albedo values appear to have a stepped upper albedo limit which increases along the transect. The difference in the value between the ATM datasets is at its greatest along Transect C, where albedo is higher than the other transects.

These characteristics suggest that the FLAASH atmospheric correction model is extremely capable in terms of producing surface albedo values for regions of snow. In contrast, the solar spectrum calibration was fundamentally unable to produce a representative set of values. In order to explain the apparent albedo ceiling in the ATMSolar data, the narrowband reflectance values for each band were re-examined. Upon analysing band-3 and band-7, those used in the NTB conversion, the apparent cause of the albedo ceiling was found. The data for band-3 was shown to be highly variable across the high albedo regions of Langjokull whilst band-7 was almost constant throughout these areas. This saturation of band-7 resulted in any broadband albedo variability being entirely the result of band-3 variability. This relationship was reflected across all three transects A, B and C by the ATMSolar data showing near constant values in high albedo areas. In addition, unsaturated nature of band-7 in lower albedo areas allowed the ATMSolar data to show the albedo variability shown in the ATMFlaash dataset.

4.2.2 Comparison of the ETM+ data along snow transects

The characteristics of the ETM+ albedo data are relatively simple over the snow transects in comparison to the ATM data (Figure 4.7). All three transects show the ETM+ albedo values derived by the three different methods to be largely covariant. Despite this, a key difference between the datasets exists. The transects show the albedo values derived from the FLAASH atmospheric model to be too high. This assertion is based on the general agreement between the 6S and dark pixel albedo values which have an absolute difference of only 0.05. Moreover, the 6S atmospheric correction model has regularly been validated for ETM+ images and is therefore likely to be the most reliable of the different atmospheric correction methods (Mahiny and Turner, 2007). Thus, the LandsatFlaash dataset appears to be overestimating the snow albedo by between 0.15 and 0.2.

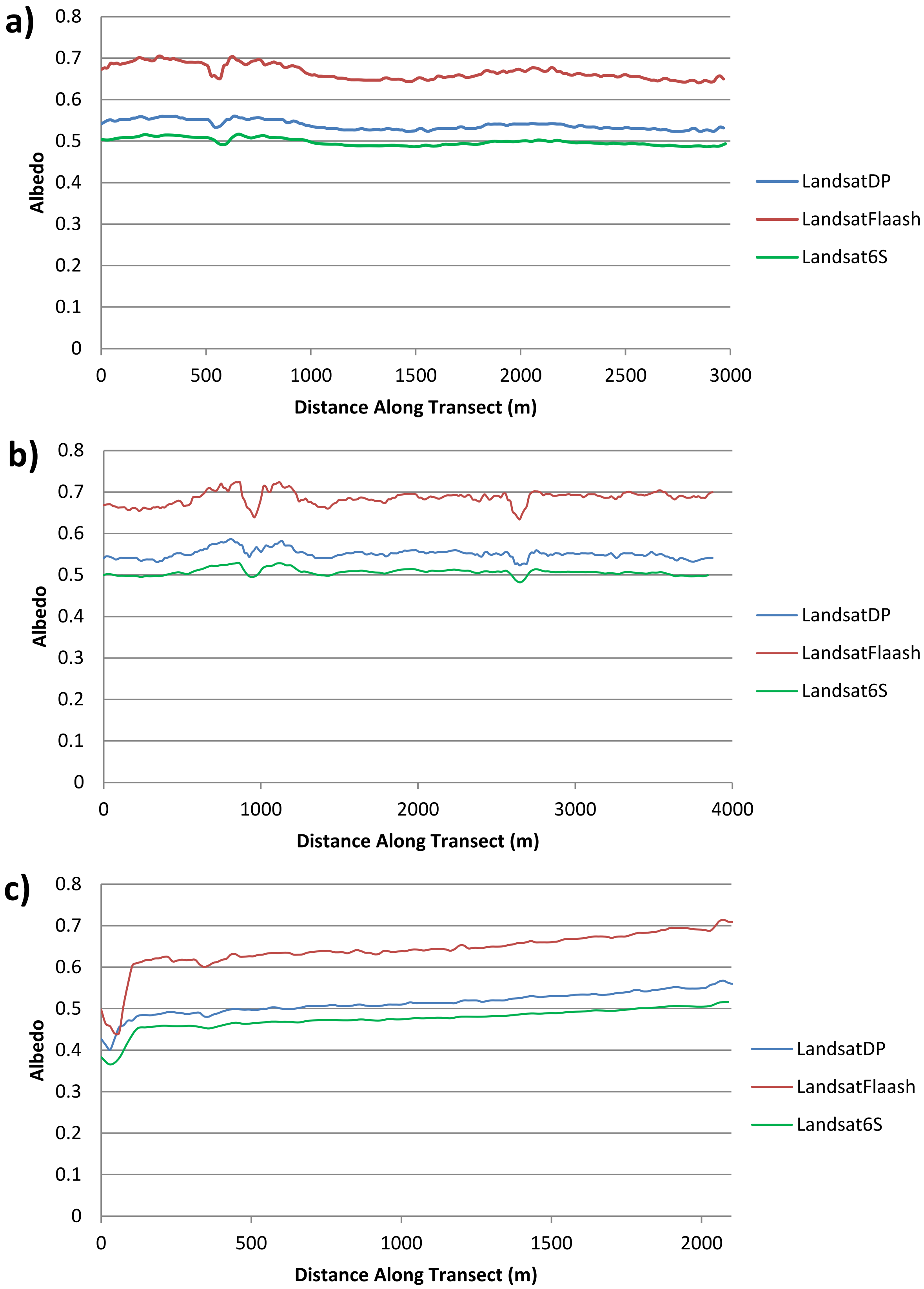

Figure 4.7: ETM+ albedo values along a) Transect A’ - A’’; b) Transect B’ - B’’; c) Transect C’ - C’’.

4.2.3 Comparison of all data along snow transects

In order to compare the albedo values derived from the different instruments along the snow transects, the datasets deemed to be the most representative of the likely surface were selected. Shown in Figure 4.8, the different albedo datasets show values to be in general agreement, any differences being between 0 and 0.1. Despite this agreement, the extracted values clearly demonstrate that the lower resolution satellite-derived products hide the high spatial variability of albedo shown by the ATMFlaash dataset. In particular the MCD43 data shows very little variability along transects A and B and was unfortunately unavailable for Transect C.

Analysis of the datasets for all three transects reveals that the ATMFlaash dataset is not consistently better correlated with any particular satellite albedo dataset. Along Transect A, ATMFlaash values are in close agreement with the Landsat6S values. This is contrasted by transects B and C. In the former ATMFlaash values are closely associated with the values derived by dark pixel atmospheric corrections, whilst in the latter the ATMFlaash values are greater than either of the Landsat datasets. Meanwhile the MCD43 albedo data is far more closely associated with the LandsatDP data. Crucially, no conclusions can be made from these transects alone regarding which method is the most accurate for deriving surface albedo for snow surfaces.

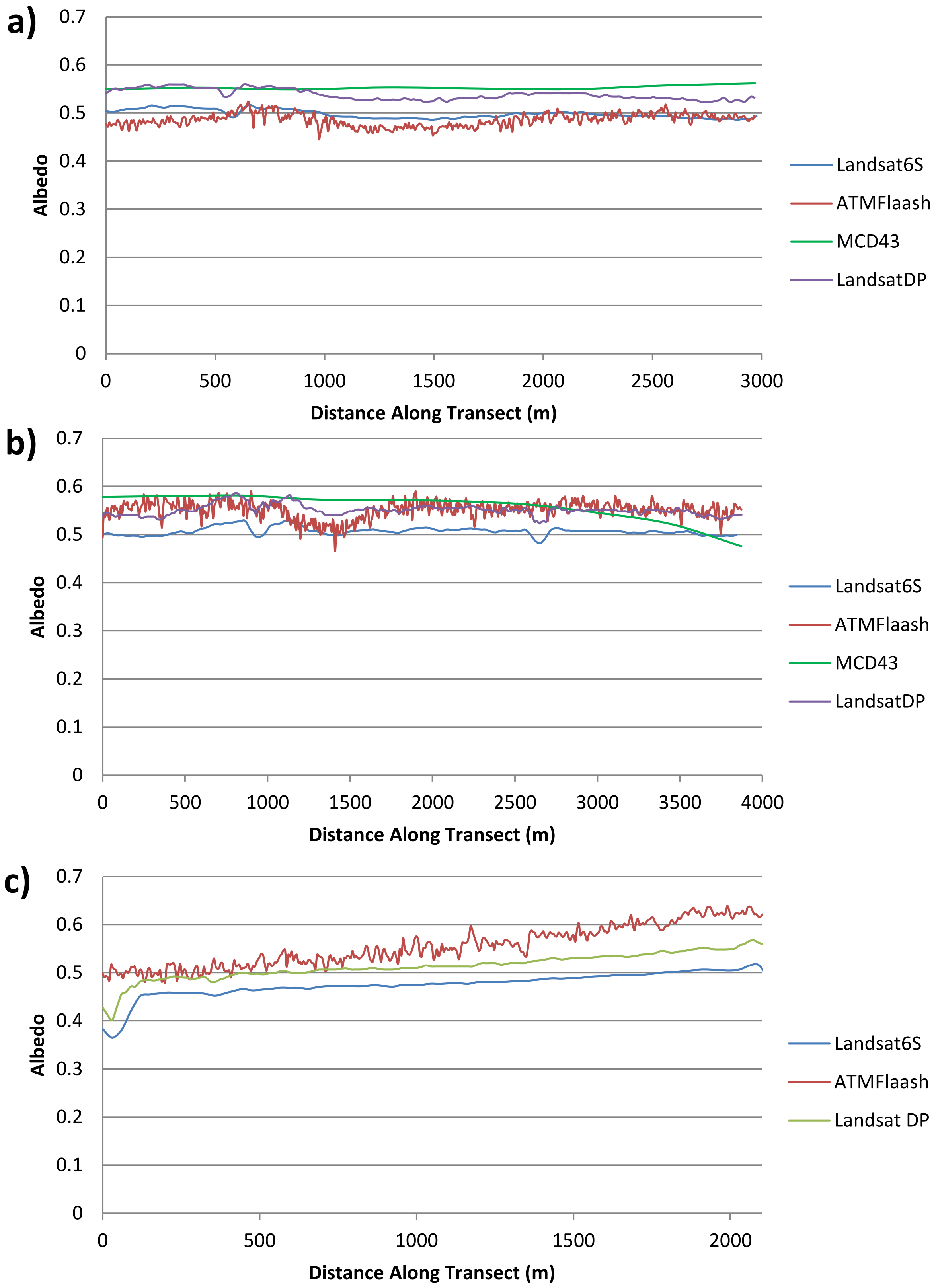

Figure 4.8: Selection dataset albedo values along a) Transect A’ - A’’; b) Transect B’ - B’’; c) Transect C’ - C’’.

4.2.4 Comparison of the ATM data along ice transects

Located in regions of bare ice in two separate drainage basins on Langjökull, Transects D and E show very different characteristics compared to those displayed by the snow transects. Crucially the ATMSolar albedo data no longer displays an upper limit (Figure 4.9). Instead the surface albedo is shown to have the variability seen in the ATMFlaash data. This cements the snow transect analysis as the ATMSolar dataset is able to measure radiance changes over lower albedo snow or ice as band-7 is no longer saturated. As a consequence the ATMSolar data is able to show the surface albedo variability of heterogeneous ice surfaces, but not of snow surfaces.

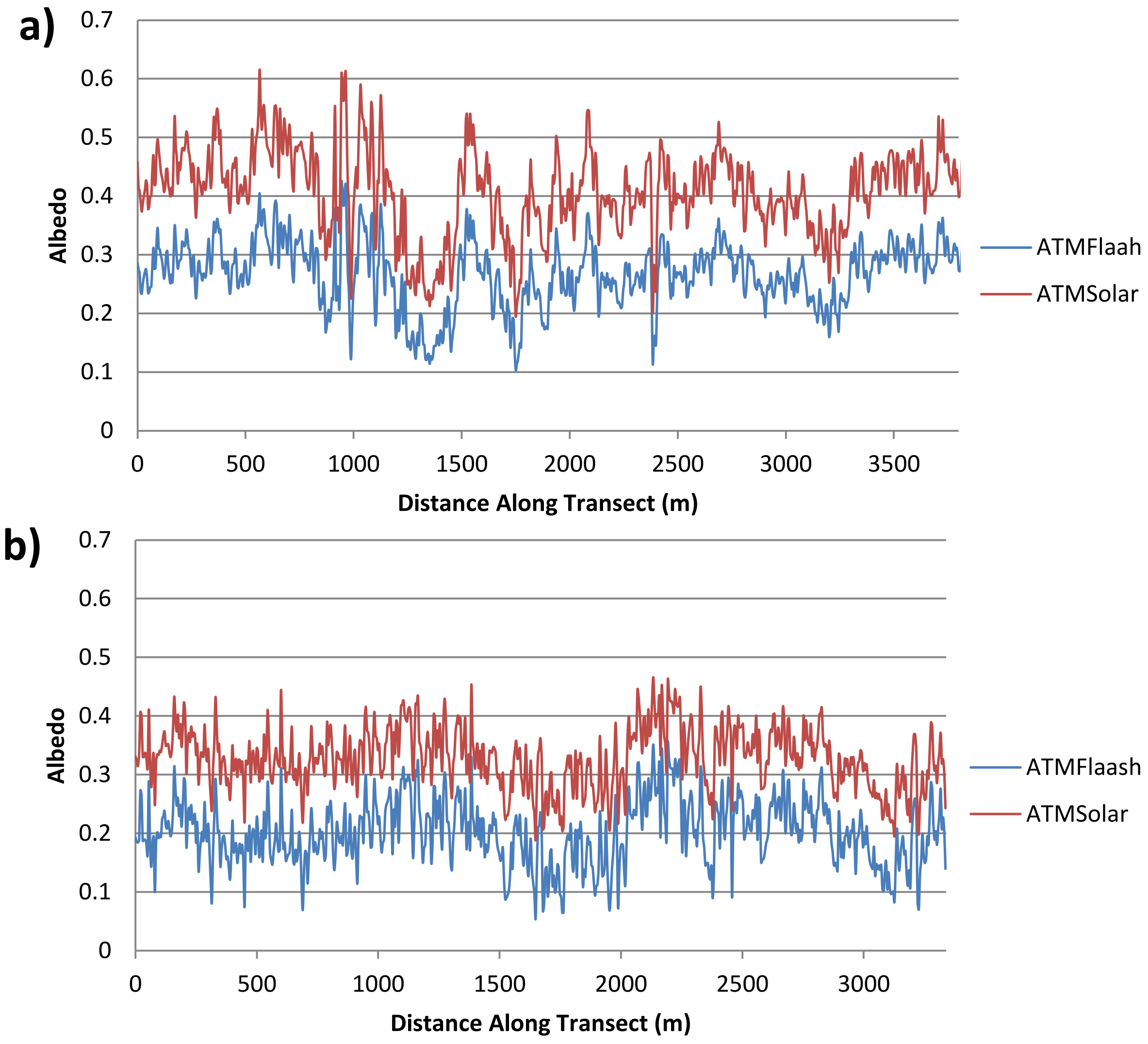

Figure 4.9: ATM albedo values along a) Transect D’ - D’’; b) Transect E’ - E’’.

The two transects also show the ATMSolar albedo values to be greater than those of the ATMFlaash dataset along both transects. They do, however, show a high degree of covariance; the shape of both albedo transects is similar despite the difference between the values not being constant. The rate of change along the ATMSolar transects is greater which is borne out by the value range. Across Transect D, the ATMSolar data has a range of 0.421 compared to 0.320 for the ATMFlaash dataset. Across Transect E, the value ranges are 0.300 and 0.277 respectively.

4.2.5 Comparison of the ETM+ data along ice transects

The ETM+ data show the same characteristics as demonstrated along the snow transects. Over Transect D and E the albedo values derived from dark pixel and 6S atmospheric corrections show even closer agreement than was apparent across the snow transects. Moreover, there is no apparent divergence at either high or low albedo values. Supporting results from the snow transects, the FLAASH atmospheric correction is again seen to overestimate surface albedo; only at extremely low values of between 0.1 and 0.2 are the values comparable to those of LandsatDP and Landsat6S. Elsewhere the LandsatFlaash dataset remains about 0.1 higher than the other two datasets. The conclusion to be drawn, therefore, is that the use of FLAASH to carry out atmospheric corrections over Langjökull for the ETM+ dataset will produced an albedo map which overestimated the true surface albedo. Consequently LandsatFlaash data will not feature in the data analysis beyond section 4.2.

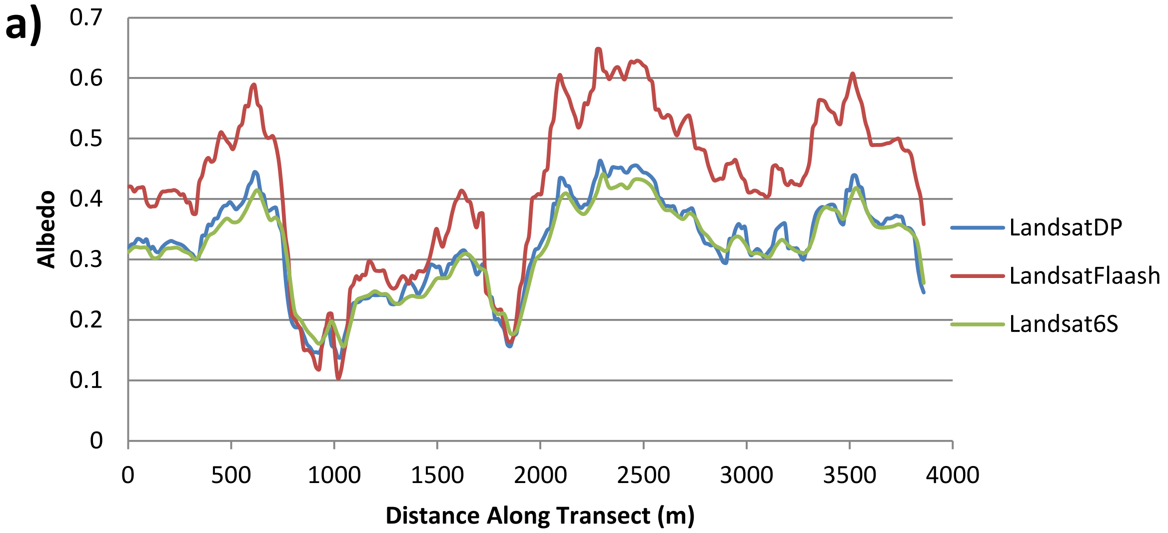

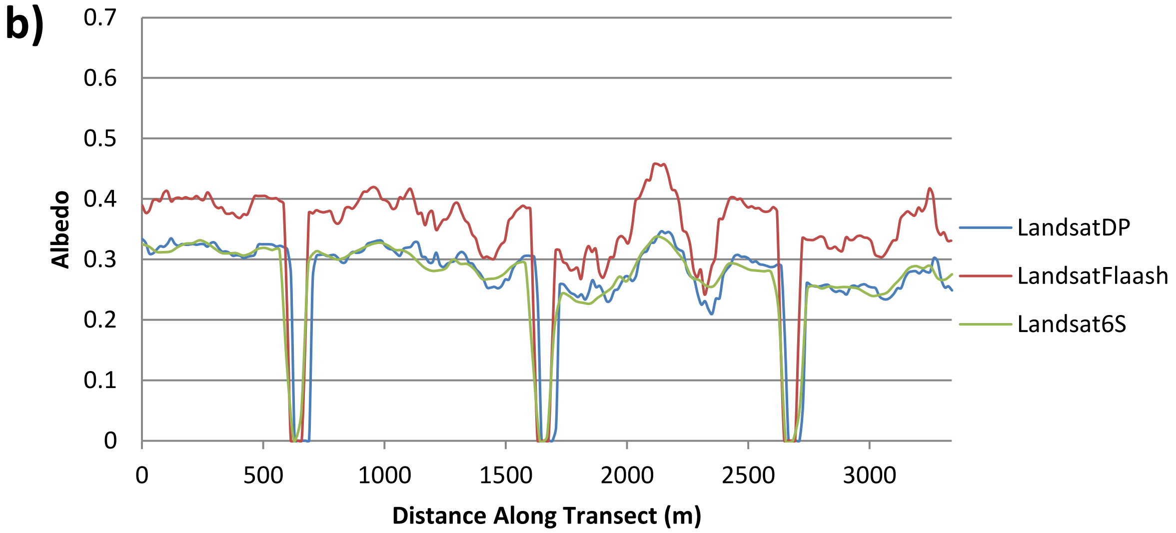

Figure 4.10: ETM+ values along a) Transect D’ - D’’; b) Transect E’ - E’’.

4.2.6 Comparison of all data along ice transects

Given the finding from the analysis of the ATM and ETM+ datasets along the ice transects summarised above, datasets chosen for the inter-instrument comparison were different to those used for the snow transect comparison. The Landsat6S and LandsatDP datasets were deemed comparable and thus only the former is represented, whilst the ATMSolar dataset was included due to the unsaturated nature of band-7 over ice. Transect D and Transect E show greater variability between the ATM and Landsat albedo values than was apparent over the snow transects. Along Transect D the Landsat6S albedo is comparable to the ATMFlaash albedo over the first 2000m. However, for the subsequent 2000m the Landsat6S albedo values occur between the ATMFlaash and ATMSolar albedo values. These observations are reversed along Transect E; the Landsat6S values are comparable to the ATMSolar albedo values over the first 1000m before exhibiting values between those derived from the ATMSolar and ATMFlaash datasets. Importantly, the MCD43 product also shows a similar amount of variability. Along Transect D, the MCD43 product has the lowest average albedo (0.256). However, along Transect E it has the highest average value (0.344). Importantly for this study, the lack of consistent trends between the different instruments may be the first indication of the impact of different spatial resolutions in an area of high albedo variability. Consequently, as the extracted transects provide only a limited means of examining the relationship between albedo variability and spatial resolution, section 4.3 will seek to greater quantify the impacts of varying spatial variability at the pixel, drainage basin and ice cap scales.

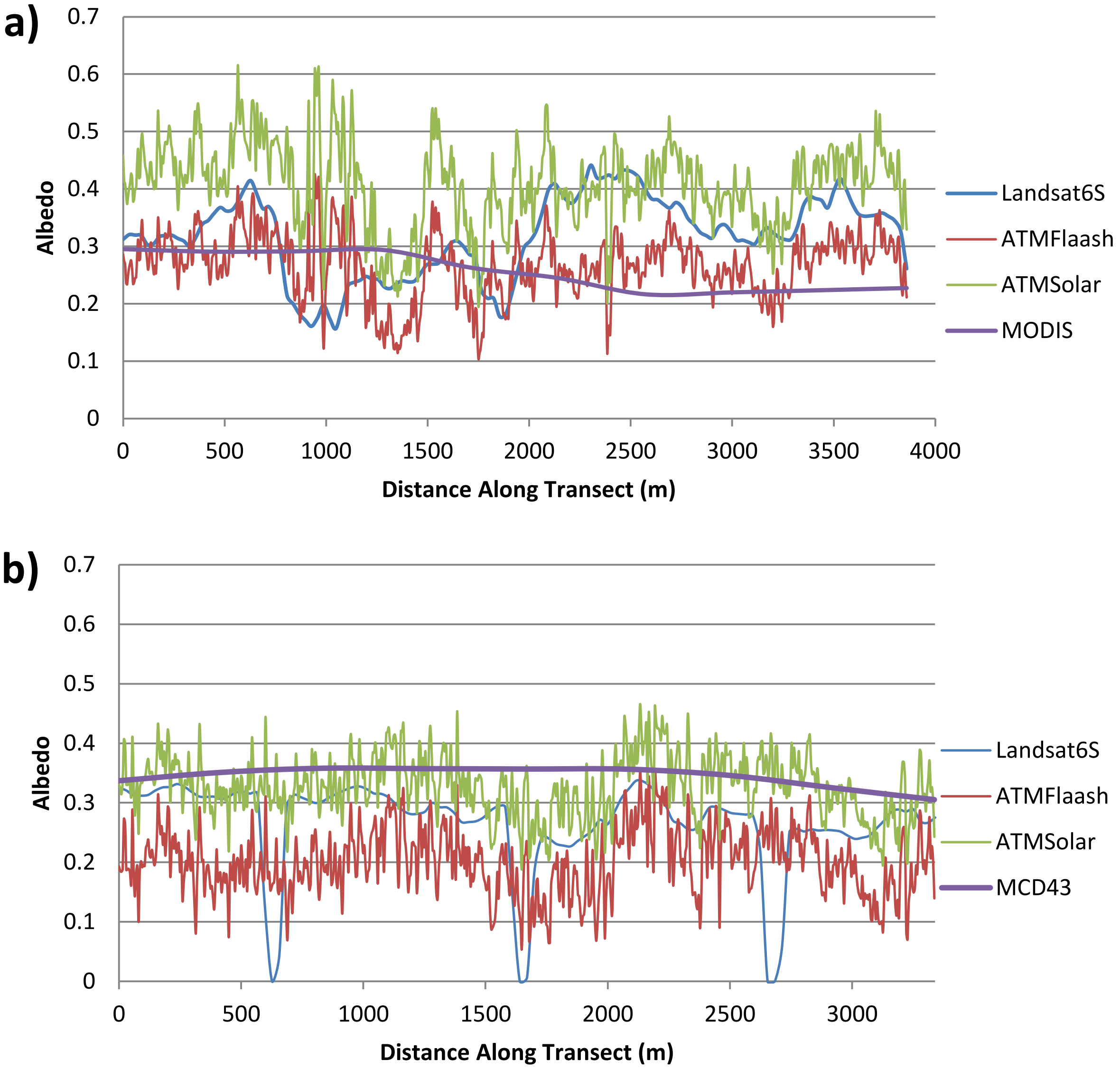

Figure 4.11: Selected dataset albedo values along a) Transect D’ - D’’; b) Transect E’ - E’’.

4.2.7 Up glacier transect

Transect F was located with the intention of investigating whether there were any systematic differences between the different platforms and models of albedo generation moving from the glacier margin, through the ablation zone and into the accumulation area. It should therefore support any conclusions drawn from the single surface type transects summarised above, whilst also allowing any differences across the firn zone to be characterised. The precise placement of the transect at the nadir of the ATM swath, unlike the perpendicular transects, should also reveal any impacts of residual limb brightening not accounted for by the swath corrections. Transect F should therefore reveal any possible artefacts incorporated into the other transects.

Figure 4.12a shows Transect F to be consistent with the ATM albedo characteristics from the other transects. This suggests that conclusions drawn from the analysis of cross swath Transects A to D are unlikely to be affected by the influence of limb brightening. Consistent with previous observations, the ATMSolar albedo values are greater than the corresponding ATMFlaash albedo values with the difference increasing at higher albedos. Perhaps more importantly, the ATMSolar data is again shown to have a maximum albedo value (0.756) in the accumulation area from 3500m onwards. Although the ATMFlaash albedo data also appears to have a similar ceiling at ~0.6, the values are in fact representative of the broadband albedo. The previous relationships between the ETM+ albedo data seen in the cross transect swaths are also shown in Figure 4.12b. The LandsatDP and Landsat6S values strongly agree with each other, whilst the LandsatFlaash data indicates a greater surface albedo; the difference diverging with movement into higher albedo areas.

Despite validating the cross swath transect analysis, comparison of the different instrument measurements along Transect F do begin to reveal differences not previously observed. Over the first 2000m, excluding the first 100m where the ATM records an ice marginal snow patch whilst the SLC failure leads to data loss, there is good agreement between the ATMFlaash, Landsat6S and MCD43 albedo values. This section represents the bare ice in the ablation area and the agreement between instruments is similar to that seen along Transect D and E. However, there is a large difference with movement into the transition zone and the accumulation zone above. The difference peaks at 0.3; the surface albedo derived from the ATMFlaash data greatly exceeds that seen in either the Landsat6S or the MCD43 data in the transition firn zone. Visual inspection of this area reveals a surface characterised by a combination of spatially variable snow and ice facies and it therefore appear to represent a surface of such high spatial heterogeneity that low resolution data has problems accurately representing the area. Consequently, movement out of this area into more homogeneous snow coverage results in the datasets becoming more comparable again. These apparent characteristics are extremely important for point validation and automated albedometer studies of glacier albedo.

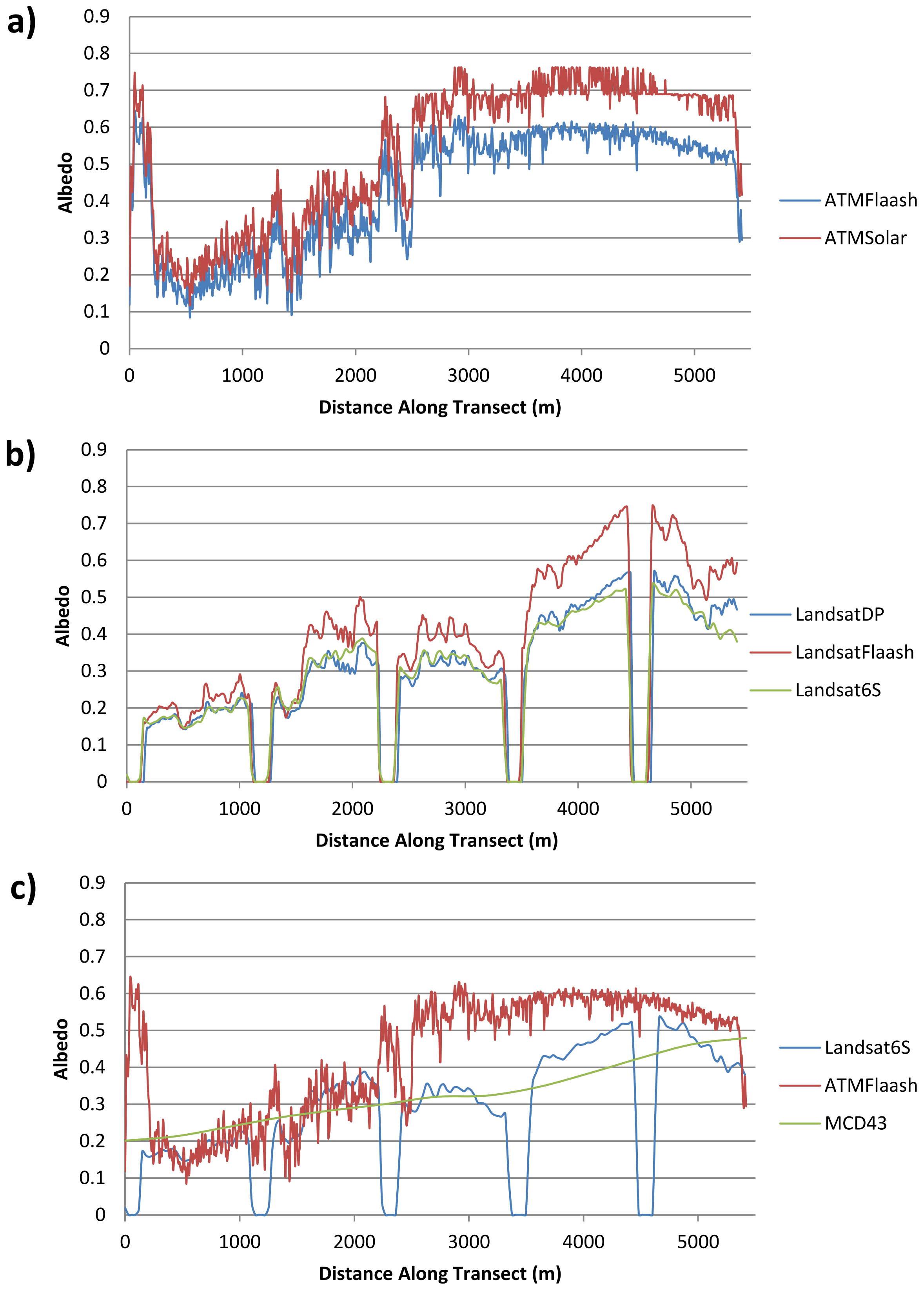

Figure 4.12: a) ATM albedo values along transect F'-F''. b) ETM+ albedo values along transect F'-F''. c) Selected dataset albedo values along transect F'-F''.

4.3 Impact of Spatial resolution

4.3.1 Albedo variability at the pixel level

To assess the impact of image resolution on capturing albedo variability, the different datasets were first analysed at the smallest spatial coverage, that of individual pixels. This was accomplished by taking individual MCD43 pixels and comparing their value to the ATM and ETM+ pixels covered by the same area. Thus each MCD43 pixel value was compared to 8464 ATM pixel values and 232 ETM+ pixel values. To manage the volume of data being analysed a sample of MCD43 pixels was selected. Pixels were selected over a range of albedo values ranging from 0.084 to 0.551, at roughly 0.05 intervals, and in locations where there was complete data coverage to facilitate comparison of the different resolutions at all sites. The location of the pixels selected can be seen in Figure 4.13 whilst the descriptive statistics derived from the individual pixels are displayed in Table 4.1 and shown graphically in Figure 4.14.

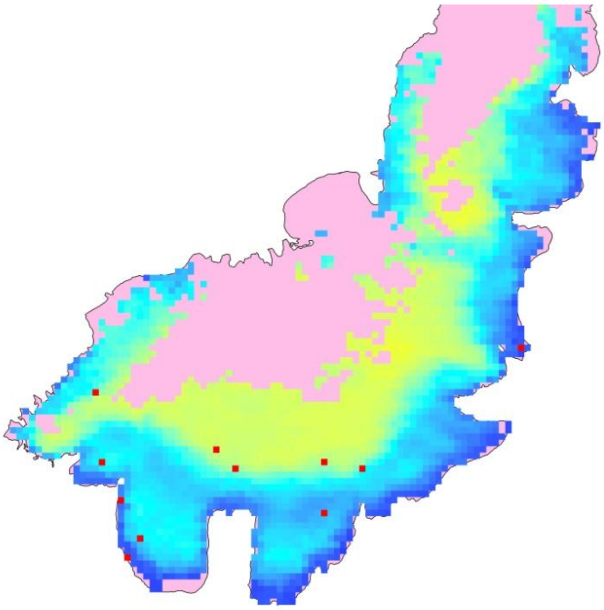

Figure 4.13: Individual MCD43 pixels selected to analyse albedo variability across different spatial scales.

MODIS Pixel Value	**0.084**	**0.105**	**0.164**	**0.233**	**0.301**	**0.341**	**0.370**	**0.434**	**0.467**	**0.502**	**0.551**
ATMFlaash											
Min	0.000	0.010	0.010	0.014	0.050	0.079	0.387	0.064	0.351	0.197	0.410
Max	0.456	0.290	0.325	0.300	0.455	0.395	0.538	0.552	0.545	0.620	0.571
Mean	0.055	0.050	0.075	0.117	0.323	0.262	0.482	0.455	0.478	0.551	0.512
Stdev	0.0332	0.0169	0.0486	0.0381	0.0633	0.0439	0.0177	0.0946	0.0168	0.0376	0.0156
ATMSolar											
Min	0.039	0.039	0.039	0.039	0.112	0.177	0.546	0.229	0.546	0.306	0.610
Max	0.508	0.421	0.474	0.401	0.628	0.568	0.762	0.838	0.762	0.762	0.838
Mean	0.091	0.084	0.137	0.182	0.466	0.407	0.678	0.707	0.700	0.680	0.752
Stdev	0.0548	0.0243	0.0693	0.0463	0.0755	0.0544	0.0246	0.1167	0.0266	0.0400	0.0246
Landsat6S											
Min	0.047	0.051	0.044	0.111	0.184	0.242	0.431	0.187	0.443	0.303	0.499
Max	0.162	0.087	0.150	0.176	0.390	0.339	0.521	0.442	0.495	0.555	0.523
Mean	0.083	0.065	0.069	0.134	0.315	0.292	0.500	0.294	0.482	0.497	0.511
Stdev	0.0204	0.0071	0.0229	0.0123	0.0445	0.0195	0.0153	0.0779	0.0090	0.0589	0.0046
LandsatDP											
Min	0.035	0.039	0.033	0.092	0.176	0.295	0.458	0.180	0.471	0.309	0.541
Max	0.201	0.075	0.165	0.169	0.403	0.446	0.567	0.468	0.534	0.611	0.571
Mean	0.074	0.053	0.059	0.123	0.318	0.378	0.542	0.300	0.518	0.540	0.554
Stdev	0.0236	0.0071	0.0261	0.0130	0.0491	0.0305	0.0190	0.0881	0.0111	0.0691	0.0056
LandsatFlaash											
Min	0.003	0.000	0.010	0.055	0.192	0.245	0.568	0.133	0.574	0.323	0.675
Max	0.200	0.067	0.194	0.197	0.550	0.333	0.745	0.598	0.679	0.785	0.721
Mean	0.060	0.030	0.063	0.119	0.430	0.291	0.708	0.332	0.651	0.675	0.696
Stdev	0.0351	0.0136	0.0390	0.0242	0.0754	0.0182	0.0322	0.1417	0.0188	0.1099	0.0086

Table 4.1: Minimum, maximum, mean and standard deviations of the pixel values for the individual datasets for the 11 sample MCD43 pixels.

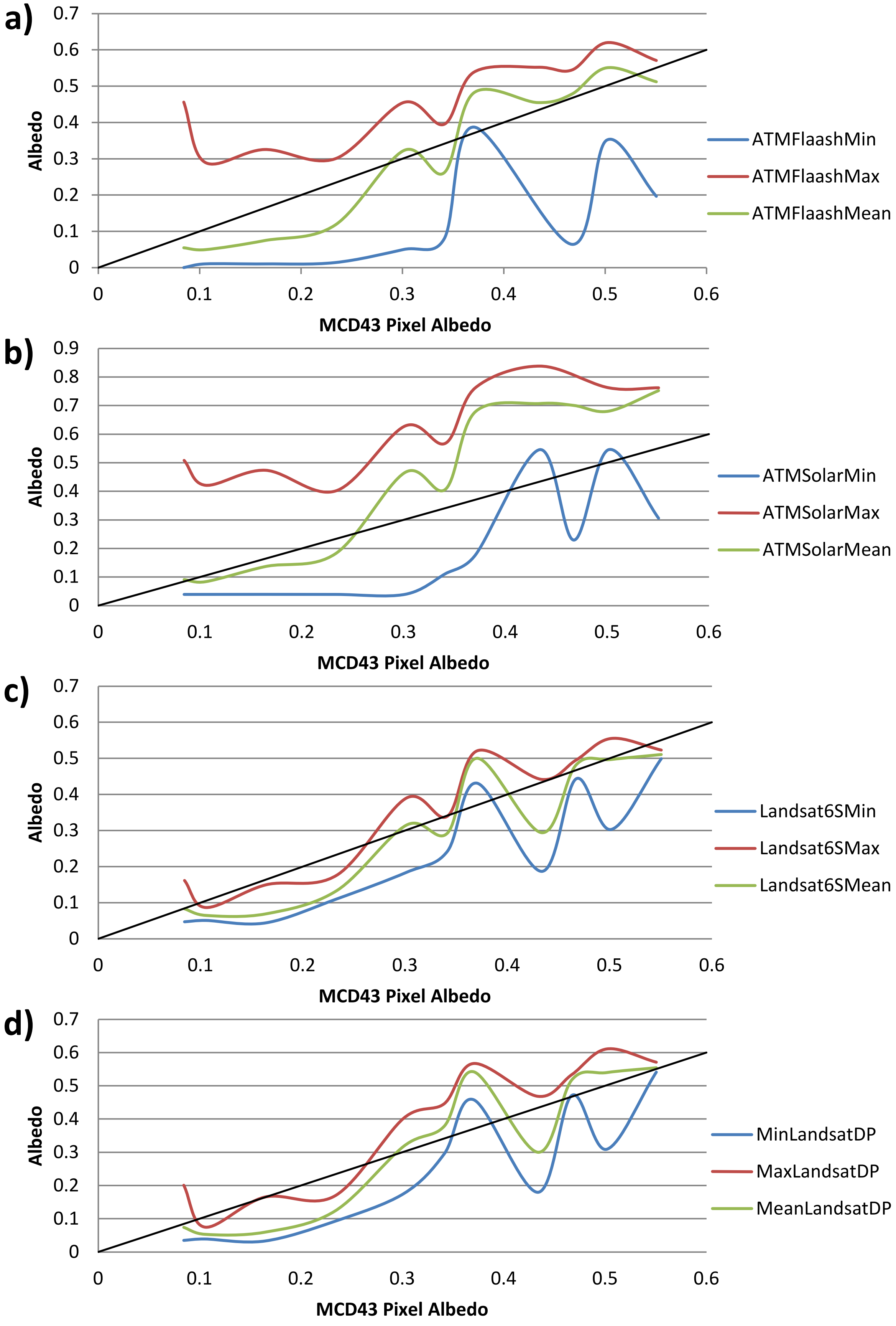

Figure 4.14: Albedo values for the MCD43 pixels for a) ATMFlaash; b) ATMSolar ; c) Landsat6S ; d) LandsatDP.

Both the statistics in Table 4.1 and the graphics in Figure 4.14 show several characteristics of albedo variability at the scale of individual MCD43 pixels. First, the ATMFlaash dataset displays significantly lower values than the ATMSolar dataset which is consistent with the transect observations. However, both demonstrate that within a single MCD43 pixel the albedo within the 0.212km^2 area can vary by as much as 0.45 at scales of 2.5 x 10^{-5} m^2. As a consequence the range of the maximum and minimum albedo values for each MCD43 pixel is between 0.4 and 0.5.

Dataset	**ATMFlaash**	**ATMSolar**	**Landsat6S**	**LandsatDP**	**LandsatFlaash**	**MCD43**
ATMFlaash	1	0.990	0.963	0.948	0.951	0.955
ATMSolar	0.990	1	0.944	0.926	0.926	0.947
Landsat6S	0.963	0.944	1	0.994	0.994	0.921
LandsatDP	0.948	0.926	0.994	1	0.979	0.917
LandsatFlaash	0.951	0.926	0.994	0.979	1	0.891
MCD43	0.955	0.947	0.921	0.917	0.891	1

Table 4.2: Correlation between the datasets over the area of the 11 MCD43 pixels.

Despite the high spatial variability of the ATM albedo values within each MCD43 pixel, the correlation between the ATMFlaash mean albedo and the corresponding MCD43 pixel value is 0.955 as shown in Table 4.2. Meanwhile, the correlation between the MCD43 pixel values and ATMSolar mean values is lower (0.947) as a consequence of a less linear association between the two. Notwithstanding the good correlation between the mean values, it appears that the MCD43 pixels tend to have a bias towards abnormally high or low albedo areas. This is indicated in Figure 4.14a by the MCD43 value overestimating the mean ATM values at lower albedos and underestimating the mean ATM values at higher albedos. Critically these results indicate the high spatial variability of albedo with the MODIS pixels and, by implication, the high variability in the rate of melt for a given solar radiation input. Therefore, the impact of these characteristics will be analysed at the larger spatial scales.

As may be expected from the lower resolution ETM+ albedo data, the range of ETM+ pixel values within each MODIS pixel is much lower than that of the ATM data. The peak range is about 0.3 whilst the average range across the Landsat6S and LandsatDP data is 0.118 and 0.144 respectively. Figure 4.13 shows the Landsat6S dataset to have lower albedo variability in each MCD43 pixel as the trend lines are generally more covariant. However, both the mean difference and the correlation between the MCD43 values and the Landsat6S values indicate that there is greater discrepancy between the MODIS data and the ETM+ data compared to the MODIS and ATM data. The mean values of the ATMFlaash and Landsat6S pixel values are 0.305 and 0.295, which are 94.4% and 91.3% of the mean MCD43 pixel values respectively. Moreover, the correlation between the Landsat6S and MCD43 pixels is 0.921. This is of particular interest as it indicates that the differences between the derived albedos are not solely the consequence of reducing the spatial resolution of the instruments. Meanwhile, the correlation between the mean ATMFlaash pixel values and the corresponding Landsat6S mean values within the 11 MODIS pixels is 0.963. This is the highest correlation value between any two datasets derived from different instruments for the sample pixels and has important possible implications for the wider application of the different instruments. Over the scale represented by individual MODIS pixels it appears that whilst the ETM+ instrument fails to capture the extreme values seen in the ATM data, the mean ETM+ values are closer to the mean ATM values thus implying that the ETM+ instrument can more accurately derive surface albedo compared to MODIS. This conclusion has, however, been made on a limited sample and therefore will be evaluated at the other spatial scales.

In addition to the analysis presented so far, there is a particular feature, visible across the different instrument datasets, which may be crucial to understanding the impact of using comparatively low resolution data to estimate surface albedo. This feature is associated with the MODIS pixel with the value of 0.37. Within this pixel, throughout the other datasets, the albedo range is much lower when compared to the higher and lower albedo MODIS pixels. Furthermore, the minimum pixel value for the ATM and ETM+ datasets exceeds the MCD43 albedo value. Importantly, this is the only MODIS pixel value at which this occurs. The cross dataset occurrence of these characteristics indicates that the cause may relate to the MODIS data itself and therefore to the specific location of the MODIS pixel. The pixel in question was located in the transition zone between the low albedo exposed ice in the ablation area and the higher albedo snow in the accumulation area. This location is crucial as it was in this same zone where Transect F revealed a large disparity between the ATMFlaash and MCD43 data. This contrast meanwhile is not seen between the ATM and ETM+ data. The contrast between the datasets therefore supports the conclusion made in section 4.2.7 that the low resolution MCD43 product may struggle to accurately represent the albedo of this transition zone despite the apparent successful characterisation by the ETM+ product in this case.

4.3.2 Albedo variability at the drainage basin scale

Despite the value of analysing the ability of individual MCD43 pixels to characterise the albedo of Langjökull when measured at higher resolutions, the results of this analysis are inevitably limited by the sample size used, in this case 11 MODIS pixels. Thus, in an attempt to validate the pixel analysis, as well as the earlier transect study, a basin scale investigation was undertaken. For this purpose Svartárjökull, on the south west of the ice cap was chosen to act as a test basin (Figure 2.1c). Svartárjökull was chosen because it encompassed the large variability of surface types seen over the rest of the ice cap and yet its relatively small size made the number of data points manageable. Prior to carrying out the analysis on Svartárjökull two steps were taken. First, the region of cloud visible in the north of the basin in the ETM+ images and not removed by the NDSI threshold were manually removed from the images. Second, the datasets deemed to be most representative of the likely albedo surface were chosen using the outcomes of the transect and pixel investigation. Images from these datasets are seen in Figure 4.15 whilst histograms of the frequency distribution of pixel values are displayed in Figure 4.16.

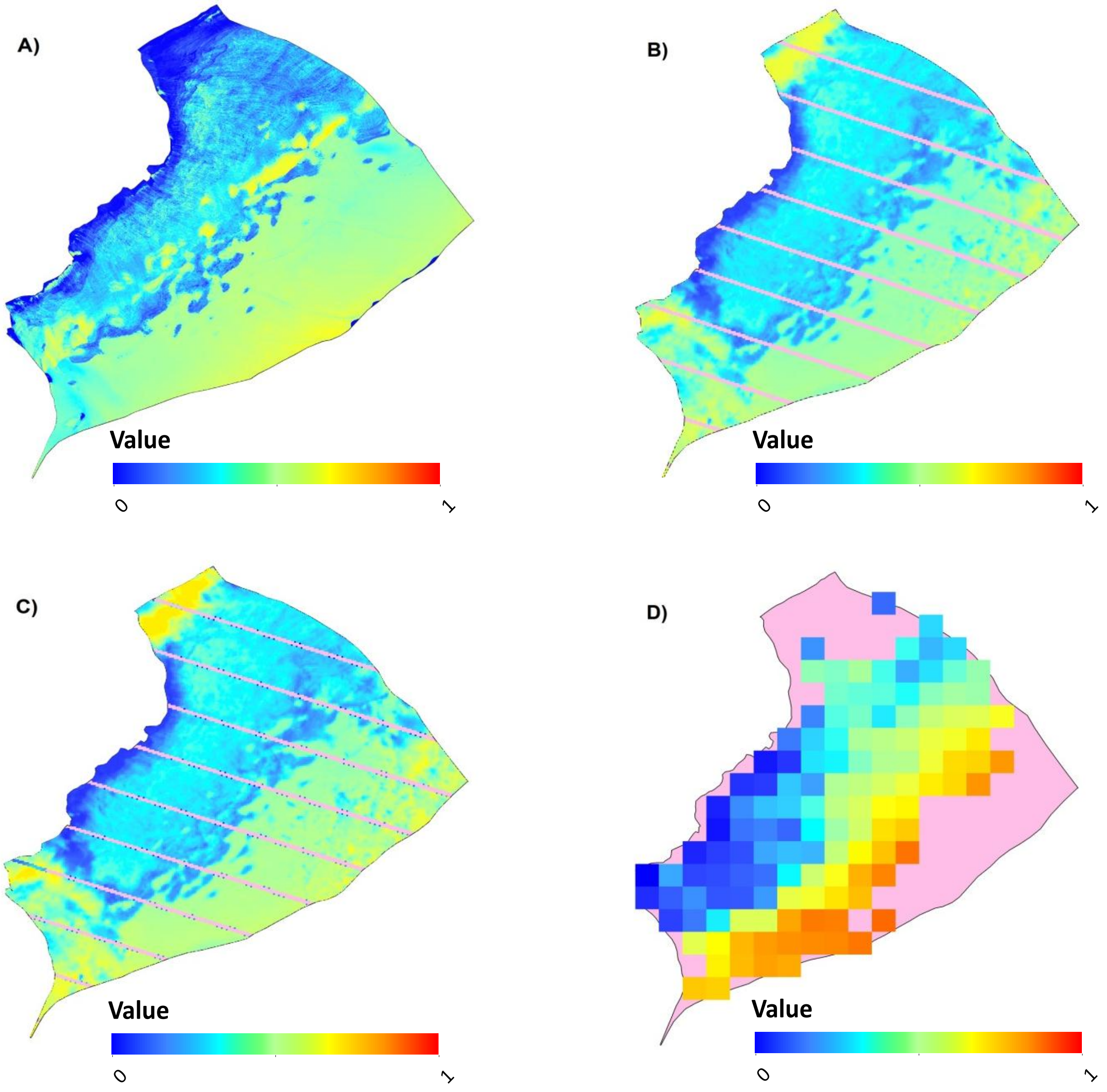

Figure 4.15: Albedo map of Svartárjökull for A) ATMFlaash; B) Landsat6S ; C) LandsatDP ; D) MCD43.

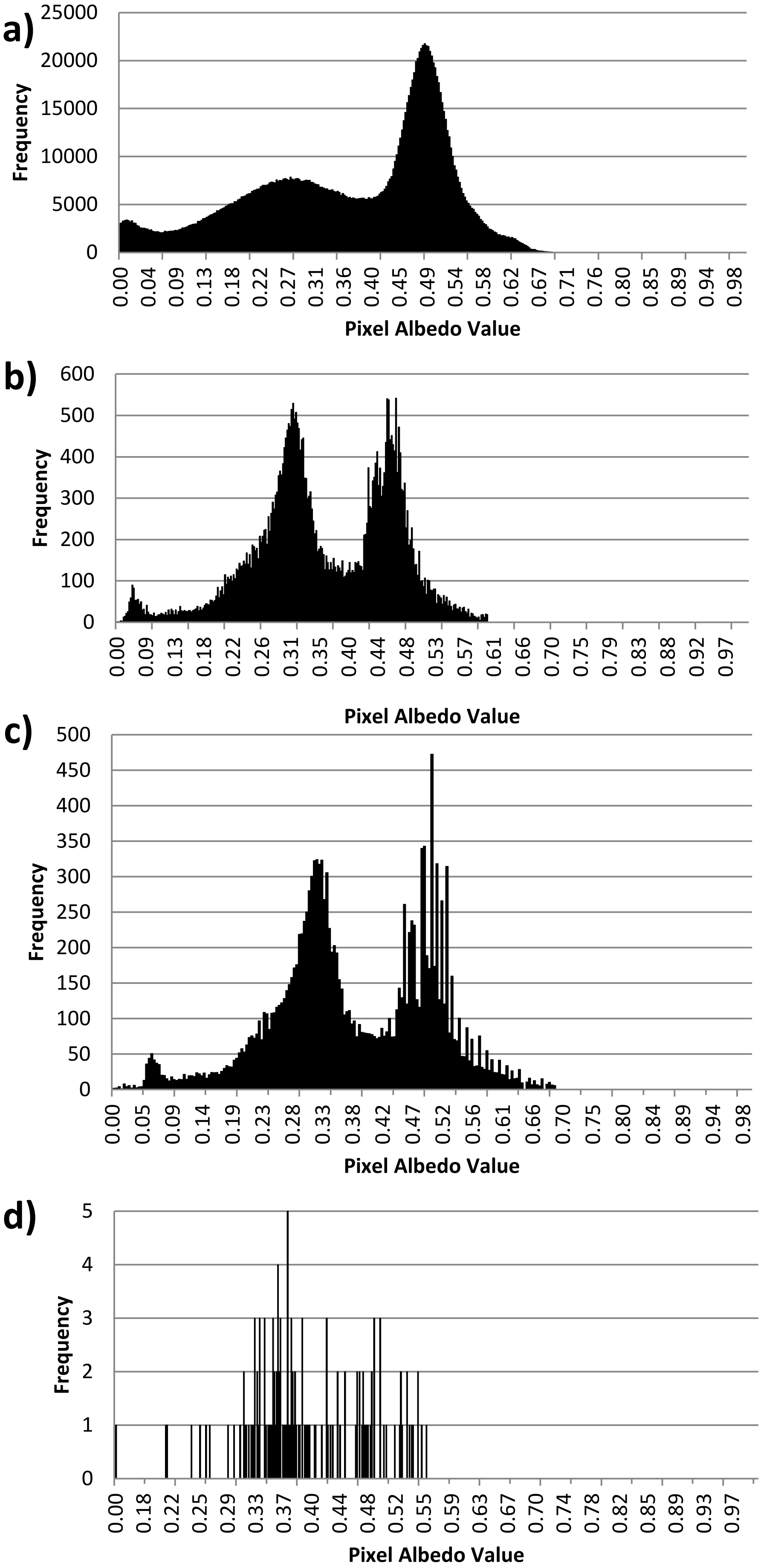

Figure 4.16: Histogram of pixel values for Svartárjökull for a) ATMFlaash; b) Landsat6S; c) LandsatDP; d) MCD43.

Svartárjökull represents a seventeen fold increase in the number of pixels being sampled compared to section 4.3.1. Svartárjökull represents 1.522 x 10^6 ATMFlaash pixels, 4.257 x 10^4 ETM+ pixels and 188 MCD43 pixels. Svartárjökull therefore represents a necessary intermediate step between analysing albedo variability at the pixel level and ice cap wide scale. The albedo value frequency distribution seen across Svartárjökull (Figure 4.16) is similar to that seen across the ice cap as a whole (Figure 4.2). However, the comparatively small size of the ablation area means that the outlet glacier has a higher mean albedo value for all of the satellite derived datasets compared to the overall ice cap.

Comparison of the albedo values across Svartárjökull between the different datasets reveals a number of similar characteristics present in the individual pixel analysis. Across the basin, the MCD43 mean albedo value is the highest (0.399), compared to 0.373, 0.361 and 0.381 for the ATMFlaash, Landsat6S and LandsatDP datasets respectively which is the same order of size as seen across the pixel analysis. In addition, albedo variability implied by the standard deviation of the data has increased as a consequence of the greater range of albedo values incorporated across the drainage basin; the greatest degree of variability still being associated with the highest resolution dataset. Crucially therefore the amount of variability is directly linked to the pixel resolution of different datasets (Table 4.3) and the area size being sampled.

Instrument	**ATMFlaash**	**Landsat6S**	**LandsatDP**	**MODIS**
Min	5.25 x 10^{-6}	0.046	0.001	0.144
Max	0.714	0.609	0.694	0.560
Mean	0.373	0.361	0.381	0.399
Stdev	0.1521	0.1051	0.1282	0.0796

Table 4.3: Minimum, maximum, mean and standard deviation of the different datasets for the Svartárjökull basin.

Despite these similarities between the pixel analysis and the analysis across Svartárjökull between the different resolution datasets, there is a large change in one characteristic with the increase in spatial coverage. The correlation between the different datasets is substantially lower for outlet glacier compared to the original 11 pixels (Table 4.3). Across the original 11 MODIS pixels, the correlation between the MCD43 albedoes and the ATMFlaash means was 0.955; this has dropped to 0.441 across Svartárjökull. Similarly, the correlation between the Landsat6S and the ATMFlaash datasets has dropped from 0.963 to 0.504. Most dramatically the correlation between the MCD43 albedo values and the Landsat6S mean values has dropped from 0.921 to 0.432. The correlation between the LandsatDP dataset and the other datasets has also declined. The change in correlation, whilst maintaining similar differences between mean values is the result of increasing the sample size which incorporated a specific set of surface characteristics.

Dataset	ATMFlaash	Landsat6S	LandsatDP	MCD43
ATMFlaash	1	0.504	0.419	0.441
Landsat6S	0.504	1	0.916	0.432
LandsatDP	0.419	0.916	1	0.401
MCD43	0.441	0.432	0.401	1

Table 4.4: Correlation between the datasets over the Svartárjökull basin.

Visible in Figure 4.15 and to a lesser degree in Figure 4.16, the transition from the 5m pixel resolution of the ATMFlaash data to the 30m resolution of the ETM+ data has resulted in the loss of extremely high and low values. The ETM+ instrument averaging has lowered the high albedo values of the accumulation area and raised the albedo values at the glacier margin. The removal of large albedo ranges by Landsat was earlier evident in section 4.3.1 as shown by the small range for the Landsat6S and LandsatDP and to a lesser extent by the LandsatFlaash dataset. Crucially, it appears that the reduction of albedo values in the accumulation area and increasing of albedo values in the ablation area suggests that the differences between the ETM+ and ATM datasets is not the result of the different times of acquisition. Instead these differences are likely to be caused by the spatial sampling, calibration and processing of the instrument data. The result of this smoothing, is that the melt trend, using this data, between the ablation and accumulation area is also smoothed and thus loses a degree of spatial variability which may be of particular importance to modelling surface mass balance.

Whilst the ETM+ instrument appears to smooth the albedo across the glacier surface, the MCD43 instrument exhibits the opposite characteristic. Figure 4.15d shows the low albedo area seen in the other images along the north western edge of the basin to have been expanded over the basin area. This is opposed by the high albedo area along the southern edge of the basin which far exceeds the albedo measured by the other instruments. However, the opposing misrepresentation has the impact of producing a mean value more representative of the overall surface. As was the case with the ETM+ instrument, this misrepresentation of extreme albedo areas in pixels is consistent with observations made in the pixel analysis. Unfortunately from a melt perspective, the rough pattern of albedo transition therefore implies an extremely uneven pattern of surface melt, greatly enhanced at the margin and greatly repressed at higher elevations.

4.3.3 Albedo variability at the ice cap scale

To validate the conclusions made over the smaller spatial extents, albedo variability across the whole ice cap was analysed. This section analyses the entirety of the ATMFlaash data points available and therefore any characteristics specific only to the limited sample sizes previously used should be exposed. Only the Landsat6S dataset was chosen as part of this analysis due to this dataset and the LandsatDP dataset being deemed comparable as a result of the previous results. In order to carry out ice cap wide analysis, the different datasets were masked against each other in order to make the areas in question directly comparable. As a result, statistics given in section 4.1 will appear slightly different in this section of the analysis.

Across Langjökull the mean albedo characteristics mirror those of Svartárjökull. At the drainage basin scale the MCD43 mean albedo value was the highest whilst the Landsat6S value was the lowest (Table 4.5). Across Langjökull the MCD43 mean albedo value is again the greatest, 0.368, whilst the Landsat6S value remains the lowest 0.355. The ATMFlaash albedo recorded a mean value of 0.360. Despite the difference between these mean values, they are the smallest differences over the three different spatial extents sampled. However, it is still clear that the choice of instrument used to measure albedo has a large bearing on the calculation albedo evolution over the ablation season.

Instrument	**ATMFlaash**	**Landsat6S**	**MODIS**
Min	0.254×10^{-6}	0.012	0.068
Max	0.909	0.625	0.630
Mean	0.360	0.355	0.368
Stdev	0.1501	0.1496	0.1423

Table 4.5: Minimum, maximum, mean and standard deviation of the different datasets for the Langjökull.

The impact of increasing the spatial coverage (sample size) on variability and correlation characteristics was not consistent with the characteristics seen with the increase in coverage from the 11 MODIS pixels to Svartárjökull. In terms of variability, the instruments all showed the variability of albedo to be higher across Langjökull, compared to the smaller spatial coverages. In addition, variability was also linked to instrument resolution as the ATM once again displayed the greatest variability. In contrast the correlation between the datasets increased from the Svartárjökull sample. The ATMFlaash and MCD43 albedo values had a correlation of 0.648, the ATMFlaash and Landsat6S values had a correlation of 0.695, and the MCD43 and Landsat6S values had a correlation of 0.566. The order of the most correlated datasets is, however, maintained. The difference between the dataset correlations and the observation made for the Svartárjökull basin suggest that the outlet glacier itself may not have been representative of the ice cap as a whole. Principally this appears to be the result of the limited size of Svartárjökull, resulting in a greater rate of change of albedo over the glacier surface. This rate of change was uncharacteristic of the southern margin of the ice cap which makes up the majority of the sampled ice cap area. Despite this, the conclusions during the Svartárjökull analysis are critically important to consider when using remotely sensed data. Consequently, the contrasting characteristics of Svartárjökull and Langjokull will be further explored in section 5.

5. Discussion

This discussion is divided into two parts. First, the spatial characteristics of albedo variability between the different platforms will be assessed. Second, it will discuss the problems inherent in the different methods of generating broadband albedo.

5.1 Impact of different spatial resolution data on derived albedo

5.1.1 Spatial characteristics of the differences between the derived albedo datasets

Section 4.1 and 4.2 both showed that there were distinct differences between the albedo values derived across Langjökull for the different datasets. In particular, section 4.2, suggested the differences were specifically related to the spatial resolution of the different datasets as the ATM data clearly showed a greater rate of surface albedo change. This suggestion was supported by section 4.3 which indicated both a bias towards representing certain values within each of the lower resolution datasets, as well as a spatial component to the differences between the albedo values being produced. As a result of the contrasting characteristics seen between Langjökull, Svartárjökull, and the 11 MODIS pixels, and the explanations ventured, the differences between the ATMFlaash, Landsat6S and MCD43 datasets were mapped across Langjökull. This was carried out in order to determine whether there was any overall spatial component to the observed characteristics (Figure 5.1). In each case the lower resolution dataset albedo value was taken away from the albedo value given by the higher resolution dataset.

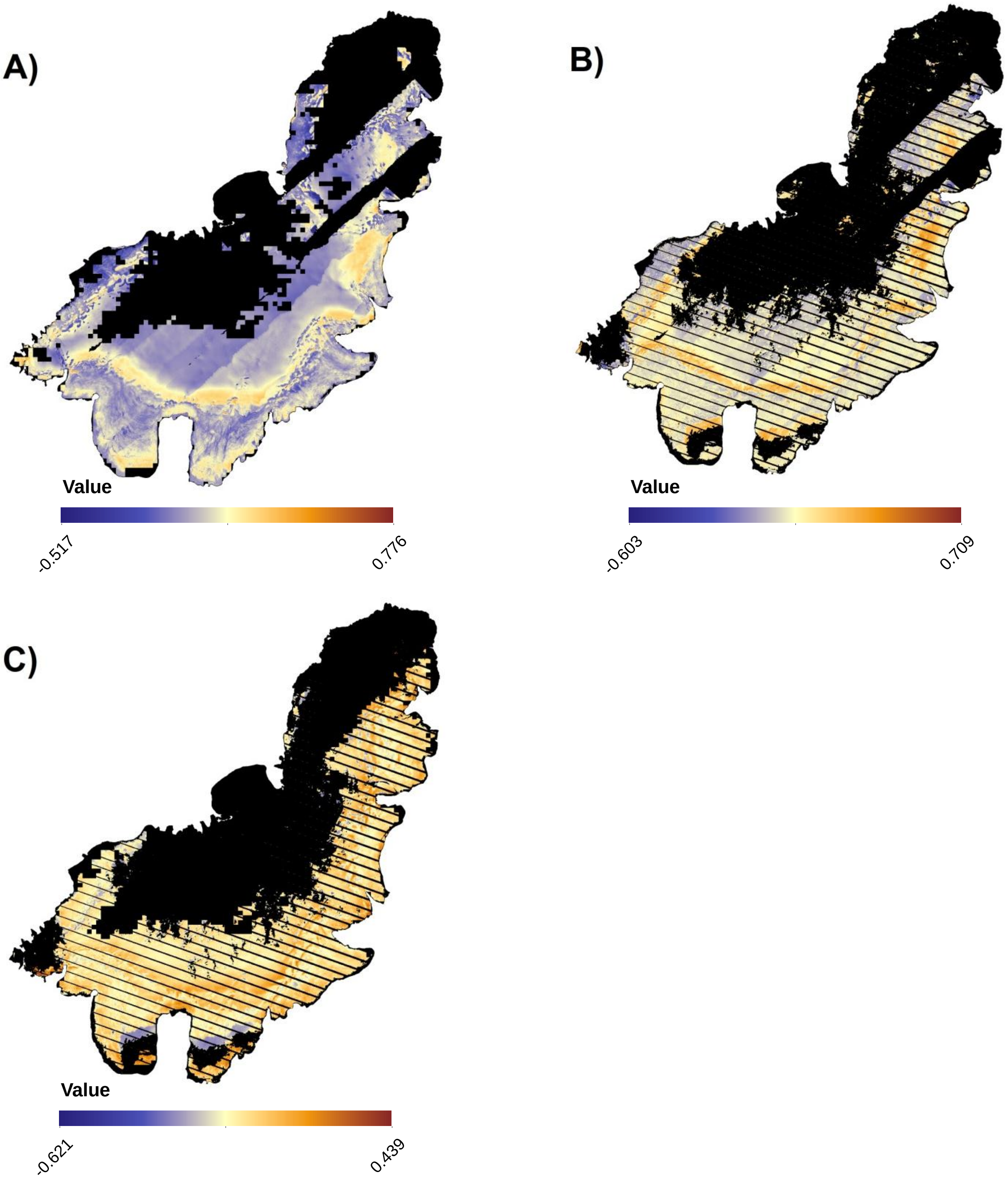

Figure 5.1: Map of difference in albedo values between A) ATMFlaash and MCD43; B) ATMFlaash and Landsat6S; Landsat6S and MCD43.

Figure 5.1 shows that there is a strong spatial element to the different albedo characteristics generated by the different platforms. Figure 5.1a and 5.1b show the derived ATMFlaash albedo values were less than the MCD43 and Landsat6S values in the accumulation area. Meanwhile, in areas of bare ice, the lower resolution datasets acted to overestimate the value of clean ice whilst greatly underestimating the albedo of debris covered ice. The impact of contrasting resolutions between the MODIS and ETM+ instruments can be seen by comparing the different figures. The regular debris bands are clearly visible in Figure 5.1a as a result of the large differences in the comparative differences between the ATM and MCD43 data. In contrast, in Figure 5.1b, the greater ability of the ETM+ instrument to capture some degree of the variability due to its 30m resolution means that the contrast in difference values is much smaller. Consequently it is extremely difficult to see the debris bands in 5.1b. The ETM+ instrument therefore is more adept at capturing the high degree of albedo spatial variability seen across the ablation area of Langjökull and previously demonstrated in the Svartárjökull analysis.

Whilst the ablation area characteristics at the spatial extent of the ice cap support the earlier analysis, conceivably more important is the underestimation feature visible in both Figure 5.1a and 5.1b and to a lesser extent 5.1c. The albedo underestimation feature, found in both the MCD43 and the Landsat6S albedo data represents the transition zone between bare ice and snow cover. The change from low albedo dirty ice to high albedo dry snow over very small spatial scales has resulted in the low resolution instruments being unable to adequately represent the surface. This zonal feature was shown in the Svartárjökull analysis by the spatial smoothing of the ETM+ instrument and the stepped albedo profile generated by the MCD43 product. Furthermore, this albedo feature was recognisable in the pixel analysis as a result of the characteristics present in the 0.370 MCD43 pixel.

These characteristics have a number of very important implications for surface energy balance models. First, the MCD43 product appears to be giving snow areas an overly high albedo. This is consistent with both the Svartárjökull analysis and the bias in individual MODIS pixels seen in section 4.3.1. Consequently, surface energy balance model validation using MCD43 data will result in too little melt being generated in the accumulation area. Second, the lower resolution instruments struggle to capture the spatial variability of albedo in the ablation area. Although the over and underestimation of albedo for different surface types should reduce the impact of this inability to accurately represent the surface, there is a tendency to underestimate albedo as outlined in section

4.3.1 and 4.3.2. Third, the value of the albedo differences in the transition zone between the high resolution and low resolution datasets could have severe consequences for modelling. Unlike the ablation area where the value difference is small due to the low albedo nature of the area, the albedo in the transition zone ranged from 0.14 to 0.56. Any inability to capture this variability, or at the very least to average it, will therefore have a large impact on the modelled spatial characteristics of melting and snowline migration upglacier; a conclusion that has been supported by each of the different spatial extent analyses. Fundamentally, it is the proportion of the surface of the ice covered by each of these different surface facies that will therefore control the ability to accurately produce a mean albedo value across the ice cap.

5.1.2 Surface energy balance implications

In order to try to quantify the impact of the different resolution of each of the datasets and the resulting mean albedos derived across the different spatial coverage as generated in section 4.3, the impact of albedo differences on melt will now be estimated. From the standpoint of calculating varying melt across the ice cap, the difference in mean albedo values between the different resolution datasets (ATM, ETM+ and MODIS) is will impact on the calculation of melt due to the net shortwave radiation flux. To estimate this impact, the difference between the melt associated with the net shortwave radiation flux across the different datasets was quantified. This was achieved by assuming a uniform horizontal surface with no shading in combination with an incoming shortwave flux of 140Wm^{-2} per day, an average figure for Langjökull in August. With this assumption, estimates of the different amounts of melt associated with each dataset are calculated using the mean albedo values calculated in section 4.3.

The average difference between the 11 MCD43 pixel albedo values and the corresponding mean ATMFlaash pixel albedo values generated in section 4.3.1 resulted in an additional melt of 0.644mm/m^{2} using the ATMFlaash values. Evidently, when the albedo values corresponding to each MCD43 pixel albedo are considered in isolation the difference in melt volume produced is highly variable. The difference in estimated melt ranges from an addition melt 4.208mm/m^{2} for the MCD43 pixel with an albedo of 0.233 to 4.017mm/m^{2} less melt for the 0.370 MCD43 pixel. The difference between the mean values of the ATMFlaash dataset and the MCD43 dataset increases across Svartárjökull thus predicting an additional 0.940mm/m^{-2}. The difference between the mean values is at its least across the ice cap as a whole, meaning that the ATMFlaash dataset only estimates an addition 0.289mm/m^{-2}.

The differences between the melt predicted by the Landsat6S and MCD43 albedo values follows a similar trend. For the 11 MODIS pixels, the different mean values result in the Landsat6S dataset predicting an addition 1.024mm/m^{2} compared to the MCD43 pixel values. Despite the range of different melt estimates across the 11 pixels being greater than the ATMFlaash dataset, ranging from an additional 5.052mm/m^{2} to 4.690mm/m^{2} less than the MCD43 estimate, there is an overall inclination towards greater melting. This tendency towards greater melting, eight of the MCD43 pixel suggesting less melting, results in the greater average additional melt predicted by the Landsat6S dataset compared to the ATMFlaash dataset. The increase in spatial coverage of the samples taken had the same impact on the estimated addition melt predicted by the Landsat6S dataset compared to the MCD43 dataset as was shown by the ATMFlaash dataset. Across Svartárjökull the estimated addition melt rose to 1.373mm/m^{2}. However, when Langjökull as a whole was considered, the additional melt figure dropped to 0.470mm/m^{2}.

In comparison to the differences in estimated melt, the differences between the Landsat6S data and the ATMFlaash data are smaller than the comparison of the two datasets to the MCD43 dataset. For the area of the 11 MODIS pixels, the Landsat6S albedo values predict an additional 0.380mm/m^{2} compared to the ATMFlaash dataset. This figure rises for the Svartárjökull basin to 0.434mm/m^{2} before dropping across Langjökull to 0.180mm/m^{2}. Critically, the increase in difference between these two datasets for the Svartárjökull basin is also present between these two datasets and the MCD43 dataset.

5.2 Methods used to derive albedo from the different instruments

The analysis of the surface reflectance characteristics of Langjökull has shown that there is a large difference between the albedo values derived from the different datasets. This has been a consequence both of the different spatial resolutions of the instruments used and the different methods by which broadband albedo values were generated from the raw instrument data. This section of the discussion will focus on the differences between the different methods used to derive albedo values and the problems associated with each method, as well as the errors inherent in the data.

5.2.1 ATMSolar Vs ATMFlaash

The ability to derive surface albedo from the ATM radiance data using the FLAASH atmospheric correction model was contrasted by the inability of the solar spectrum radiance calibration. Analysis of the results indicated that the ATMFlaash albedo values appeared to be representative of the surface albedo and were broadly in agreement with the previously validated methods of deriving albedo. This was principally demonstrated in section 4.2. In contrast, the ATMSolar albedo values were found to be substantially higher than the ATMFlaash albedo values as well as appearing unable to derive precise snow albedo. Consequently a problem must exist with the method used to derive surface albedo using a solar spectrum to calibrate the data.

Analysis of the solar spectrum method of calibration to produce albedo values illuminates one major source of error; the solar spectrum used to make the corrections. Errors derived from the solar spectrum are primarily the result of the intensity of the irradiance being measured. In order to precisely derive the surface albedo from the measured radiance data, the measured solar spectrum intensity would have to be the same as the solar spectrum at the time that the radiance was measured. Unfortunately, the solar spectrum used in this study was measured on the 25 August, nearly a month after the ATM sortie. Therefore despite the chosen solar spectrum being the brightest available, the solar incidence angle is likely to result in a lower intensity solar spectrum than the one that resulted in the measured radiance values.

Further errors may also be incorporated through this method of albedo retrieval as a consequence of both the equipment and conditions under which the *in situ* measurements were made. First, calculation of the spectral irradiance incident to the panel is based on the radiometric calibration files provided by the FSF. These are likely to contain a degree of error, both as a result of measurement imprecision and the time taken between calibration and measurement using the panel. Crucially no calibration measurements were made in the field. Second there is no guarantee that the atmospheric conditions when the panel measurements were made were identical to those present when the ATM instrument was flown despite the similarly cloudless conditions.

Indications that the measured solar spectrum is the principle cause of the disparity in results between the ATMFlaash and the ATMSolar albedo datasets is present throughout section 4 but particularly in section 4.2 and 4.3.1. The greater albedo values generated by the ATMSolar dataset implied that the weighted average used to convert the radiance to reflectance was too low. Principally this is the result of a lower intensity spectrum. In addition, the difference between the albedo values is not constant but increases as albedo increases. Best shown by the transect analysis, the trend line attached to the different ATM datasets showed the formula differences were multiplicative rather than additive differences. This multiplicative difference between the dataset formulae validates the assumption that the solar spectrum was insufficiently bright. Consequently, this method of deriving albedo from ATM radiance data may in fact be effective at generating precise albedo values if the correct spectrum is used.

Despite, the apparent success of FLAASH to carry out atmospheric corrections on the ATM swaths, this method was not without problems. Shown by the different coverage of the ATMFlaash dataset compared to the ATMSolar dataset, a major problem was found resulting from available computing power. The temporary disk space required by FLAASH is in the order of 5 times the size of the data file to be corrected (Kruse, 2004). This results from the production of two temporary files, twice the size of the original dataset, as well as the output file. The consequence of this need for temporary disk space was that the available computers were unable to process either the a214e051 or the a214e071 swaths; these two swaths being the largest datasets at 2.2Gb and 2.1Gb respectively. Whilst attempts were made at reducing their size by splitting the individual swaths into four parts, this had the unfortunate by-product of impacting upon the atmospheric correction. Principally this was the result of changing the dark land pixels and bright calibration targets that were being used to remove the impacts of water vapour and aerosols in the atmosphere. In light of this issue, the decision was taken not to include these two swaths in the final results.

FLAASH may also have resulted in the incorporation of errors as a result of it being a non-image specific correction model. Specifically, the model uses an idealised atmosphere based on latitudinal location and time of year, as well as an aerosol model based on an estimation of the aerosol type present (FLAASH User's Guide, 2009). Therefore unlike the 6S and dark pixel atmospheric correction methods which were image specific, FLAASH is likely to be slightly less accurate as a result of its generalised nature.

The use of FLAASH to carry out atmospheric corrections on the ATM dataset also included one major assumption. Unlike, satellite instruments collecting multispectral data, the viewing angle changes substantially for the ATM instrument over each individual swath. For example, the Daedalus 1268 used in this study had a viewing angle over each swath of between 45^0 and -45^0. The consequence of this variable viewing angle is that the atmospheric transmission path increases with distance away from nadir and therefore the impact of atmospheric scattering and absorption increases (Callison et al., 1987; Rees, 2006). Critically the other assumptions incorporated into the FLAASH model means that it is extremely difficult to try to quantify the impact of the viewing angle variation beyond visual inspection. Viewing angle differences appear, however, to have a negligible impact on the ATMFlaash dataset. In order to overcome this issue in the future and derive more accurate albedo measurements, a correction for variable viewing angle should be incorporated into either FLAASH or the 6S radiative transfer code in order to effectively model the impact of atmospheric propagation on the derived ATM instrument data.

5.2.2 Other sources of error in the ATM albedo datasets

A number of other error sources exist in the ATM data, independent of the issues associated with either the solar spectrum intensity or the atmospheric model assumptions. Principle among these is the assumption of an isotropic surface. Alluded to in section 1.2, snow and ice have often been found to be anisotropic scattering surfaces and in particular they are effective forward-scatterers. Having been unable to model the surface BRDF, evidence of the anisotropic scattering is demonstrated by the stripping which is evident in Figure 4.1. As this characteristic is directly linked to the solar incidence angle and the viewing angle, the flight direction has the impact of changing the viewing angle relative to the incidence angle (Choudhury and Chang, 1981; Wendisch et al., 2004). Overcoming this problem led to a number of solutions for both the spectrum calibrated dataset and the FLAASH correction dataset. The simplest step to overcome the lack of BRDF modelling was to use the conclusion that the BRDF is “faily well-bahaved” near nadir (Greuell and de Ruyter de Wildt, 1999) meaning that no extraction transects or individual pixels were taken near to the margins of the individual swaths. The additional step would have been to adjust the histograms of identical regions according to the method demonstrated by Bucher (2004) using histogram peaks. However, with very limited cross over between individual swaths, any correction would have been somewhat artificial and as much an adjustment based on atmospheric propagation at extreme viewing angles, as an adjustment for flight direction.

In the case of the FLAASH corrected dataset, the impacts of flight direction were greatly reduced by the atmospheric model itself. Critical input parameters for the modelling process, solar position and incidence angle, were included when the model was run. Furthermore, the inability to process a214e051 or a214e071 meant that the vast majority of the ATMFlaash albedo map was made up of swaths from flightlines in the same direction. This represented one of the major reasons for predominantly using the ATMFlaash dataset throughout the study.

A further correction not carried out for the ATM data and therefore another source of error, is that for topography. Topography has a significant impact on measured albedo as a consequence of the variations in incident radiation (Klok and Oerlemans, 2002; Klok et al., 2003; Arnold et al., 2006). Moreover, the Dumont et al. (2012) study concluded that a topographic correction was more important for a surface assumed to be Lambertian scattering than a non-Lambertian surface. In spite of this, the decision was made not to correct for surface topography as a consequence of the different spatial resolutions of the available datasets. Whilst it would have been acceptable to correct the satellite datasets with the available ASTER GDEM, due to their 30m resolutions, it was felt that the spatial resolution of the ATM dataset prevented its correction using the same DEM. The use of a 30m resolution DEM to correct a 5m resolution dataset would have resulted in the generation an artificially corrected albedo dataset.

In addition to these issues it must also be recognised that not all of the ATM data was used in this study. Before swaths were excluded by the FLAASH atmospheric correction modelling process, a number of swaths had to be excluded as a consequence of an inability to sufficiently georeference them. The majority of these swaths only contained remotely sensed data from the ice cap itself. Therefore as the surface conditions were not constant between the acquisition of the ETM+ image used for georeferencing and the ATM acquisition there was no way to georeference them accurately enough for the purpose of this comparative study. Moreover, they contained no significant features in the proglacial area which would have allowed accurate georeferencing.

5.2.3 Atmospheric correction methods for ETM+ images

The success of atmospheric corrections and the conversion of radiance to albedo values for the ATM data using FLAASH is contrasted by its apparent failure to accurately correct the ETM+ image. This failure is probably the result of the model being non-specific to each image it is correcting. In comparison, although the dark pixel method of atmospheric correction relies on assumptions, it does use information from within the ETM+ image in order to make the correction. Meanwhile the 6S atmospheric correction model used a model atmosphere derived from remotely sensed MODIS data for the day the ETM+ image was derived. The contrasts between the image specific method of atmospheric correction and the use of a generalised atmospheric structure do therefore make a significant difference for derive albedo from ETM+ images and therefore specific models should be used in the future.

5.2.4 Errors in the ETM+ albedo data

Despite the number of errors incorporated into the ETM+ albedo data being smaller than the number associated with the ATM data, a number must still be acknowledged. Firstly, an error may have been introduced into the ETM+ data through uncertainties in the calibration. The ETM+ sensor was originally calibrated against a number of Earth targets with known reflectance values. Through this process the ETM+ sensor was found to be one of the most stable sensor arrays as there was very little variation in radiometric gains over time (Thome, 2001). Having established the original calibration, the ETM+ sensor has constantly been monitored using onboard calibrators allowing quarterly production of calibration parameter files to be generated which are subsequently used during the radiometric calibration process (Chander et al., 2009). These files have a calibration uncertainty of ±5% which is subsequently incorporated into the ETM+ datasets (Markham et al., 2003; 2004).

In addition, to the calibration uncertainty, the other errors present in the ETM+ albedo data were also present in the ATM data. Principally these are related to the assumption of a Lambertian scattering surface. As demonstrated by the ATM data, the snow and ice surface present on Langjökull were not Lambertian surfaces. The ETM+ data therefore also incorporates the error associated with the lack of a topography correction and a BRDF model. Whilst the former could have been corrected for, the lack of a topographic correction for the ATM data would mean a dissimilar number of corrections would have been carried out on the different datasets.

5.2.5 Temporal differences between image acquisitions

In addition to the differences between the different methods of deriving albedos from the various platforms, the temporal differences between image acquisitions must be considered. The ETM+ image was acquired nearly two weeks after the ATM sortie was flown and the MCD43 product was a composite of 8 days worth of measurements either side of the 5 August 2007. The two week difference between the ETM+ image and the ATM swaths may explain some of the difference between the two datasets as this would provide an opportunity for the snow surface to metamorphose and darken. Despite this the spatial pattern of albedo is similar as shown throughout section 4 and thus the conclusions are believed to be valid. In the case of the MCD43 product, analysis of the data used to derive the image that was utilized shows that the ATM and MODIS datasets are temporally more similar than first thought. The MOD09 and MYD09 images that were used to generate the 16-day composite over Langjökull were in fact all cloudy. Consequently, the majority of the images were automatically dismissed. The exceptions were images acquired on the 2 August 2007 which were made under mostly clear skies. The composite image is therefore only derived from the day the ATM was acquired and thus is directly comparable. Moreover the extent of cloud cover suggests that the amount of melting between the ATM and ETM+ acquisitions was significantly reduced by the lack of direct sunlight. Instead the impact of sensible heat provided by rain may have played a more important role in altering the snow characteristics.

6. Conclusion

The study presented has attempted to demonstrate the ability of different resolution instruments using various retrieval methods to accurately measure the surface albedo across Langjökull. The study demonstrated that the surface albedo of Langjökull is highly variable and that the measured variability increased both with increases in the sample area and resolution of the multispectral instruments. The value of the measured albedos from the different instruments did, however, depend on the retrieval methods used and as a result, some methods were found to be preferable over others.

For the ATM data, this study showed that the use of the available solar spectrum to calibrate the ATM radiance data was unsuitable. This method resulted in the dataset being unable to accurately resolve a broadband albedo over higher albedo snow areas, whilst in lower albedo areas where an appropriate broadband albedo was achieved, the results were overly high compared to the other datasets. The study did, however, indicate that the use of solar spectrum measurements could be used to derive surface albedo from measured radiance data as a quick and easy alternative to atmospheric modelling if a suitable intensity spectrum were available. In contrast, the use of the FLAASH atmospheric correction model on the ATM data appeared to generate extremely accurate surface albedo measurements from the ATM data and therefore proved the best method to derive albedo from this instrument. For the ETM+ data, in contrast to the ATM data, the use of the FLAASH atmospheric correction model resulted in the generation of the most inaccurate surface albedo when compared to the other methods used for this instrument. Therefore in the case of the ETM+ the use of either dark pixel empirical correction or atmospheric correction using the 6S model is preferable.

In terms of comparability between the datasets, the transect analysis provided a number of different results. Across relatively homogenous snow areas there was general agreement between the ATMFlaash, Landsat6S, LandsatDP and MCD43 albedo values, in spite of the different resolutions. However, the transects placed across regions of variable ice facies indicated a degree of variability in terms of both which datasets were in the closest agreement and the absolute values. Combined with results from the transect placed with an upglacier alignment, the variability between the datasets suggested differences related to the spatial resolution of the different instruments.

Consequently the differences between the datasets were analysed both in terms of a spatial resolution and changing spatial extents. The different analysis at various spatial extents indicated a number of characteristics. First, the variability of albedo increased the higher the resolution of the instrument. Second, the variability of albedo increased with sample size being investigated. Consequently, it was clear that even over surfaces thought to be relatively homogenous at lower resolutions, the surface albedo was in fact highly variable at spatial scales of 2.5×10^5 m^2. Whilst trends in variability were fairly uniform with increases in resolution and sample size, the mean value characteristics and correlation between the different datasets was much more variable. At the smallest sample size, that of the 11 MODIS pixels, the datasets were highly correlated and the difference in mean values was relatively small for each MODIS pixel. When sampled across Svartárjökull the difference between the dataset mean values increased whilst the correlation dropped significantly. At the largest sample size, Langjökull, these trends were reversed with the difference between the mean values being the smallest over the different spatial scales and the dataset correlations being slightly greater than those seen across Svartárjökull. These findings combined with the mapping of differences between the datasets demonstrated the large impacts that changing spatial resolutions have on remotely sensed albedo data.

On the scale of individual MODIS pixels, the lower resolution data was seen to lose the spatial heterogeneity displayed by the ice cap surface. More importantly, however, it also showed that the lower resolution instruments had a representational bias. The result of this bias was to portray high albedo areas combined with small numbers of abnormally low albedo areas as having an overly low albedo. The opposite trend was seen in low albedo areas. Consequently, when applied to the ice cap as a whole this representation issue served to average the impacts across the ice cap thus producing close mean values. The analysis across Svartárjökull demonstrates the impact of high and low bias not being equal as the difference between the mean values is the greatest. The albedo characteristics portrayed across Svartárjökull are primarily the result of the rapid changes in albedo across this drainage basin due to the short transition between different facie types. Furthermore, the low resolution instruments were seen to be unable to accurately represent the surface albedo of the firn zone due to the wide range of surface albedos. The analysis over this basin, combined with the spatial differences between the low and high resolution datasets across Langjökull, indicate that the difference between the mean results is likely to vary throughout the ablation season as a consequence of the changing surface types. It therefore appears that such changes would impact greatest upon the ability of the MCD43 product to produce an accurate surface albedo map due to its inability to represent heterogeneous surfaces.

Despite these characteristics between the different datasets, the relative order of mean albedo is maintained across all sample sizes. The MCD43 dataset estimates the surface albedo to be the highest, followed by the ATMFlaash dataset and the Landsat6S dataset. Moreover, the differences ATMFlaash dataset and Landsat6S dataset are smaller than between the ATMFlaash dataset and the MCD43 dataset. This is also indicated by the greater correlation shown between the higher resolution datasets across all the sample sizes.

These findings clearly pose problems for studies using ground validation points. The highly variable nature of albedo, in conjunction with the bias shown indicates that the use of point measurements to validate remotely sensed multispectral imagery is highly problematic. This is especially true in areas with high variable surface albedo. Despite this, the lack of point validation measurements for this study does represent a fundamental limitation of the study. The numerous processing steps needed to generate accurate ATM albedos means that ground measurements would have been extremely helpful in validating the ATM albedo values. Furthermore, unlike the low resolution nature of the ETM+ and MODIS imagery, point measurements would likely be more representative of a 5x5m area represented by the ATM pixels. Future studies using ATM data for glaciological applications should therefore be accompanied by a limited ground campaign in order to provide *in situ* albedo measurements.

This study has therefore generated a number of key points for future remote sensing based studies of surface albedo and energy balance modelling. Whilst there are obvious cost implications as well as computational complications in deriving accurate high resolution albedo data, ATM multispectral data provides an effective means of comparison and validation for satellite multispectral imagery. *In situ* measurements would also allow for the calculation of the different surface BRDFs thereby allowing even greater ATM data precision (Lyapustin and Privette, 1999; Jacob et al., 2002; Wu and Tong, 2011). The continuous coverage, rather than point measurement, achieved by the ATM means the ATM albedo values derived for a given area are far more representative of the surface. Furthermore, the ability to show bias within individual pixels of low resolution imagery is crucial to generating higher precision albedo maps using other remote sensing systems.

These results also have wider glaciological implications. Although inappropriate over ice sheets and the largest ice caps, surface energy balance models over alpine glacier and small ice caps may have to be of the same resolution of the ATM data in order to accurately assess the impacts of surface albedo. Crucially, previous attempts to utilise high resolution airborne data for similar purposes have been fundamentally limited by the lack of sufficiently high resolution DEMs (Molotch et al., 2004; Molotch and Bales, 2006). Instead, the airborne data has been resampled to lower resolutions in order for the resolution to match the available DEM thus foregoing the advantages of the high resolution dataset (Molotch and Bales, 2006).With this in mind, the future use of high resolution airborne data would be greatly facilitated by the addition of lidar instruments to each sortie, although 'Structure-from-Motion' photogrammetry may eventually provide a suitable alternative (Westoby et al., 2012). Where it is not possible to collect ATM data on a regular basis, this study has shown Landsat to be of sufficiently high resolution and therefore Landsat-8 should be used to monitor ice masses with highly variable surface types.

Even for ice sheet studies these findings have possible implications. Whilst numerous studies have looked to quantify changing albedo over time (Greuell and Oerlemans, 2005; Stroeve et al., 2005; Box et al., 2006, 2012) and are more concerned with albedo change rather than precise values, surface energy balance modelling will require precise albedo values to be derived. The impacts of spatially variable ice albedo were clearly shown by the van Angelen et al. (2012) surface mass balance study using MODIS satellite retrievals, and in particular in low albedo regions. However, this study has clearly demonstrated that the appropriateness of MODIS data for these studies is dependent on the surface characteristics and the spatial variability of surface albedo, whilst measurement bias further hinders the accuracy of this instrument. The conclusions from this study are therefore critical for monitoring high Arctic GICs, mountain glaciers and ice sheets in the 21st Century.

7. Appendix

L7 ETM+ Sensor (Qcalmin=1 and Qcalmax=255)								
Band	Spectral Range	Centre Wavelength		LMIN$_{\lambda}$	LMAX$_{\lambda}$	G$_{rescale}$	B$_{rescale}$	ESUN$_{\lambda}$
Units	µm			W/(m2 sr µm)		(W/m2 sr µm)/DN	W/(m2 sr µm)	W/(m2 µm)
Low gain (LPGS)								
1	0.452–0.514	0.483		−6.2	293.7	1.180709	−7.38	1997
2	0.519–0.601	0.560		−6.4	300.9	1.209843	−7.61	1812
3	0.631–0.692	0.662		−5.0	234.4	0.94252	−5.94	1533
4	0.772–0.898	0.835		−5.1	241.1	0.969291	−6.07	1039
5	1.547–1.748	1.648		−1.0	47.57	0.19122	−1.19	230.8
6	10.31–12.36	11.335		0	17.04	0.067087	−0.07	N/A
7	2.065–2.346	2.206		−0.35	16.54	0.066496	−0.42	84.9
PAN	0.515–0.896	0.706		−4.7	243.1	0.975591	−5.68	1362
High Gain (LPGS)								
1	0.452–0.514	0.483		−6.2	191.6	0.77874	−6.98	1997
2	0.519–0.601	0.560		−6.4	196.5	0.798819	−7.20	1812
3	0.631–0.692	0.662		−5.0	152.9	0.621654	−5.62	1533
4	0.772–0.898	0.835		−5.1	157.4	0.639764	−5.74	1039
5	1.547–1.748	1.648		−1.0	31.06	0.12622	−1.13	230.8
6	10.31–12.36	11.335		0	12.65	0.037205	3.16	N/A
7	2.065–2.346	2.206		−0.35	10.8	0.043898	−0.39	84.9
PAN	0.515–0.896	0.706		−4.7	158.3	0.641732	−5.34	1362

Table 7.1: ETM+ spectral range, post-calibration dynamic ranges, and mean exoatmospheric solar irradiance (ESUNλ).

Earth–Sun distance (*d*) in astronomical units for Day of the Year (DOY).

											d
DOY	*d*	DOY	*d*	DOY	*d*	DOY	*d*	DOY	*d*	DOY	0.9936
1	0.9833	61	0.9911	121	1.0076	181	1.0167	241	1.0099	301	0.9933
2	0.9833	62	0.9913	122	1.0078	182	1.0167	242	1.0097	302	0.9931
3	0.9833	63	0.9916	123	1.0081	183	1.0167	243	1.0095	303	0.9928
4	0.9833	64	0.9918	124	1.0083	184	1.0167	244	1.0092	304	0.9925
5	0.9833	65	0.9921	125	1.0086	185	1.0167	245	1.009	305	0.9923
6	0.9833	66	0.9923	126	1.0088	186	1.0167	246	1.0087	306	0.992
7	0.9833	67	0.9926	127	1.009	187	1.0167	247	1.0085	307	0.9918
8	0.9834	68	0.9929	128	1.0093	188	1.0167	248	1.0083	308	0.9915
9	0.9834	69	0.9931	129	1.0095	189	1.0167	249	1.008	309	0.9913
10	0.9834	70	0.9934	130	1.0098	190	1.0167	250	1.0078	310	0.991
11	0.9835	71	0.9937	131	1.01	191	1.0166	251	1.0075	311	0.9908
12	0.9835	72	0.9939	132	1.0102	192	1.0166	252	1.0072	312	0.9905
13	0.9835	73	0.9942	133	1.0104	193	1.0166	253	1.007	313	0.9903
14	0.9836	74	0.9945	134	1.0107	194	1.0166	254	1.0067	314	0.9901
15	0.9837	75	0.9947	135	1.0109	195	1.0165	255	1.0065	315	0.9898
16	0.9837	76	0.995	136	1.0111	196	1.0165	256	1.0062	316	0.9896
17	0.9838	77	0.9953	137	1.0113	197	1.0164	257	1.0059	317	0.9894
18	0.9839	78	0.9956	138	1.0115	198	1.0164	258	1.0057	318	0.9892
19	0.9839	79	0.9958	139	1.0117	199	1.0163	259	1.0054	319	0.9889
20	0.984	80	0.9961	140	1.0119	200	1.0162	260	1.0051	320	0.9887
21	0.9841	81	0.9964	141	1.0121	201	1.0162	261	1.0049	321	0.9885
22	0.9842	82	0.9967	142	1.0123	202	1.0161	262	1.0046	322	0.9883
23	0.9843	83	0.997	143	1.0125	203	1.016	263	1.0043	323	0.9881
24	0.9844	84	0.9973	144	1.0127	204	1.0159	264	1.004	324	0.9879
25	0.9845	85	0.9975	145	1.0129	205	1.0158	265	1.0037	325	0.9877
26	0.9846	86	0.9978	146	1.013	206	1.0158	266	1.0035	326	0.9875
27	0.9847	87	0.9981	147	1.0132	207	1.0157	267	1.0032	327	0.9873
28	0.9848	88	0.9984	148	1.0134	208	1.0156	268	1.0029	328	0.9871
29	0.985	89	0.9987	149	1.0136	209	1.0154	269	1.0026	329	0.9869
30	0.9851	90	0.999	150	1.0137	210	1.0153	270	1.0023	330	0.9868
31	0.9852	91	0.9993	151	1.0139	211	1.0152	271	1.0021	331	0.9866
32	0.9854	92	0.9995	152	1.014	212	1.0151	272	1.0018	332	0.9864
33	0.9855	93	0.9998	153	1.0142	213	1.015	273	1.0015	333	0.9862
34	0.9857	94	1.0001	154	1.0143	214	1.0149	274	1.0012	334	0.9861
35	0.9858	95	1.0004	155	1.0145	215	1.0147	275	1.0009	335	0.9859
36	0.986	96	1.0007	156	1.0146	216	1.0146	276	1.0006	336	0.9858
37	0.9861	97	1.001	157	1.0148	217	1.0144	277	1.0003	337	0.9856
38	0.9863	98	1.0013	158	1.0149	218	1.0143	278	1.0001	338	0.9855
39	0.9865	99	1.0016	159	1.015	219	1.0141	279	0.9998	339	0.9853
40	0.9866	100	1.0018	160	1.0151	220	1.014	280	0.9995	340	0.9852
41	0.9868	101	1.0021	161	1.0152	221	1.0138	281	0.9992	341	0.9851

42	0.987	102	1.0024	162	1.0154	222	1.0137	282	0.9989	342	0.9849
43	0.9872	103	1.0027	163	1.0155	223	1.0135	283	0.9986	343	0.9848
44	0.9874	104	1.003	164	1.0156	224	1.0133	284	0.9983	344	0.9847
45	0.9876	105	1.0033	165	1.0157	225	1.0132	285	0.998	345	0.9846
46	0.9877	106	1.0035	166	1.0158	226	1.013	286	0.9978	346	0.9845
47	0.9879	107	1.0038	167	1.0159	227	1.0128	287	0.9975	347	0.9844
48	0.9881	108	1.0041	168	1.016	228	1.0126	288	0.9972	348	0.9843
49	0.9884	109	1.0044	169	1.016	229	1.0124	289	0.9969	349	0.9842
50	0.9886	110	1.0046	170	1.0161	230	1.0123	290	0.9966	350	0.9841
51	0.9888	111	1.0049	171	1.0162	231	1.0121	291	0.9963	351	0.984
52	0.989	112	1.0052	172	1.0163	232	1.0119	292	0.9961	352	0.9839
53	0.9892	113	1.0055	173	1.0163	233	1.0117	293	0.9958	353	0.9838
54	0.9894	114	1.0057	174	1.0164	234	1.0115	294	0.9955	354	0.9838
55	0.9897	115	1.006	175	1.0164	235	1.0112	295	0.9952	355	0.9837
56	0.9899	116	1.0063	176	1.0165	236	1.011	296	0.9949	356	0.9836
57	0.9901	117	1.0065	177	1.0165	237	1.0108	297	0.9947	357	0.9836
58	0.9904	118	1.0068	178	1.0166	238	1.0106	298	0.9944	358	0.9835
59	0.9906	119	1.0071	179	1.0166	239	1.0104	299	0.9941	359	0.9835
60	0.9908	120	1.0073	180	1.0166	240	1.0102	300	0.9939	360	0.9834
										361	0.9834
										362	0.9834
										363	0.9834
										364	0.9833
										365	0.9833

(Table 7.2: Earth-sun distances throughout the year)

8. References

Adler-Golden, S. M., Matthew, M. W., Bernstein, L. S., Levine, R. Y., Berk, A., Richtsmeier, S. C., Acharya, P. K., Anderson, G. P., Felde, G., Gardner, J., Hoke, M., Jeong, L. S., Pukall, B., Mello, J., Ratkowski, A., and Burke, H.–H. 1999. Atmospheric correction for shortwave spectral imagery based on MODTRAN4. *SPIE Proceeding, Imaging Spectrometry V*, 3753, 61-69.

Anderson, B., Lawson, W., Owens, I., and Goodsell, B. 2006. Past and future mass balance of Ka Roimata o Hine Hukatere (Franz Josef Glacier). *Journal of Glaciology*, 52, 179, 597-607.

Anderson, J. B. 1999. *Antarctic Marine Geology*, New York: Cambridge University Press.

Aniya, M., Sate, H., Naruse, R., Skvarca, P., and Casassa, G. 1996. The use of satellite and airborne imagery to inventory outlet glaciers on the southern Patagonia icefield, South America. *Photogrammetric Engineering and remote sensing*, 62, 12, 1361-1369.

Arendt, A. 1999. Approaches to modelling the surface albedo of a high arctic glacier. *Geographical Annals*, 81A, 4, 477-487.

Arnold, N. S., and Rees, W. G. 2003. Self-similarity in glacier surface characteristics. *Journal of Glaciology*, 49, 167, 547-554.

Arnold, N. S., Rees, W. G., Hodson, A. J., and Kohler, J. 2006. Topographic controls on the surface energy balance of a high Arctic glacier. *Journal of Geophysical Research*, 111 F02011, doi:10.1029/2005JF000426.

Arnold, N. S., Willis, I. C., Sharp, M. J., Richards, K. S., and Lawson, W. J. 1996. A distributed surface energy balance model for a small valley glacier. I. Development and testing for Haut Glacier d'Arolla, Valais, Switzerland. *Journal of Glaciology*, 42, 140, 77-89.

Atmospheric Correction Module, Version 4.7, 2009. *Atmospheric Correction Module: QUAC and FLAASH User's Guide.*

Azimuth Systems. 2005. AZGCORR Users Manual. Available at: http://arsf.nerc.ac.uk/documents/azgcorr_v5.pdf [Accessed November 1, 2012].

Bamber, J. L. and Kwok, R. 2004. Remote Sensing Techniques, *in Bamber, J. L., and Payne, A. J. (eds.); Mass Balance of the Cryosphere: Observations and modelling of contemporary and future changes.* 59-113.

Banwell, A. F., Willis, I. C., Arnold, N. S., Messerli, A., Rye, C. J., Tedesco, M., and Ahlstrøm, A. P. 2012. Calibration and evaluation of a high-resolution surface mass-balance model for Paakitsoq, West Greenland. *Journal of Glaciology*, 58, 212, 1047-1062.

Barry, R. G. 2011. The cryosphere – past, present and future: a review of the frozen water resources of the world. *Polar Geography*, 34, 4, 219-227.

Bell, R. E. 2008. The role of subglacial water in ice-sheet mass balance. *Nature Geoscience*, 1, 297-304.

Benn, D. I., and Evans, D. J. A., 2010. *Glaciers and Glaciation*, 2nd Edition, Hodder Education.

Benn, D. I., Bolch, T., Hands, K., Gulley, J., Luckman, A., Nicholson, L. I., Quincey, D., Thompson, S., Toumi, R., and Wiseman, S. 2012. Response of debris-covered glaciers in the Mount Everest region to recent warming, and implications for outburst flood hazards. *Earth-Science Reviews*, 114, 156-174.

Bishop, M. P., Shroder Jr, J. F., Hickman, B. L., Copland, L. 1998. Scale-dependent analysis of satellite imagery for characterisation of glacier surfaces in the Karakoram Himalaya. *Geomorphology,* 21, 217-232.

Björnsson, H., and Pálsson, F. 2008. Icelandic glaciers. *Jökull*, 58, 365-386.

Bolch, T., and Kamp, U. 2006. Glacier mapping in high mountains using DEMs, Landsat and ASTER data. *8th International symposium on high mountain remote sensing cartography, 37-48.*

Box, J. E., Bromwich, D. H., Veenhuis, B. A., Bai, L., Stroeve, J. C., Rogers, J. C., Steffen, K., Haran, T., and Wang, S. 2006. Greenland ice sheet surface mass balance variability (1988-2004) from calibrated Polar MM5 output. *Journal of Climate*, 19, 2783-2800.

Box, J. E., Fettweis, X., Stroeve, J. C., Tedesco, M., Hall, D. K., and Steffan, K. 2012. Greenland ice sheet albedo feedback: thermodynamics and atmospheric drivers. *Cryosphere*, 6, 821-839.

Boyd, D. S. 2009. Remote sensing in physical geography: a 21st Century perspective. *Progress in Physical Geography*, 33, 4, 451-456.

Braithwaite, R. J. 2002. Glacier mass balance: the first 50 years of international monitoring. *Progress in Physical Geography*, 26, 1, 76-95.

Brock, B.W., and Arnold, N.S. 2000. A spreadsheet-based (Microsoft Excel) point surface energy balance model for glacier and snow melt studies. *Earth Surface Processes and Landforms*, 25, 649-658.

Brock, B. W., Willis, I. C., Sharp, M. J., and Arnold, N. S. 2000. Modelling seasonal and spatial variations in the surface energy balance of Haut Glacier d'Arolla, Switerland. *Annals of Glaciology*, 31, 53-62.

Bromwich, D. H., Bai, L., and Bjarnason, G. G. 2006. High-resolution regional climate simulations over Iceland using Polar MM5. *Mountain Weather Review*, 133, 3527-3547.

Bucher, T. 2004. Directional effects (view angle, sun angle, flight direction) in multi-angular high resolution image data – examples and conclusions from HRSC-A(X) flight examples. *Remote Sensing for Environmental Monitoring, GIS Applications, and Geology III*, *Proceedings of SPIE*, 5239, 234-243.

Callison, R. D., Blake, P., and Anderson, J. M. 1987. The quantitative use of Airborne Thematic Mapper infrared data. *International Journal of Remote Sensing*, 8, 1, 113-126.

Campbell, J. B. 2002. *Introduction to remote sensing,* 3rd Edition, The Guildford Press.

Chander, G., Meyer, D. J., and Helder, D. L. 2004. Cross-calibration of the Landsat-7 ETM+ and EO-1 ALI sensors. *IEEE Transactions on Geoscience and Remote Sensing*, 42, 12, 2821-2831.

Chander, G., Angal, A., Choi, T., Meyer, D. J., Xiong, X., and Teillet, P. M. 2007. Cross-calibration of the Terra MODIS, Landsat-7 ETM+ and EO-1 ALI sensors using near simultaneous surface observation over Railroad Valley Playa, Nevada test site. In Butler, J. J. and Xiong, J. (eds.) *Proceedings of SPIE Conference 6677 on Earth Observing Systems XII, SPIE, Vol 6677,* (pp. 66770Y: 1-12) San Diego, CA.

Chander, G., Coan, M. J. and Scaramuzza, P. L. 2008. Evaluation and comparison on the IRS-P6 and the Landsat Sensors. *IEEE Transactions on Geoscience and Remote Sensing*, 46, 1, 209-221.

Chander, G., Markham, B.L., and Helder, D.L. 2009. Summary of current radiometric calibration coefficients for Landsat MSS, TM, ETM+, and EO-1 ALI sensors. *Remote Sensing of Environment*, 113, 893-903.

Chen, J. L., Wilson, C. R., Tapley, B. D., Famiglietti, J. S., and Rodell, M. 2005. Seasonal global mean sea level change from satellite altimter, GRACE, and geophysical models. *Journal of Geodesy*, 79, 9, 532-539.

Chen, J. L., Wilson, C. R., Tapley, B. D., Blankenship, D., and Young, D. 2008. Antarctic regional ice loss rates from GRACE. *Earth and Planetary Science Letters*, 266, 140-148.

Choudhury, B. J., and Chang, A. T. C. 1981. On the angular variation of solar reflectance of snow. *Journal of Geophysical Research*, 86, 1, 465-472.

Coulson, K. L., Dave, J. V., and Sekera, Z. 1960. *Tables related to radiation emerging from a planetary atmosphere with Rayleigh scattering.* University of California Press.

Cuffey, K. M., and Paterson, W. S. B. 2010. *The Physics of Glaciers*, 4th Edition. Elsevier Inc.

Cutler, P. and Munro, D. S. 1996. Visible and near-infrared reflectivity during the ablation period on Peyto Glacier, Alberta, Canada. *Journal of Glaciology*, 42, 333-340.

Dahlke, H. E., Lyon, S. W., Stedinger, J. R., Rosqvist, G., and Jansson, P. 2012. Contrasting trends in floods for two sub-arctic catchments in northern Sweden – does glacier presence matter? *Hydrology and Earth System Sciences*, 16, 2123-2141.

Dumont, M., Durand, Y., Arnaud, Y., and Six, D. 2012. Variational assimilation of albedo in a snowpack model and reconstruction of the spatial mass-balance distribution of an alpine glacier. *Journal of Glaciology*, 58, 207, 151-164.

Flowers, G.E., Björnsson, H., Geirsdóttir, Á., Miller, G.H., and Clarke, K.C. 2007. Glacier fluctuation and inferred climatology of Langjökull ice cap through the Little Ice Age, *Quaternary Science Reviews*, 26, 2337-2353.

Gardner, A. S. and Sharp, M. J. 2010. A review of snow and ice albedo and the development of a physically based broadband albedo parameterisation. *Journal of Geophysical Research*, 115, F01009, doi:10.1029/2009JF001444.

Goetz, B. 2012. Making accurate field spectral reflectance measurements.

Greuell, W., and Oerlemans, J. 2004. Narrowband-to-broadband conversion for glacier ice and snow: equations based on modelling and rangers of validity of equations. *Remote Sensing of Environment*, 89, 95-105

Greuell, W., and Oerlemans, J. 2005. Assessment of the surface mass balance along the K-transect (Greenland ice sheet) from satellite-derived albedos. *Annals of Glaciology*, 42, 107-116.

Greuell, W., and de Ruyter de Wildt, M. 1999. Anisotropic reflection by melting glacier ice: Measurements and parameterisations in Landsat TM bands 2 and 4. *Remote Sensing of Environment*, 70, 3, 265-277.

Greuell, W., Reijmer, C. H., Oerlemans, J. 2002. Narrowband-to-broadband albedo conversion for glacier ice and snow based on aircraft and near-surface measurements. *Remote Sensing of Environment*, 82, 48-63.

Grinsted, A. 2013. An estimate of global glacier volume. *The Cryosphere*, 7, 1, 141-151.

Guðmundsson, S., Björnsson, H., Pálsson, F., and Haraldsson, H.H. 2003. Physical energy balance and degree-day models of summer ablation on Langjökull ice cap, SW-Iceland. *Technical Report RH-20-2003*. Science Institute, University of Iceland, Reykjavik, 20pp.

Guðmundsson, S., Björnsson, H., Pálsson, F., and Haraldsson, H.H. 2009. Comparison of energy balance and degree-day model of summer ablation on the Langjökull ice cap, SW-Iceland, *Jökull,* 59, 1-18.

Guo, L. J., Moore, J. McM., and Haigh, J. D. 1997. Simulated reflectance technique for ATM image enhancement. *International Journal of Remote Sensing*, 18, 2, 243-254.

Hay, J. E., and Fitzharris, B. B. 1988. A comparison of the energy-balance and bulk-aerodynamic approaches for estimating glacier melt. *Journal of Glaciology*, 34, 117, 145-153.

Hock, R. 2005. Glacier melt: a review of processes and their modelling. *Progress in Physical Geography*, 29, 3, 363-391.

Hooker, B. L. and Fitzharris, B. B. 1999. The correlation between climatic parameters and the retreat and advance of Franz Josef Glacier, New Zealand. *Global and Planetary Change*, 22, 39-48.

Hubbard, B., Heald, A., Reynold, J., Quincey, D. J. 2004. Impact of a rock avalanche on a moraine-dammed proglacial lake: Laguna Safuna Alta, Cordillera Blanca, Peru. *Earth Surface Processes and Landforms*, 30, 11, 1251-1264.

IPCC, 2007. *Climate Change 2007: The Physical Science Basis.* Working Group I contribution to the Fourth Assessment Report of the Intergovernmental Panel on Climate Change. Cambridge University Press.

Ishii, M., Kimoto, M., Sakamoto, K., and Iwasaki, S. I. 2006. Steric sea level changes estimated from historical ocean subsurface temperature and salinity analyses. *Journal of Oceanography*, 62, 2, 155-170.

Jacob, F., Olioso, A., Weiss, M., Baret, F., and Hautecoeur, O. 2002. Mapping short-wave albedo of agricultural surfaces using airborne PolDER data. *Remote Sensing of Environment*, 80, 36-46.

Jin, Y., Schaaf, C. B., Woodcok, C. E., Gao, F., Li, X., Strahler, A. H., Lucht, W., and Liang, S. 2003. Consistency of MODIS surface bidirectional reflectance distribution function and albedo retrievals, 2. Validation. *Journal of Geophysical Research-Atmospheres*, 108, D5, 4159.

Kachouie, N. N., Huybers, P., and Schwartzman, A. 2013. Localisation of mountain glacier termini in Landsat multi-spectral images. *Pattern Recognition Letters*, 34, 1, 94-106.

Kaufman, Y. J., Wald, A. E., Remer, L. A., Gao, B.-C., Li, R.-R. and Flynn, L. 1997. The MODIS 2.1µm channel-correlation with visible reflectance for use in remote sensing of aerosol. *IEEE Transactions on Geoscience and Remote Sensing*, 35, 1286-1298.

Kennedy, R. E., Warren, C. B., and Takao, G. 1997. Empirical methods to compensate for a view-angle-dependent brightness gradianet in AVIRIS imagery. *Remote Sensing of Environment*, 62, 3, 277-291.

Klok, E. J., Greuell, W., and Oerlemans, J., 2003. Temporal and spatial variation of the surface albedo of Morteratschgletscher, Switzerland, as derived from 12 Landsat images. *Journal of Glaciology*, 49, 167, 491-502.

Klok, E. J. and Oerlemans, J. 2002. Model study of the spatial distribution of the energy and mass balance of Morteratschgletscher, Switzerland, *Journal of Glaciology*, 48, 16, 505-515.

Knap, W.H., and Reijmer, C.H. 1998. Anisotropy of the Reflected Radiation Field over Melting Glacier Ice: Measurements in Landsat TM Bands 2 and 4. *Remote Sensing Environment*, 65, 93-104.

Knap, W.H., Brock, B.W., Oerlemans, J., and Willis, I.C. 1999. Comparison of Landsat TM-derived and ground-based albedos of Haut Glacier d'Arolla, Switzerland. *International Journal of Remote Sensing,* 20, 17, 3293-3310.

Kokhanovsky, A. A., and Breon, F. –M. 2012. Validation of an Analytical Snow BRDF Model using PARASOL multi-angular and multispectral observations. *IEEE Geoscience and Remote Sensing Letters*, 9, 5, 928-932.

Kotchenova, S. Y., and Vermote, E. F. 2007. Validation of a vector version of the 6S radiative transfer code for atmospheric correction of satellite data. Part II: Homogeneous Lambertian and anisotropic surfaces. *Applied Optics*, 46, 20, 4455-4464.

Kotchenova, S. Y., Vermote, E. F., Matarrese, R., and Klemm, F. J. 2006 Validation of a vector version of the 6S radiative transfer code for atmospheric correction of satellite data. Part I: Path Radiance. *Applied Optics*, 45, 26, 6726-6774.

Kruse, F. A. 2004. Comparison of ATREM, ACORN, and FLAASH atmospheric corrections using low-altitude AVIRIS data of Boulder, CO. *Summaries of 13th JPL Airborne Geoscience Workshop, Jet Propulsion Lab, Pasadena, CA.*

Kuhn, M. 1985. Bidirectional reflectance of polar and alpine snow surfaces. *Annals of Glaciology*, 6, 164-167.

Laumann, T., and Reeh, N. 1993. Sensitivity to climate change of the mass balance of glaciers in southern Norway. *Journal of Glaciology*, 39, 133, 656-665.

Lee, D. S., Storey, J. C., Choate, M. J., and Hayes, R. 2004. Four years of Landsat-7 on-orbit geometric calibration and performance. *IEEE Transactions of Geoscience and Remote Sensing*, 42, 2786-2795.

Letreguilly, A. 1988. Relation between the mass balance of western Canadian mountain glaciers and meterological data. *Journal of Glaciology*, 34, 11-18.

Li, W., Stamnes, K., and Eide, H. 2007. Bidirectional reflectance distribution function of snow: corrections for the Lambertian assumption in remote sensing applications. *Optical Engineering*, 46, 6, 066201.

Li, X., and Strahler, A. H. 1992. Geometric-optical bidirectional reflectance modelling of the discrete crown vegetation canopy: Effect of crown shape and mutual shadowing. *IEEE Transactions on Geoscience and Remote Sensing*, 30, 276-292.

Liang, S., Strahler, A. H., and Walthall, C. 1999. Retrieval of land surface albedo from satellite observations: a simulation study. *Journal of Applied Meteorology*, 38, 712-725.

Liang, S., Stroeve, J., and Box, J. E. 2005. Mapping daily snow/ice shortwave broadband albedo from Moderate Resolution Imaging Spectroradiometer (MODIS): The improved direct retrieval algorithm and validation with Greenland in situ measurements. *Journal of Geophysical Research*. 110, D10109, doi:10.1029/2004JD005493.

Lillesand, T. M. and Kiefer, R. W. 2000. *Remote sensing and image interpretation,* 4th Edition. John Wiley and Sons Inc.

Lucht, W., Schaaf, C. B., and Strahler, A. H. 2000. An algorithm for the retrieval of albedo from space using semiempirical BRDF models. *IEEE Transactions on Geoscience and Remote Sensing*, 38, 2, 977-998.

Lyapustin, A. I., and Privette, J. L. 1999. A new method of retrieving surface bidirectional reflectance from ground measurements: atmospheric sensitivity study. *Journal of Geophysical Research*, 104, D6, 6257-6268.

MacArthur, A., 2007a. Field Guide for the ASF FieldSpec Pro – Radiance/Irradiance Measurements in Raw DN mode. *Available at:* http://fsf.nerc.ac.uk/resources/guides/pdf_guides/asd_guide_v2_RadIrrad.pdf

MacArthur, A., 2007b. Field Guide for the ASF FieldSPec Pro – Raw DN Mode. *Available at:* http//fsf.nerc.ac.uk/resources/guides/pdf_guides/asd_guides_v2_dn.pdf

MacArthur, A., 2007c. Field Guide for the ASF FieldSpec Pro – White reference mode. *Available at:* http//fsf.nerc.ac.uk/resources/guides/pdf_guides/asd_guide_v2_wr.pdf

Mahiny, A. S., and Turner, B. J. 2007. A comparison of four common atmospheric correction methods. *Photogrammetric Engineering and Remote Sensing*, 73, 4, 361-368.

Markham, B. L., Barker, J. L., Barsi, J. A., Kaita, E., Thome, K. J., Helder, D. L., Palluconi, F. D., Schott, J. R., and Scaramuzza, P. 2003. Landsat-7 EMT+ radiometric stability and absolute calibration. *Proceedings of SPIE*, 4881, 308-318.

Markham, B. L., Thome, K., Barsi, J., Kaiti, E. Helder, D., Barker, J., and Scaramuzza, P. 2004. Landsat-7 EMT+ On-Orbit reflective-band radiometric stability and absolute calibration. *IEEE Transactions on Geoscience and Remote Sensing*, 42, 2810-2810.

Masson, R., and Lubin D. 2006. *Polar remote sensing: Volume II: Ice Sheets.* Springer.

Matthew, M. W., Adler-Golden, S. M., Berk, A., Felde, G., Anderson, G. P., Gorodetzky, D., Paswaters, S., and Shippert, M. 2003. Atmospheric correction of spectral imagery: evaluation of the FLAASH algorithm with AVIRIS data. *SPIE Proceeding, Algorithms and Technologies for Multispectral, Hyperspectral and Ultraspectral Imagery IX.*

Matthew, M. W., Adler-Golden, S. M., Berk, A., Richtsmeier, S. C., Levine, R. Y., Bernstein, L. S., Acharya, P. K., Anderson, G. P., Felde, G. W., Hoke, M. P., Ratowski, A., Burke, H. –H., Kaiser, R. D., and Miller, D. P. 2000. Status of Atmospheric Correction using a MODTRAN4-based algorithm. *SPIE Proceeding, Algorithms for Multispectral, Hyperspectral and Ultraspectral Imagery VI,* 4049, 199-207.

Meier, M. F., Dyurgerov, M. B., Rick, U. K., O'Neel, S., Pfeffer, W., T., Anderson, R. S., Anderson, S. P., and Glazovsky, A. F. 2007. Glacier dominate eustatic sea-level rise in the 21st Century. *Science*, 317, 1064-1067.

Milton, E. J., Schaepman, M. E., Anderson, K., Kneubühler, M., and Fox., N. 2009. Progress in field spectroscopy. *Remote Sensing of Environment*, 113, S92-S109.

Mishchenko, M. I., Dlugachb, J. M., Yanovitskijb, E. G., and Zakharovac, N. T. 1999. Bidirectional reflectance of flat, optically thick particulate layers: An efficient radiative transfer solution and applications to snow and soil surfaces. *Journal of Quantitative Spectroscopy and Radiative Transfer*, 63, 409-432.

Molotch, N. P., Painter, T. H., Bales, R. C., and Dozier, J. 2004. Incorporating remotely sensed snow albedo into a spatially distributed snowmelt model. *Geophysical Research Letters*, 32, L03501, doi:10.1029/2003GL019063.

Molotch, N. P., and Bales, R. C. 2006. Comparison of ground-based and airborne snow surface albedo parameterisations in an alpine watershed: Impact on snowpack mass balance. *Water Resource Research*, 42, W05410, doi:10.1029/2005WR004522.

Moore, R. D. and Demuth, M. N. 2001. Mass balance and streamflow variability at Place Glacier, Canada in relation to recent climate fluctuations. Hydrological Processes, 15, 3473-3486.

Munro, D. S. 1990. Comparison of melt energy computations and ablatometer measurements on melting ice and snow. *Arctic, Alpine Research*, 22, 2, 153-162.

NERC, 2013. http://arsf.nerc.ac.uk/instruments/atm.asp.

NERC FSF, 2013. Excel Post Processing Templates and User Guides. Available at http://fsf.nerc.ac.uk/resources/post-processing/index.shtml [Accessed January 12, 2013].

Oerlemans, J. 1992. Climate sensitivity of glaciers in southern Norway: application of an energy-balance model to Nigardsbreen, Hellstugubreen, and Alfotbreen. *Journal of Glaciology*, 38, 129, 223-232.

Palubinskas, G., Müller, R., and Reinartz, P. 2003a. Mosaiching of optical remote sensing imagery. *Proceedings of the IEEE International Geoscience and Remote Sensing Symposium (IGASS03)*, 3955-3957.

Palubinskas, G., Müller, R., and Reinartz, P. 2003b. Radiometric normalisation of optical remote sensing imagery. *Proceedings of the IEEE International Geoscience and Remote Sensing Symposium (IGASS03)*, 2, 720-722.

Paterson, W. S. B. 1994. *The physics of glaciers* 3rd Edition. Oxford: Pergamon Press.

Paul, F., Kaab, A., Maisch, M., Kellenberger, T. And Haeberli, W. 2004. Rapid disintegration of Alpine glaciers observed with satellite date. *Geophysical Research Letters*, 31, L21402, doi:10.1029/2004GL020816.

Paul, F. 2000. Evaluation of different methods for glacier mapping using Landsat TM, *Proceedings of EARSel-SIG-Workshop Land Ice and Snow, Dresden/FRG, June 16-17, EARSel eProceedings,* 1, 239-245.

Pellikka, P., and Rees, W. G. 2010. *Remote Sensing of Glaciers*. London: CRC Press.

Perkins, T. Adler-Golden, S. M., Cappelaere, P., and Mandl, D. 2012. High-speed Atmospheric Correction for Spectral Image Processing. *SPIE Proceedings, 8390.*

Pope, A. 2013. Multispectral Classification and reflectance of glaciers: *In situ* data collection, satellite data algorithm development, and application in Iceland and Svalbard. *Unpublished.*

Pope, A., and Rees, W. G. 2013. Using *in situ* spectra to explore Landsat classification of glacier surfaces. *(In press)*

Pope, E. L. 2012. An analysis of the ability of Landsat ETM+ measurements to accurately represent glacier surface characteristics. *Unpublished.*

Privette, J. L., Eck, T. F., and Deering, D. W. 1997. Estimating spectral albedo and nadir reflectance through inversion of simple BRDF models with AVHRR/MODIS-like data. *Journal of Geophysical Research*, 102, 29529-29542.

Quincey, D. J. and Luckman, A. 2009. Progress in satellite remote sensing. *Progress in Physical Geography*, 33, 4, 547-567.

Radić, V., and Hock, R. 2010. Regional and global volume of glaciers derived from statistical upscaling of glacier inventory data. *Journal of Geophysical Research*, 115, F01010, doi:10.1029/2009JF001373.

Radić, V., and Hock, R. 2011. Regionally differentiated contribution of mountain glaciers and ice caps to future sea-level rise. *Nature Geoscience*, 4, 2, 91-94.

Reijmer, C.H., Knap, W.H., and Oerlemans, J. 1999. The surface albedo of the Vatnajökull Ice Cap, Iceland: A comparison between satellite-derived and ground-based measurements. *Boundary-Layer Meterology,* 92, 125-144.

Rees, W. G. 1999. *The remote sensing data book*. Cambridge University Press.

Rees, W. G. 2001. *Physical principles of remote sensing,* 2nd Edition. Cambridge University Press.

Rees, W. G. 2006. *Remote sensing of snow and ice*, Taylor and Francis Group.

Rees, W. G. 2013. *Physical principals of remote sensing*, 3rd Edition. Cambridge University Press.

Ribstein, P., Tiriau, E., Francou, B., and Saravia, R. 1995. Tropical climate and glacier hydrology: a case study in Bolivia. *Journal of Hydrology*, 165, 221-234.

Richardson, S. D., and Reynolds, J. M. 2000. An overview of glacial hazards in the Himalayas. *Quaternary International*, 65/66, 31-47.

Ross, J. K. 1981. *The radiation regime and architecture of plant stands*. Norwell, MA: Dr. W. Junk, 392pp.

Röthlisberger, H. and Lang, H. 1987. Glacial Hydrology. In Gurnell, A. M., and Clark, M. J. (eds.) *Glacio-fluvial Sediment Transfer.* Wiley, New York, 207-284.

Roujean, J. L., Leroy, M., and Deschamps, P. Y. 1992. A bidirectional reflectance model of the Earth's surface for the correction of remote sensing data. *Journal of Geophysical Research*, 97, 20450-20468.

Roy, D., Borak, J., Devadiga, S., Wolfe, R., Zheng, M., and Descloitres, J. 2002. The MODIS land product quality assessment approach. *Remote Sensing of Environment*, 83, 62-76.

Roy, D. P., Ju, J. Kline, K., Scaramuzza, P. L., Kovalskyy, V., Hansen, M., Loveland, T. R., Vermote, E., and Zhang, C. 2010. Web-enabled Landsat Data (Weld): Landsat ETM+ composited mosaics of the conterminous United States. *Remote Sensing of Environment*, 114, 35-48.

Salomon, J. G., Schaaf, C. B., Strahler, A. H., Gao, F., and Jin, Y. 2006. Validation of the MODIS bidirectional reflectance distribution function and albedo retrievals using combined observations from the Aqua and Terra platforms. *IEEE transactions on geosciences and remote sensing,* 44, 6, 1555-1565.

Schaaf, C. B., Gao, F., Strahler, A. H., Lucht, W., Li, X., Tsang, T., Strugnell, N. C., Zhang, X., Jin, Y., Muller, J., Lewis, P., Barnsley, M., Hobson, P., Disney, M., Roberts, G., Dunderdale, M., Doll, C., d'Entremont, R. P., Hu, B., Liang, S., Privette, J. L., and Roy, D. 2002. First operational BRDF, albedo nadir reflectance products from MODIS. *Remote Sensing of the Environment*, 83, 135-148.

Schaepman-Strub, G., Schaepman, M. E., Painter, T. H., Dangel, S., Martonchik, J. V. 2006. Reflectance quantities in optical remote sensing – definitions and case studies. *Remote Sensing of Environment*, 103, 27-42.

Shimamura, Y. Izumi, T., and Matsuyama, H. 2006. Evaluation of a useful method to indentify snow-covered areas under vegetation – comparisons among a newly proposed snow index, normalised difference snow index, and visible reflectance. *International Journal of Remote Sensing*, 27, 21-22, 4867-4884.

Sigurðsson, F. 1990. Groundwater from glacial areas in Iceland. *Jökull*, 40, 119-145.

Steffan, K., Bindschadler, R., Casassa, G., Comiso, J., Eppler, D., Fetterer, F., Hawkins, J., Key, J., Rothrock, D., Thomas, R., Weaver, R., and Welch, R. 1993. Snow and ice applications of AVHRR in polar regions: report workshop held in Boulder, Colorado, 20 May 1992. *Annals of Glaciology*, 17, 1-16.

Storey, J. C., Choate, M. J., and Lee, K. 2008. Geometric performance comparison between the OLI and the ETM+. *Proceedings at Pecora 17, 2008, Denver Colorado.*

Strahler, A. H., Wanner, W., Schaaf, C. B., Li, X., Hu, B., Muller, J. -P., Lewis, P., and Barnsley, M. J. 1996. MODIS BRDF/Albedo Product: Algorithm theoretical basis document version 4.0.

Stroeve, J., Box, J.E., Gao, F., Liang, S., Nolin, A., and Schaaf, C. 2005. Accuracy assessment of the MODIS 16-day albedo product for snow: comparisons with Greenland in situ measurements. *Remote Sensing of Environment*, 94, 46-60.

Stuiver, M. and Grootes, P. M. 2000. GISP2 Oxygen Isotope Ratios. *Quaternary Research*, 53, 277-284.

Suttles, J. T., Green, R. N., Minnis, P., Smith, G. L., Stayler, W. F., Wielicki, B. A., Walker, I. J., Young, D. F., Taylor, V. R., and Stone, L. L. 1988. *Angular Radiation Models for Earth Atmosphere System. Volume I: Shortwave Radiation,* NASA Reference Publication 1184, NASA, Washington, DC.

Tedesco, M., Fettweis, X., van den Broeke, M.R., van de Wal, R.S.W., Smeets, C.J.P.P., van de Berg, W.J., Serreze, M.C., and Box, J.E. 2011. The role of albedo and accumulation in the 2010 melting record in Greenland, *Environmental Research Letters*, 6, doi:10.1088/1748-9326.

Thome, K.J. 2001. Absolute radiometric calibration of Landsat 7 ETM+ using the reflectance-based method. *Remote sensing of environment*, 78, 27-38.

Thorson, E. J. 2009. Sharing Himalayan glacial meltwater: the role of territorial sovereignty. *Duke Journal of Comparative and International Law*, 19, 487-514.

Tucker, C. J., Grant, D. M., and Dykstra, J. D. 2004. NASA’s global orthorectified Landsat data set. *Photogrammetric Engineering and Remote Sensing*, 70, 313-322.

USGS, 2010. SLC-off products: Background. *landsat.usgs.gov/products_slcoffbackground.php*.

Van Angelen, J. H., Lenaerts, J. T. M., Lhermitte, S., Fettweis, X., Kuipers Munneke, P., van den Broeke, M. R., and van Meijgaard, E. 2012. Sensitivity of Greenland Ice Sheet surface mass balance to surface albedo parameterisation: a study with a regional climate model. *The Cryosphere Discussions*, 6, 1531-1562.

Varone, F., Reynard, E., Kissling-Naf, I., and Mauch, C. 2002. Institutional resource regimes: the case of water management in Switzerland. *Integrated Assessment*, 3, 1, 78-94.

Vermote, E.F., El Saleous, N. Z., Justice, C. O., Kaufman, Y. J., Privette, J. L., Remer, L., Roger, J. C., and Tanre, D. 1997. Atmospheric correction of visible to middle-infrared EOS-MODIS data over land surfaces: background, operational algorithm and validation. *Journal of Geophysical Research-Atmosphere*, 102(D14), 17131-17141.

Vermote, E. F., El Saleous, N. Z., and Justice, C. O. 2002. Atmospheric correction of MODIS data in the visible to middle infrared: first results. *Remote Sensing of Environment*, 83, 97-111.

Vermote, E. F., Tanré, D., Deuzé, J. L., Herman, M., Morcrette, J. J., and Kotchenova, S. Y. 2006. Second simulation of a satellite signal in the solar spectrum – vector (6SV) user guide.

Warren, S. G., and Wiscombe, W. J. 1980. A model for the spectral albedo of snow. II: Snow containing atmospheric aerosols. *Journal of the Atmopsheric Sciences*, 37, 12, 2734-2745.

Wendisch, M., Pilewskie, P., Jäkel, E., Schmidt, S., Pommier, J., Howard, S., Jonsson, H. H., Guan, H., Schröder, M., and Mayer, B. 2004. Airborne measurements of areal spectral surface albedo over different sea and land surfaces. *Journal of Geophysical Research*, 109, D08203, doi:10.1029/2003JD004392.

Westoby, M. J., Brasington, J., Glasser, N. F., Hambrey, M. J., Reynolds, J. M. 2012. 'Structure-from-Motion' photogrammetry: a low-cost, effective tool for geosciences applications. *Geomorphology*, 179, 300-314.

Williams, R. S., Hall, D. K., and Benson, C. S., 1991. Analysis of glacier facies using satellite techniques. *Journal of Glaciology*, 35, 125, 120-128.

Willis, I. C., Arnold, N. S., Sharp, M., Bonvin, J-M., and Hubbard, B. 1998. *Mass balance and flow variations of Haut Glacier d'Arolla, Switzerland calculated using digital terrain modelling techniques*, in Lane, S. N., Chandler, J. H., and Richards, K. S. (eds.) *Landform Monitoring, Modelling and Analysis*. John Wiley and Sons.

Wu, H., and Tong, L. 2011. Modelling visible and near-infrared snow surface reflectance-simulation and validation. *Chinese Optics Letters*, 9, 10, 102901-3.

Xiong X., and Barnes, W. 2006. An overview of MODIS radiometric calibration and characterisation. *Advances in Atmospheric Sciences*, 23, 1, 69-79.

Zelazowski, P., Sayer, A. M., Thomas, G. E., and Grainger, R. G. 2011. Reconciling satellite-derived atmospheric properties with fine-resolution land imagery: insights for atmospheric correction. *Journal of Geophysical Research*, 116, D18308, doi:10.1029/2010JD015488.

Zhao, Y., Meng, Z., Wang, L., Miyazaki, S., Geng, X., Zhou, G., Liu, R., Kosaka, N., Takahashi, M., Li, X. 2005. A new cross-track radiometric correction method (VRadCor) for airborne hyperspectral image of operational modular imaging spectrometer (OMIS). *Proceedings of IEEE IGARSS*, 3553-3556.

Zwally, H. J., Schutz, B., Abdalati, W., Abshire, J., Bently, C., Brenner, A., Bufton, J., Dezio, J., Hancock, D., Harding, D., Herring, T., Mintser, B., Quinn, K., Palm, S., Spinhirne, J., and Thomas, R. 2002. ICESat’s laser measurements of polar ice, atmosphere, ocean and land. *Journal of Geodynamics*, 34, 405-445.